



FJSRL-TR-95-0005

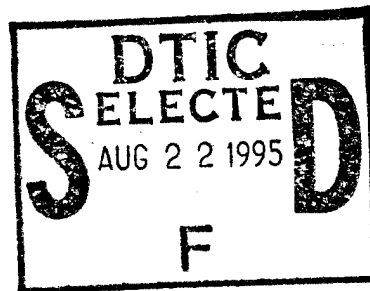
FRANK J. SEILER RESEARCH LABORATORY

MATERIALS PHYSICS

WORK UNIT 2300-FF-05

FINAL REPORT

OCTOBER 1991 - SEPTEMBER 1995



**CAPTAIN PETER M. RANON
TASK MANAGER**

**APPROVED FOR PUBLIC RELEASE;
DISTRIBUTION UNLIMITED.**

SEPTEMBER 1995



AIR FORCE MATERIEL COMMAND

UNITED STATES AIR FORCE

19950821 008


FJSRL-TR-95-0005

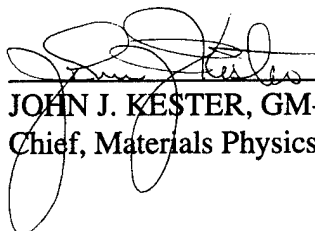
This document was prepared by the Materials Physics Division, Frank J. Seiler Research Laboratory, United States Air Force Academy CO. The research was conducted under Project Work Unit Number 2300/FF/05, Materials Physics. Dr John J. Kester was the Division Chief and Captain Peter M. Ranon was the Project Officer in charge of the work.

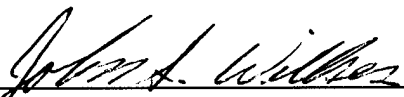
When U.S. Government drawings, specifications, or other data are used for any purpose other than a definitely related government procurement operation, the government thereby incurs no responsibility nor any obligation whatsoever, and the fact that the government may have formulated, furnished, or in any way supplied the said drawings, specifications, or other data is not to be regarded by implication or otherwise, as in any manner licensing the holder or any other person or corporation or conveying any rights or permission to manufacture, use or sell any patented invention that may in any way be related thereto.

[This report has been reviewed by the Technical Director and is releasable to the National Technical Information Service (NTIS). At NTIS it will be available to the general public, including foreign nations.]

This technical report has been reviewed and is approved for publication.


PETER M. RANON, Captain, USAF
Task Manager, Materials Physics


JOHN J. KESTER, GM-14, DAF
Chief, Materials Physics Division


JOHN S. WILKES, GM-15, DAF
Technical Director

REPORT DOCUMENTATION PAGE			Form Approved OMB No. 0704-0188	
Public reporting burden for this collection of information is estimated to average 1 hour per response, including the time for reviewing instructions, searching existing data sources, gathering and maintaining the data needed, and completing and reviewing the collection of information. Send comments regarding this burden estimate or any other aspect of this collection of information, including suggestions for reducing this burden, to Washington Headquarters Services, Directorate for Information Operations and Reports, 1215 Jefferson Davis Highway, Suite 1204, Arlington, VA 22202-4302, and to the Office of Management and Budget, Paperwork Reduction Project (0704-0188), Washington, DC 20503.				
1. AGENCY USE ONLY (Leave blank)		2. REPORT DATE SEPTEMBER 1995	3. REPORT TYPE AND DATES COVERED FINAL - October 1991 -- September 1995	
4. TITLE AND SUBTITLE MATERIALS PHYSICS - WORK UNIT 2300/FF/05 - FINAL REPORT			5. FUNDING NUMBERS	
6. AUTHOR(S) CAPTAIN PETER M. RANON				
7. PERFORMING ORGANIZATION NAME(S) AND ADDRESS(ES) FRANK J. SEILER RESEARCH LABORATORY 2354 VANDENBERG DRIVE, SUITE 6H79 USAF ACADEMY CO 80840-6272			8. PERFORMING ORGANIZATION REPORT NUMBER FJSRL-TR-95-0005	
9. SPONSORING / MONITORING AGENCY NAME(S) AND ADDRESS(ES)			10. SPONSORING / MONITORING AGENCY REPORT NUMBER	
11. SUPPLEMENTARY NOTES				
12a. DISTRIBUTION / AVAILABILITY STATEMENT Distribution Unlimited			12b. DISTRIBUTION CODE	
13. ABSTRACT (Maximum 200 words)				
THIS QUANTITY EXHAUSTED				
14. SUBJECT TERMS NONLINEAR OPTICS, THIN FILMS, LASER ABLATION			15. NUMBER OF PAGES 113	
			16. PRICE CODE	
17. SECURITY CLASSIFICATION OF REPORT UNCLASSIFIED	18. SECURITY CLASSIFICATION OF THIS PAGE UNCLASSIFIED	19. SECURITY CLASSIFICATION OF ABSTRACT UNCLASSIFIED	20. LIMITATION OF ABSTRACT NONE	

GENERAL INSTRUCTIONS FOR COMPLETING SF 298

The Report Documentation Page (RDP) is used in announcing and cataloging reports. It is important that this information be consistent with the rest of the report, particularly the cover and title page. Instructions for filling in each block of the form follow. It is important to **stay within the lines** to meet **optical scanning requirements**.

Block 1. Agency Use Only (Leave blank).

Block 2. Report Date. Full publication date including day, month, and year, if available (e.g. 1 Jan 88). Must cite at least the year.

Block 3. Type of Report and Dates Covered. State whether report is interim, final, etc. If applicable, enter inclusive report dates (e.g. 10 Jun 87 - 30 Jun 88).

Block 4. Title and Subtitle. A title is taken from the part of the report that provides the most meaningful and complete information. When a report is prepared in more than one volume, repeat the primary title, add volume number, and include subtitle for the specific volume. On classified documents enter the title classification in parentheses.

Block 5. Funding Numbers. To include contract and grant numbers; may include program element number(s), project number(s), task number(s), and work unit number(s). Use the following labels:

C - Contract	PR - Project
G - Grant	TA - Task
PE - Program Element	WU - Work Unit Accession No.

Block 6. Author(s). Name(s) of person(s) responsible for writing the report, performing the research, or credited with the content of the report. If editor or compiler, this should follow the name(s).

Block 7. Performing Organization Name(s) and Address(es). Self-explanatory.

Block 8. Performing Organization Report Number. Enter the unique alphanumeric report number(s) assigned by the organization performing the report.

Block 9. Sponsoring/Monitoring Agency Name(s) and Address(es). Self-explanatory.

Block 10. Sponsoring/Monitoring Agency Report Number. (If known)

Block 11. Supplementary Notes. Enter information not included elsewhere such as: Prepared in cooperation with...; Trans. of...; To be published in.... When a report is revised, include a statement whether the new report supersedes or supplements the older report.

Block 12a. Distribution/Availability Statement. Denotes public availability or limitations. Cite any availability to the public. Enter additional limitations or special markings in all capitals (e.g. NOFORN, REL, ITAR).

DOD - See DoDD 5230.24, "Distribution Statements on Technical Documents."

DOE - See authorities.

NASA - See Handbook NHB 2200.2.

NTIS - Leave blank.

Block 12b. Distribution Code.

DOD - Leave blank.

DOE - Enter DOE distribution categories from the Standard Distribution for Unclassified Scientific and Technical Reports.

NASA - Leave blank.

NTIS - Leave blank.

Block 13. Abstract. Include a brief (*Maximum 200 words*) factual summary of the most significant information contained in the report.

Block 14. Subject Terms. Keywords or phrases identifying major subjects in the report.

Block 15. Number of Pages. Enter the total number of pages.

Block 16. Price Code. Enter appropriate price code (*NTIS only*).

Blocks 17. - 19. Security Classifications. Self-explanatory. Enter U.S. Security Classification in accordance with U.S. Security Regulations (i.e., UNCLASSIFIED). If form contains classified information, stamp classification on the top and bottom of the page.

Block 20. Limitation of Abstract. This block must be completed to assign a limitation to the abstract. Enter either UL (unlimited) or SAR (same as report). An entry in this block is necessary if the abstract is to be limited. If blank, the abstract is assumed to be unlimited.

TABLE OF CONTENTS

INTRODUCTORY SUMMARY	1
TIME-INTEGRATED OPTICAL EMISSION STUDIES OF PLUMES GENERATED FROM LASER ABLATED GERMANIA GLASS - WOLF	2
PHOTODISSOCIATION DYNAMICS OF S_4N_4 AT 222 AND 248 NM - ONGSTAND, LAWCONNELL, HENSHAW	9
SECOND-HARMONIC GENERATION IN PLANAR WAVEGUIDES OF DOPED SILICA - KESTER, WOLF, WHITE	21
SECOND HARMONIC GENERATION IN LOW-WATER FUSED SILICA BY PROTON IMPLANTATION - HENRY, ALLEY, RAND, KESTER	25
FIRST-PRINCIPLES CHARACTERIZATION OF STRUCTURE AND PROPERTIES OF E' CENTERS - KARNA, KESTER	30
MODAL AND POLARIZATION PROPERTIES OF SHG IN DOPED-SILICA WAVEGUIDES: TRANSVERSE MODULATION EFFECTS - KESTER, DAJANI, RANON, ALLEY	35
SECOND-HARMONIC GENERATION EFFICIENCIES IN GERMANIUM- DOPED PLANAR WAVEGUIDES: A NORMAL-MODE ANALYSIS - DAJANI	40
EFFECT OF PRE-ANNEALING ON THE LEVEL OF SECOND HARMONIC GENERATION AND DEFECT SITES ACHIEVED IN POLED FUSED SILICA - HENRY, DEVILBISS, TSAI	62
SPECTROSCOPIC INVESTIGATION OF LASER ABLATED GERMANIUM OXIDE - WOLF, PATTERSON, WITANACHCHI	94
PUBLICATION LIST	100

Accession For	
NTIS	<input checked="" type="checkbox"/>
CRA&I	<input type="checkbox"/>
DTIC	<input type="checkbox"/>
TAB	<input type="checkbox"/>
Unannounced	<input type="checkbox"/>
Justification	
By	
Distribution /	
Availability Codes	
Dist	Avail and/or Special
A-1	

MATERIALS PHYSICS

Final Report for Work Unit 2300/FF/05

This task addressed basic research to better understand laser ablation deposition of thin films, nonlinear optical (NLO) effects in poled quartz, and the waveguiding properties of Ge doped silica planar waveguides. These efforts expanded the understanding of the interaction between light and matter and thus advanced the envelope of the technology base of NLO materials used in optical device applications. Research directly supported Air Force Objectives for Optoelectronic Materials, as outlined in the current research Technology Area Plan for Project 2305, Electronics.

The research was organized around the following areas: (1) laser ablation deposition of thin films, (2) NLO effects in poled quartz, and (3) the waveguiding properties of Ge doped silica planar waveguides. For the laser ablation effort, various techniques were used to investigate the optical losses and the properties of the laser ablation films. For NLO effects in poled quartz, two possible sources of SHG, which are the non-bridging oxygen hole centers (associated with Si and Ge) and peroxy bridge structures were found to be supported by experimental evidence. Through ion implantation which creates an internal poling field in quartz, second order NLO effects were introduced into otherwise amorphous films. For the waveguiding properties of Ge doped silica planar waveguides, credibility of computation efforts were increased significantly with high degree of correlation between experiment and theoretical predictions. Results for these topics are summarized in the next several sections.

For a more detailed account of the research, see the attached Work Unit publications and presentations listing.

Time-integrated optical emission studies of plumes generated from laser ablated germania glass

Paul J. Wolf^a

Frank J. Seiler Research Laboratory, Materials Physics Division, 2354 Vandenberg Drive, Suite 6H79, USAF Academy, Colorado 80840-6272

(Received 3 February 1994; accepted for publication 9 April 1994)

The optical emission from plumes induced by ArF laser irradiation of GeO_2 was characterized as a function of laser fluence, distance from the target surface, and ambient O_2 pressure. Dispersion of the light emitted by the plume in a vacuum revealed emission from both neutral and singly ionized Ge atoms as well as neutral O atoms. The spatial variation showed that the ion concentration decreased exponentially from the target surface while the neutral atom number density reached peak intensities at distances of ≈ 1.5 – 2.5 cm from the target surface. Interactions between the plume constituents and the ambient molecular oxygen increased the excited Ge atom and Ge ion populations in the plume and, most notably, significantly enlarged the excited O atom concentration over that produced directly from the ablation process.

I. INTRODUCTION

Pulsed laser ablation has become a very successful method for depositing high-quality thin films and modifying surfaces. The congruent removal of material from a target and the relatively high kinetic energies of the plume constituents are important characteristics of this method that can influence thin-film growth processes.¹ Although much is known about the properties of films deposited under typical laser ablation conditions, knowledge is generally lacking in understanding the dynamics of laser generated plumes and the kinetics that govern thin film growth by this method. The collection, analysis, and interpretation of spectroscopic data obtained from plumes created above a surface irradiated by an intense laser pulse details the plume composition, the energy content of the ablation products, and the dynamics of the plume species which can subsequently lead to an improved understanding of the laser ablation phenomenon. In principle, the evolution of the plume can be theoretically predicted with an understanding of the initiation mechanisms and kinetic processes (electron temperature, electron density, ionization state, etc.).

The spatial and temporal evolution of transient species produced during the laser-target interaction, such as excited atoms, ions, and molecules, can be monitored as a function of the irradiation conditions, ambient gas pressure and composition, and the axial/radial distance from the target surface by investigating the optical emission produced in the plumes. Many of these spectroscopic studies have been performed near the target surface where interesting plasma dynamics can be explored. Recently, Mehlman *et al.*^{2,3} reported results of a study in the vacuum ultraviolet to ultraviolet regions at distances less than 1 cm from the target surface aimed at obtaining insight into the early stages of the laser-target and laser-plasma interaction. In contrast, probing the plume at

distances comparable to typical target-substrate separations (≈ 4 – 8 cm) should provide information on the dynamics of the laser ablated material immediately prior to collisions with a substrate surface. These studies are particularly important when reactive gases are required for stoichiometric film growth since the presence of this ambient gas can affect both the nature and the energy of the material impinging on the film growth surface. Reactive gases are commonly used to maintain the oxygen content in films produced in ablation experiments that employ oxidized targets such as YBaCuO .⁴ The formation of metal-oxide diatomic molecules has been directly correlated with improved film stoichiometry and, in general, better film quality,⁵ and the distant separation between the target and the substrate allows for potentially more gas-phase reactive encounters which can produce these species. Several optical emission studies have been performed to understand the ablation of high T_c superconducting materials that ultimately result in the transfer of material onto a substrate.^{4–8} Although the bulk of both the temporal and time-integrated optical emission studies have been devoted to high T_c superconducting materials, optical emission spectroscopy has also been performed on other laser ablated materials such as carbon,⁹ dielectrics,^{10,11} metals such as Al,^{2,3,12} and various polymers.¹³

Recently, stoichiometric GeO_2 films have been fabricated on ambient temperature substrates by ablating GeO_2 targets in 150 mTorr of O_2 .¹⁴ The high O_2 pressures required to form stoichiometric films suggested that gas phase reactions, in addition to the presence of energetic atomic species, may be important for incorporating stoichiometric quantities of oxygen in the film. Thus the purpose of this work was to study the dynamics of material ablated from a GeO_2 target in the presence of molecular oxygen to correlate the ablation process and the plume composition with the formation of stoichiometric thin films. The light emitted by a plume after ArF laser irradiation of a GeO_2 target was collected and analyzed using optical emission spectroscopy (OES). The time-integrated emission spectra were analyzed to identify the

^aPresent address: Dept. of Engineering Physics, Air Force Institute of Technology, Wright Patterson AFB, OH 45433.

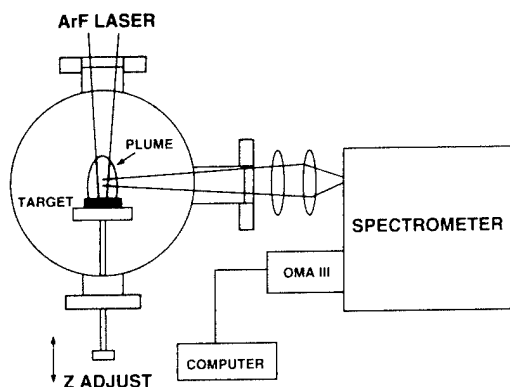


FIG. 1. Schematic diagram of the experimental arrangement.

composition of the plume, and the behavior of neutral and ionic species was mapped when variations were made in the O_2 pressure, laser fluence, and distance from the target surface. In a related study, Vega *et al.*¹⁵ investigated the ablation products of a Ge target as a function of O_2 pressure. These experiments, however, were performed at distances less than 5 mm from the target surface and, therefore, could be insensitive to possible reactions occurring downstream.

II. EXPERIMENT

Figure 1 shows the experimental arrangement with the ablation chamber and the data collection system. The experiments were performed in a vacuum chamber that typically achieved a base pressure of 2×10^{-6} Torr with a turbomolecular pump. An ArF laser [$\lambda = 193$ nm; 28 ns full width at half maximum (FWHM)] was focused at normal incidence onto the surface of a GeO_2 target to generate the plume. The laser fluence was varied between 0.5 – 6.5 $J\,cm^{-2}$ during the experiments by adjusting the combination of the laser energy and the spot size on the target surface. All data were collected with laser repetition rates ≤ 1 Hz. The experiments were performed both in vacuum (2×10^{-6} Torr) and O_2 pressures ranging from 10^{-4} Torr to 200 mTorr which spanned the pressure range used in previous GeO_x thin-film growth studies.¹⁴

The target was mounted on an adjustable shaft which allowed translation perpendicular to the target surface. The optical emission was sampled at several locations from the front surface of the target, z , by moving the target away from the "0" position while simultaneously adjusting the laser focusing lens to keep the laser fluence constant. Distances from 0.2 to 5 cm were covered in these studies. The "0" position was determined empirically by translating the target until the collected intensity lost features associated with discrete or continuum emission.

The interaction of laser radiation with the target produced a visible plume extending normal to the target surface. The optical emission was collected normal to the plume's main expansion direction with a spherical lens positioned at a focal length (23 cm) from the plume axis. A 15 cm focal length cylindrical lens subsequently focused the light onto a

$100\text{-}\mu\text{m}$ -wide entrance slit of a 0.5 m spectrometer. The spectrometer was equipped with a linear diode array (PAR OMA III) to detect the spectrally resolved emission. A glass microscope slide was positioned in front of the spectrometer to eliminate second order uv lines from being recorded at wavelengths above 350 nm. The OMA III signal was recorded, stored, and analyzed on a computer. Several visible and UV emission lines were recorded in the following wavelength regions: $260\text{ nm} \leq \lambda \leq 340\text{ nm}$ in 20 nm increments; $420\text{ nm} \leq \lambda \leq 520\text{ nm}$ in 20 nm increments; and 580, 600, and 780 nm. These spectral regions were chosen based on the known spectral line positions of neutral Ge atoms (Ge I),¹⁶ singly ionized Ge atoms (Ge II),¹⁶ molecular GeO ,¹⁷ and neutral O atoms (O I).¹⁸ Ten laser shots were required to achieve good signal-to-noise ratios in these experiments. The light collection system was not calibrated for absolute intensity measurements since only relative intensities were important in this work. The intensity of each spectral line was obtained by simply measuring peak heights after correcting for baseline variations.

The ablation rate of GeO_2 was also measured as a function of the incident laser energy density by irradiating fixed targets in vacuum. The laser fluence on target was determined by measuring the total energy delivered by the laser to the target position through all the optics and dividing this value by the area of the laser spot on the target. The crater depths were measured with a surface profiler at several locations along the length of the crater to obtain averaged values. The material removal rate was subsequently plotted as depth/pulse versus laser fluence.

III. RESULTS

A. GeO_2 ablation rate

Germanium dioxide targets were irradiated at energy densities between 0.5 and 7.0 $J\,cm^{-2}$. Well defined craters with 10 – 15 μm hole depths were produced on the target surface using 50–80 laser pulses at fluences F above 2 $J\,cm^{-2}$. At fluences between 1 – 2 $J\,cm^{-2}$, 75–100 laser pulses were required to achieve measurable crater depths. The irradiated areas at $F < 1$ $J\,cm^{-2}$ formed very shallow craters and they appeared to be heat damaged on the surface as opposed to other irradiated sites produced with higher laser fluences which clearly showed crater formation. The difficulty in measuring the area of these indentations over large laser spot sizes introduced large relative errors in the mass removal rates at $F \leq 1$ $J\,cm^{-2}$. Figure 2 shows the results plotted as crater depth in μm per laser pulse versus laser fluence. The data in Fig. 2 were fit to a phenomenological expression for the ablated depth as a function of fluence described in Eq. (1):

$$d = \alpha^{-1} \ln(F/F_{\text{threshold}}), \quad (1)$$

where d is the crater depth, α is the absorption coefficient at 193 nm, and $F_{\text{threshold}}$ is the ablation threshold fluence. As shown in Fig. 2, this expression produced a reasonable fit to the data with an absorption coefficient of $1.3 \times 10^5\text{ cm}^{-1}$ and

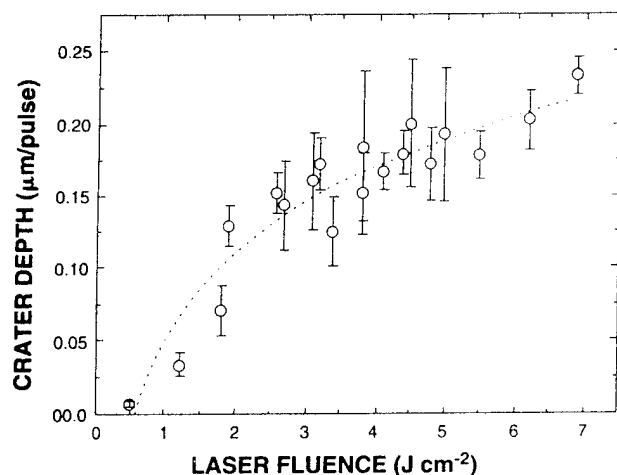


FIG. 2. The crater depth per laser pulse as a function of laser fluence for GeO_2 targets irradiated in vacuum. The fit to the data produced a ablation threshold fluence of 0.46 J cm^{-2} .

a threshold fluence of 0.46 J cm^{-2} . The absorption coefficient from the fit was within 35% of the accepted value for GeO_2 at 193 nm .¹⁹

The ablation threshold determined using the above procedure was corroborated by examining the optical emission produced from laser ablated targets. By varying the laser fluence on the target and monitoring the intensities of neutral Ge transitions using the 304, 288, 265, and 252 nm emission lines, the minimum detectable atomic emission occurred near 0.5 J cm^{-2} .

B. Plume emission characteristics

Time-integrated emission spectra of a plume generated by irradiating a GeO_2 target with a laser fluence of 6.5 J cm^{-2} at a base pressure of 4×10^{-6} Torr are shown in Fig. 3. The transitions associated with each spectral feature in this figure are listed in Table I. This figure illustrates the dramatic change in the plasma emission as the collection position is changed from the target surface to 5 cm away. At $z=0.2 \text{ cm}$, the emission consisted of features associated with both Ge I and Ge II atoms superimposed onto a continuum background. The ion lines appeared very broad and had intensities comparable to the neutral line intensities. The continuum background significantly decreased and the Ge I emission lines became much narrower 1 cm away from the target surface. The Ge II features were reduced in intensity relative to the neutral lines and remained broad. At 3 cm from the "0" position, the emission was dominated by Ge I transitions with a small contribution from the ionic species. Finally, the Ge II features disappeared at $z=5 \text{ cm}$ and the plume radiated solely from electronically excited states of Ge I atoms.

The discrete emission lines observed in this study primarily consisted of transitions originating from electronic states involving neutral and singly ionized Ge atoms. Most of the neutral transitions originated from the $4p^2-4p5s$ configuration. As shown in Table I, however, transitions originating from higher lying electronic states in Ge I were detected in

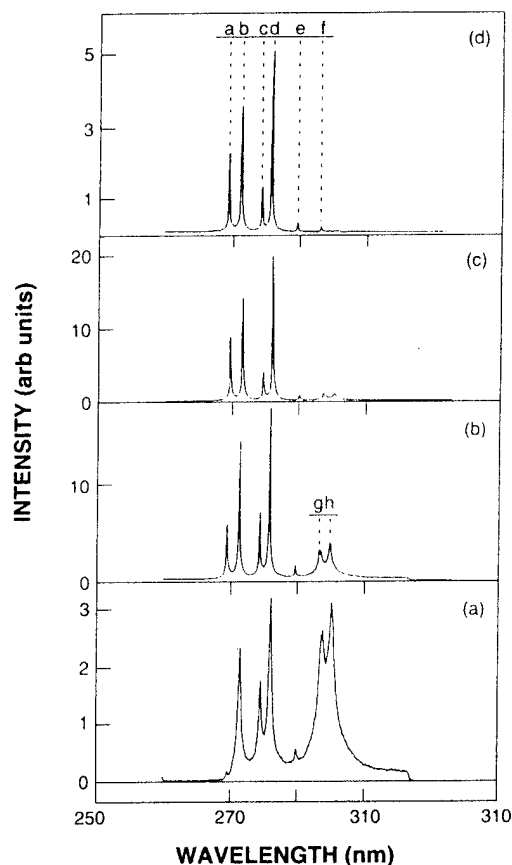


FIG. 3. Plasma emission spectra of material ablated from a GeO_2 target in vacuum (4×10^{-6} Torr) at $F=6.5 \text{ J cm}^{-2}$. The spectra are labeled according to distance from the target surface: (a) $z=0.2 \text{ cm}$, (b) $z=1.0 \text{ cm}$, (c) $z=3.0 \text{ cm}$, and (d) $z=5.0 \text{ cm}$. The transitions labeled a–h are summarized in Table I. Although the intensities have arbitrary units, the relative magnitudes are preserved in the plots in order to compare line intensities at different locations.

these plumes. The emissions from Ge II were comprised of the following transitions: $5s^2S-5p^2P^0$, $5p^2P^0-6s^2S$, $5p^2P^0-5d^2D$, and $4d^2D-4f^2F^0$. Higher-energy transitions associated with Ge III could not be observed due to the detection limits imposed by the spectrometer and the diode array. Examination of the spectrum at long wavelengths also

TABLE I. Details of the atomic transitions^a associated with the emission lines depicted in Fig. 3.

Label	Species	Transition wavelength (nm)	Transition	$E_{\text{lower}} (\text{cm}^{-1})$	$E_{\text{upper}} (\text{cm}^{-1})$
a	Ge I	269.13	$4p^2\ ^3P_1-5s^3P_1$	557	37 702
b	Ge I	270.96	$4p^2\ ^3P_1-5s^3P_0$	557	37 452
c	Ge I	274.04	$4p^2\ ^1S_0-4d^1P_1$	16 367	48 962
d	Ge I	275.46	$4p^2\ ^3P_2-5s^3P_1$	1410	37 702
e	Ge I	279.39	$4p^2\ ^1S_0-6s^3P_1$	16 367	52 148
f	Ge I	282.90	$4p^2\ ^1S_0-4d^3P_1$	16 367	51 705
g	Ge II	283.18	$4p^2\ ^2D_{3/2}-4f^2F_{5/2}$	65 015	100 317
h	Ge II	284.55	$4p^2\ ^2D_{5/2}-4f^2F_{7/2}$	65 184	100 316

^aFrom Ref. 16.

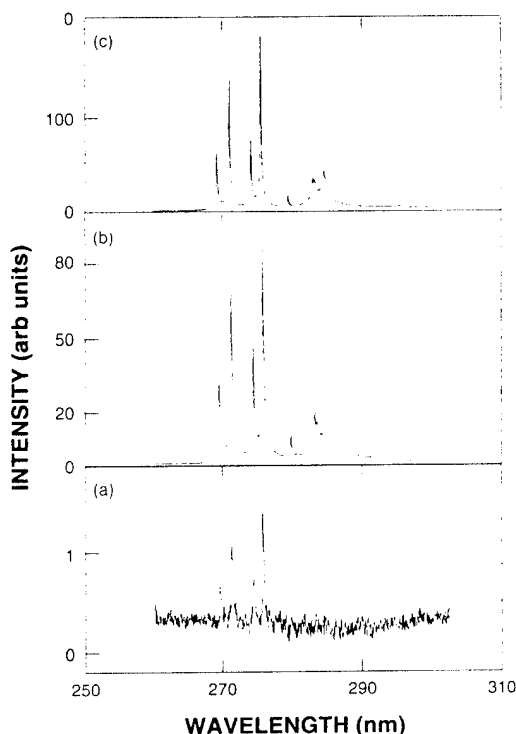


FIG. 4. Plume emission features recorded at three laser fluences: (a) 0.5 J cm^{-2} , (b) 1.0 J cm^{-2} , and (c) 6.5 J cm^{-2} . The spectra were obtained in vacuum at $z=1 \text{ cm}$.

revealed emissions originating from electronically excited, neutral atomic oxygen (O^*1). (Note: the * symbol will be used to specifically designate electronically excited states.) Molecular emission from GeO was not detected under any of the conditions utilized in these experiments.

The main spectral features of the plume remained the same over the range of fluences utilized in this work. That is, the nature of the emitting states from the neutral species and ions with the same degree of ionization did not change with distance from the target surface regardless of laser fluence. However, the intensities of the atomic lines were sensitive to the laser fluence as illustrated in Fig. 4. No discrete ion emission features were observed at $F < 1 \text{ J cm}^{-2}$ regardless of the position from the target surface or the pressure of the ambient gas. However, neutral emission did appear at laser fluences as low as 0.5 J cm^{-2} but the emission was extremely weak at $z \leq 0.5 \text{ cm}$. Since no ion state emission was observed at these laser fluences, the electronically excited neutrals were presumably dissociated directly from the target surface and these states were probably not formed via ion recombination reactions. Continuum emission, which has been frequently observed in laser generated plumes near the target surface, was conspicuously absent during ablation in vacuum at $F \leq 1 \text{ J cm}^{-2}$. As the fluence increased from 0.5 to 1.0 J cm^{-2} , the neutral line intensities increased by a factor of 15 while a much slower increase (factor of 2) was observed between 1.0 and 6.5 J cm^{-2} for both the Ge I and Ge II emission lines. Although the intensities of the individual atomic

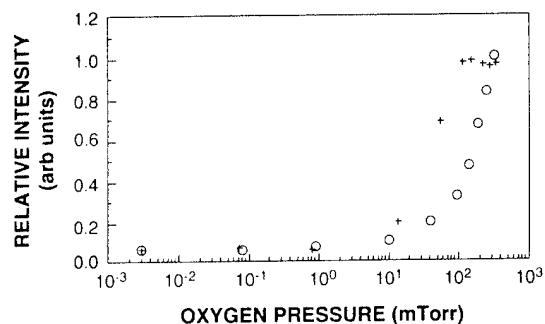


FIG. 5. Relative intensity behavior of the Ge I 269.1 nm emission line (+) and the Ge II 283.2 nm emission line (O) as a function of the oxygen pressure. The Ge I intensities are obtained at $z=3 \text{ cm}$ and the Ge II intensities are recorded at $z=1 \text{ cm}$. Both data have been obtained with a laser fluence of 6.5 J cm^{-2} . These trends are common to all other neutral and ion Ge emissions recorded in these studies.

lines varied with laser fluence, the relative intensities of spectral features remain unchanged. This implied that the local equilibrium was maintained among the energy levels regardless of the laser fluence.

The presence of an ambient gas dramatically affected the plasma characteristics. Figure 5 summarizes the general trend in the relative emission intensities versus O_2 pressure. The neutral line intensities in this figure were recorded at $z=3 \text{ cm}$ while the ion data were obtained at $z=1 \text{ cm}$ and both data sets were produced with a laser fluence of 6.5 J cm^{-2} . The intensities of both Ge I and Ge II lines, which were proportional to the excited state number densities of the respective species, remained relatively constant over four orders of magnitude change in O_2 pressure. The neutral emission intensities increased by a factor of 10 between 10 and 100 mTorr, and subsequently approached a constant value above 100 mTorr of added O_2 . Clearly, the higher oxygen pressures caused a considerable enhancement in the neutral populations. The ion emission behavior was different at O_2 pressures above 10 mTorr: the ion state intensity monotonically increased but showed no indication of leveling or decreasing at the highest pressures used in these studies. The intensities recorded at 120 mTorr were a factor of 10 greater than those obtained at the lowest pressures. Similar trends were observed for data recorded with a laser fluence of 1 J cm^{-2} for both Ge I and Ge II.

The dynamics of laser produced plumes are partially governed by the backing pressure of an ambient gas.²⁰ In vacuum,²¹ the plume is allowed to expand freely in a forward-directed pattern with a $(\cos \theta)^n$ functional dependence, where n typically ranges from 10 to 40. However, the propagation of the plume is modified even at moderate backing pressures resulting in a narrowing of the plume and a subsequent increase in n to a value as high as 200. In this study, the addition of 100–150 mTorr of O_2 forced the plume to appear constricted and more spatially confined than in vacuum. This effect could cause the number of emitters per unit volume to increase within the observation region resulting in an apparent increase in the emission intensities at higher O_2 pressures. This mechanism, which could account

5

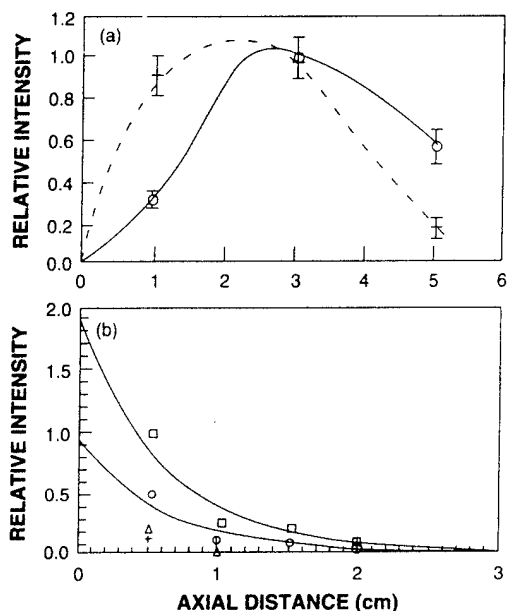


FIG. 6. The relative line intensities of Ge I and Ge II vs distance from the target surface: (a) shows the Ge I (312.5 nm transition) behavior at two pressures (+) vacuum and (O) 200 mTorr of O₂; (b) illustrates the Ge II (602.1 nm transition) dependence in vacuum (+), $P(\text{O}_2)=1$ mTorr (Δ), $P(\text{O}_2)=84$ mTorr (O), and $P(\text{O}_2)=170$ mTorr (\square). A laser fluence of 6.5 J cm^{-2} has been utilized to obtain these data. All other neutral and ion emission features follow the trends depicted in this figure.

for the trends displayed in Fig. 5, was tested by simulating a change in the pressure gradient in the plume by using different laser spot sizes at a constant fluence. A tight laser focus causes a high-pressure gradient across the plume which forces a stronger expansion than a softer focus at the same fluence. Thus, focusing the laser spot more softly should produce a similar effect as that created by increasing the background gas; namely, the shorter extent of the expansion should keep more emitting atoms confined to a smaller volume. Under these conditions, the experiments showed that the ratios of spectral line intensities for the soft focus to the tight focus increased by 10%–30%. Spatial confinement could partially account for the pressure-dependent intensities, but other processes uncovered after examining the behavior of the oxygen atom line intensities versus O₂ pressure may dominate as discussed below.

Figure 6 shows relative axial intensity distributions at successive distances from the target surface at two pressures. In Fig. 6(a), the Ge I line intensities recorded in vacuum reached their maximum values 1.5–2.0 cm from the target surface and the position of the maximum intensity shifted to 2.5–3.0 cm at an O₂ pressure of 200 mTorr. Although the data were recorded only at $z \leq 5$ cm, the emission was observable to at least 7 cm from the target surface at all pressures. The ion emission, however, had a peak intensity near the target surface and exponentially decayed over distance as illustrated in Fig. 6(b). In vacuum, the ion emission was recorded out to ~ 0.5 –1.0 cm from the target surface, where the signal levels fell below the detection limits of the experiment, whereas increases in the O₂ pressure resulted in detect-

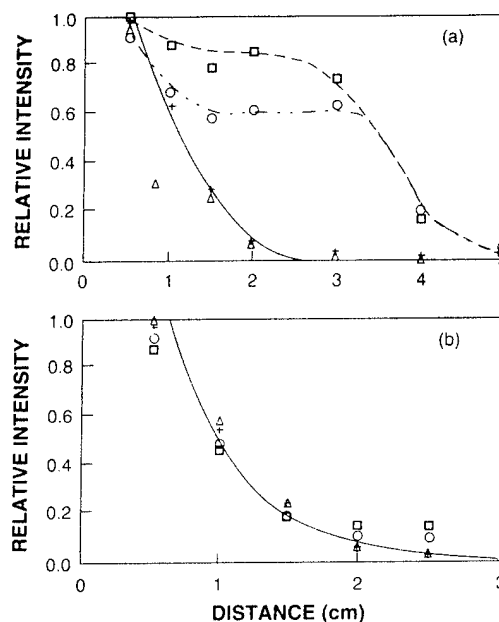


FIG. 7. The evolution of the 844.6 nm atomic oxygen line vs distance from the target surface at $F=6.5 \text{ J cm}^{-2}$: (a) illustrates the behavior in O₂ while (b) shows the effect of N₂ as the ambient gas. The gas pressures in each figure are: (+) vacuum, (Δ) 1 mTorr, (O) 84 mTorr, and (\square) 170 mTorr. All data have been normalized to the intensity measured at $z=0.2$ cm.

able signals as far out as $z=3$ cm. Exponential density profiles have been used in gas dynamic simulations in the adiabatic expansion region of a plasma,²² and these results may support this picture of a nonthermal plume expansion. The laser fluences affect the intensity distribution only to a minor extent; the brightest regions of the plume appear in the same location and to the same extent.

The trends observed for atomic oxygen are contrary to those observed with Ge. Figure 7(a) shows the evolution of the 844.6 nm emission line from atomic oxygen. In the O₂ pressure range $0 \text{ mTorr} \leq P(\text{O}_2) \leq 1 \text{ mTorr}$, the O I emission rapidly decreased to negligible values at ~ 3 cm from the target surface. The O I emission observed under these conditions was clearly a product of electronic excitation of atomic oxygen due to the ablation process because, at these pressures, the relatively low collision frequency prohibited any significant interaction between the oxygen added to the chamber and the plume material. At higher pressures, however, the O I emission intensity displayed a small decrease but attained a constant value in the region $1.5 \text{ cm} \leq z \leq 3 \text{ cm}$. The O* I populations subsequently decayed at $z > 3$ cm and finally became undetectable near $z=5$ cm. The behavior of the emissions at higher pressures could be caused by an increased residence time in the observation region as discussed previously. However, the 40 ns radiative lifetime of this transition ($^3S_0 - ^3P$) limited the travel distance to ≤ 1 mm before decaying, assuming a typical velocity of 10^6 cm s^{-1} found in laser generated plumes. The high-pressure results demonstrated that additional O* I production mechanisms must exist to account for the observed behavior.

In order to better understand the intensity behavior described in Fig. 7(a), the O I emission was monitored as a function of N_2 pressure to check whether or not additional excited oxygen atoms were being produced in reactions between the plume material and the ambient molecular oxygen. Figure 7(b) shows that the relative O*I number density remained constant at a fixed location from the target as the N_2 pressure increased from 0 to 150 mTorr. However, the O I emission decreased exponentially with distance with the same functional dependence at each pressure. Thus, the presence of O_2 acted as a source of additional atomic oxygen and this trend also revealed that the O*I dependence on the O_2 pressure was not a residence time effect.

IV. DISCUSSION

The ablation of GeO_2 glass can be partially explained by considering the optical and thermal properties of the irradiated material. The removal of material from a target by laser irradiation depends on the coupling efficiency of the laser beam energy to the target. The absorption coefficient, α of GeO_2 at 6.4 eV (193 nm) is $2 \times 10^5 \text{ cm}^{-1}$ which corresponds to an absorption depth of $\sim 50 \text{ nm}$.¹⁹ For "congruent evaporation," the heat diffusion distance δ must be smaller than the absorption depth. We can estimate the heat diffusion depth using typical values for the thermal conductivity^{23,24} ($K=0.015 \text{ W cm}^{-1} \text{ K}^{-1}$) and the specific heat²⁵ ($C_p=0.19 \text{ cal g}^{-1} \text{ K}^{-1}$) for glass at 300 K. On a time scale comparable to the laser pulse duration ($\tau=28 \text{ ns}$), $\delta=[(2D\tau)^{1/2}]$ is calculated to be $\sim 170 \text{ nm}$, where $D=K/\rho C_p$ and $\rho=3.68 \text{ g cm}^{-3}$ for GeO_2 glass.²⁵ Thus, the energy absorbed during the laser irradiation time is confined to a surface layer corresponding to the thermal diffusion length.

When energy densities above the vaporization threshold are applied to the target, the laser energy is not only absorbed in a surface layer of $\sim 50 \text{ nm}$ but intense local heating also occurs within a distance of 170 nm which can lead to additional material vaporization. In these experiments, the laser ablation threshold was near 0.46 J cm^{-2} based on the results of both the optical emission studies and crater formation on the target surface. The surface temperature on the target is estimated at this fluence using a simplified approximation to the heat diffusion equation in one dimension described by Ready²⁶ given in Eq. (2).

$$T(z=0, \tau) = (2\Phi_0/K)(D\tau/\pi)^{1/2}, \quad (2)$$

where $\Phi_0=(\Phi/\tau)(1-R)$, Φ is the laser flux, and R is the reflectivity ($R \approx 0.12-0.13$ for GeO_2 at 6.4 eV).¹⁹ Using the thermodynamic values defined above, the upper limit to the surface temperature at the end of the laser pulse for a fluence of 0.46 J cm^{-2} is $\sim 7000 \text{ K}$. This value is greater than the liquid transition temperature ($T_{liq} \approx 2625 \text{ K}$) for GeO_2 , so removal of material from the target should occur within the thermal diffusion length. By scaling $T(z=0, \tau)$ with Φ , Eq. (2) suggests that ablation threshold may be lower than 0.46 J cm^{-2} . In order to achieve the liquid transition temperature of GeO_2 , Eq. (2) predicts that the laser must deposit an energy density of 200 mJ cm^{-2} .

The interaction of the laser with the solid surface produces electrons and ions in addition to copious amounts of

neutrals. The number density of these species has a complex evolution and they depend on the irradiation conditions, the collisional kinetics in the plume, and the distance from the target surface. The most important result of this study is the pronounced effect on the plume's luminescence and, thus, the number densities of individual species, caused by the presence of molecular oxygen. At O_2 pressures below 10 mTorr, both Ge^*II and O^*I decay exponentially from the target surface. In addition, the Ge I emission peaks when the Ge^*II and O^*I concentrations reach their minimum values near $z=2 \text{ cm}$. These results imply the existence of a neutral-ion conversion mechanism to explain the delayed peaking of the Ge I emission intensity. At these low pressures, the equilibrium mean-free path (MFP) between O_2 and Ge is $>1 \text{ cm}$ so collisional interactions between these species or other plume constituents with the ambient could be eliminated. Therefore, electron-ion or electron-atom interactions within the plume may explain the increase in the Ge^*I number density at the expense of the ions and atomic oxygen.

Both the neutral and ion state concentrations begin to increase near 20–30 mTorr of added O_2 . This threshold also coincides with an increase in the O I emission. At these pressures, the MFP is typically 1–2 mm; thus, the increase in the neutral atom concentrations appear to be linked with higher collision frequencies which makes the reaction $Ge(I \text{ or } II) + O^*I \rightarrow Ge^*(I \text{ or } II) + O$ more probable. The ion emission, however, remains confined to within about 1–1.5 cm of the target surface where electron densities are higher which possibly promote e^- -atom ionization processes to account for the increase in the ion state populations.

The ablation of GeO_2 at high ambient pressures [$P(O_2) > 10 \text{ mTorr}$] not only produces O^*I directly as a result of the ablation process, but also increases the excited O atom concentration through plume- O_2 interactions. The magnitude of the cross sections for e^- - O_2 collisions resulting in the dissociation of O_2 into various excited atomic products range from 2.2×10^{-17} to $6.6 \times 10^{-17} \text{ cm}^2$ for electron energies ranging between 13.5 and 33.5 eV.²⁷ These values translate into relatively efficient collisional dissociation if the electron kinetic energies are in the appropriate range. The ablation of targets containing Ge is known to produce atomic species with average kinetic energies of 40–100 eV.^{15,28} The accompanying electrons are expected to have higher kinetic energies than the atomic species which makes O_2 dissociation by electron impact highly probable.

The maximum emission intensity is determined by the collisional excitation mechanisms and the radiative lifetimes at the higher ambient gas pressures. Collisional interactions between the plume and the ambient O_2 clearly increase the concentrations of excited Ge I and Ge II over those observed at the low ambient pressures. In addition to e^- -atom collisions which can produce more ions in the plume, excited O atoms can interact with Ge atoms to produce electronically excited Ge. The presence of an O^*I creation process, therefore, makes this event more probable. The excited species are also observed farther from the target surface at high pressures which implies that the processes responsible for production of these excited states have a spatial dependence.

The results of this study impact the understanding of

stoichiometric GeO_2 thin-film formation. Different deposition conditions typically lead to variations in plasma luminescence and the details of the emission spectra can identify conditions for producing high-quality thin films. In an earlier work,¹⁴ we found that stoichiometric GeO_2 thin films could be produced at high ambient O_2 pressures (150 mTorr). Furthermore, these studies showed that stoichiometric films were produced only when the substrate was physically located within the plume and films grown outside the plume have been found to be oxygen deficient. The results presented here demonstrate that high pressures of O_2 increase the number density of excited neutrals atoms and excited ion states. This implies that the higher-energy content of the plume is necessary for producing quality films. By placing the substrate within the plume [typically 4 cm at $P(\text{O}_2)=150$ mTorr], the substrate is bombarded by O I, Ge I, and Ge II atoms in various electronic states as well as by molecular oxygen in the ambient. Reactions of these species in the gas phase and/or on the substrate surface promote the proper oxygen incorporation in these films.

V. CONCLUSIONS

The plume generated from 193 nm irradiation of GeO_2 targets was examined by recording dispersed emission in the UV to visible regions. The emission spectra were recorded as a function of laser fluence, distance from the front surface of the target, and molecular oxygen pressure. The ablation rate of GeO_2 was also determined in this work. Neutral and singly ionized atomic species were observed in the plume and the emission intensities of these species depended on both the O_2 pressure and distance from the front surface of the target. The behavior of the emission intensities of these species were directly connected to the excited atomic oxygen concentrations which was produced as a by-product of the ablation process in vacuum and as a product of plume- O_2 interactions at higher ambient gas pressures. The change in the plume's concentration of excited species by ambient O_2 affected the film growth by producing additional energetic species that impacted the substrate which subsequently incorporated stoichiometric proportions of oxygen in the film structure. Because the excited species responsible for the plume luminescence represents only a small fraction of the material removed from the target, we are currently utilizing laser induced fluorescence to obtain information on the dynamics and kinetics of the nonemitting species in the plasma.

ACKNOWLEDGMENTS

I would like to thank Steven Ramsey for his technical assistance during these experiments and the fruitful discussions with Dr. Brian Patterson and Dr. Sarath Witanachchi.

- ¹ J. T. Cheung and H. Sankur, *CRC Crit. Rev. Solid State Mater. Sci.* **15**, 63 (1988).
- ² G. Mehlman, D. B. Chrisey, P. D. Burkhalter, J. S. Horwitz, and D. A. Newman, *J. Appl. Phys.* **74**, 53 (1993).
- ³ G. Mehlman, D. B. Chrisey, J. S. Horwitz, P. D. Burkhalter, R. C. Y. Auyeung, and D. A. Newman, *Appl. Phys. Lett.* **63**, 2490 (1993).
- ⁴ Q. Y. Ying, D. T. Shaw, and H. S. Kwok, *Appl. Phys. Lett.* **53**, 1762 (1988).
- ⁵ X. D. Wu, B. Dutta, M. S. Hegde, A. Inam, T. Venkatesan, E. W. Chase, C. C. Chang, and R. Howard, *Appl. Phys. Lett.* **54**, 179 (1989).
- ⁶ O. Auciello, S. Athavale, O. E. Hankins, M. Sato, A. F. Schreiner, and N. Biunno, *Appl. Phys. Lett.* **53**, 72 (1988).
- ⁷ G. Koren, A. Gupta, and R. Bassman, *Appl. Phys. Lett.* **54**, 2035 (1989).
- ⁸ P. E. Dyer, A. Issa, and P. H. Key, *Appl. Phys. Lett.* **57**, 186 (1990).
- ⁹ J. Seth, R. Padiyath, and S. V. Babu, *Appl. Phys. Lett.* **63**, 126 (1993).
- ¹⁰ H. Sankur, J. G. Nelson, A. J. Pritt, Jr., and W. J. Gunning, *J. Vac. Sci. Technol. A* **5**, 15 (1987).
- ¹¹ P. J. Wolf, *J. Appl. Phys.* **72**, 1280 (1992).
- ¹² J. T. Knudtson, W. B. Green, and D. G. Sutton, *J. Appl. Phys.* **61**, 4771 (1987).
- ¹³ S. Deshmukh, E. W. Rothe, and G. P. Reck, *J. Appl. Phys.* **66**, 1370 (1989).
- ¹⁴ P. J. Wolf, T. M. Christensen, N. G. Coit, and R. W. Swinford, *J. Vac. Sci. Technol. A* **11**, 2725 (1993).
- ¹⁵ F. Vega, C. N. Afonso, and J. Solis, *J. Appl. Phys.* **73**, 2472 (1993).
- ¹⁶ J. Reader, C. H. Corliss, W. L. Wiese, and G. A. Martin, "Wavelength and Transition Probabilities for Atoms and Atomic Ions," NSRDS-NBS 68 Parts I, II, Washington, DC, 1980; M. M. Miller and R. A. Roig, *Phys. Rev. A* **7**, 1208 (1973); J. Lotrain, J. Cariou, Y. Guern, and A. Johannin-Gilles, *J. Phys. B* **11**, 2273 (1978).
- ¹⁷ G. A. Capelle and J. M. Brom, Jr., *J. Chem. Phys.* **63**, 5168 (1975).
- ¹⁸ W. L. Wiese, M. W. Smith, and B. M. Glennon, "Atomic Transition Probabilities," NSRDS-NBS-4, Vol. I, Washington, DC, 1966.
- ¹⁹ L. Pasajova, *Czech. J. Phys. B* **19**, 1265 (1969).
- ²⁰ D. B. Geohegan, *Appl. Phys. Lett.* **60**, 2732 (1992).
- ²¹ D. J. Lichtenwalner, O. Auciello, R. Dat, and A. I. Kingon, *J. Appl. Phys.* **74**, 7497 (1993).
- ²² R. K. Singh and J. Narayan, *Phys. Rev. B* **41**, 8843 (1990).
- ²³ *Handbook of Physics* (McGraw-Hill, New York, 1958).
- ²⁴ *Handbook of Chemistry and Physics*, 65th ed. (CRC, Boca Raton, FL, 1984).
- ²⁵ N. M. Ravindra, R. A. Weeks, and D. L. Kinser, *Phys. Rev. B* **36**, 6132 (1987).
- ²⁶ J. F. Ready, *Effects of High-Power Laser Radiation* (Academic, New York, 1971), p. 73.
- ²⁷ P. C. Cosby, *J. Chem. Phys.* **98**, 9560 (1993).
- ²⁸ D. Lubben, S. A. Barnett, K. Suzuki, S. Gorbalkin, and J. E. Greene, *J. Vac. Sci. Technol. B* **3**, 968 (1985).

8

Photodissociation dynamics of S_4N_4 at 222 and 248 nm

Andrew P. Ongstad,^{a)} Robert I. Lawconnell,^{b)} and Thomas L. Henshaw
 Frank J. Seiler Research Laboratory, United States Air Force Academy, Colorado Springs,
 Colorado 80840-6528

(Received 30 September 1991; accepted 10 April 1992)

Emission from several electronically excited states of NS is observed when the energetic molecule S_4N_4 is photolyzed with radiation from an excimer laser. Photolysis at 248 nm generates fluorescence from the $B^2\Pi_{1/2,3/2}$, $H^2\Pi_{1/2}$, $G^2\Sigma^-$, and $I^2\Sigma^+$ states of NS. NS($B^2\Pi_{1/2,3/2}$) and NS($C^2\Sigma^+$) fluorescence is observed when the photolysis wavelength is changed to 222 nm. The NS(H) and NS(C) spectra are postulated to arise from a resonant interaction between the KrF and KrCl excimer photons, respectively, and vibrationally hot ground state NS. LIF excitation scans on the NS $X^2\Pi_{1/2,3/2} \rightarrow B^2\Pi_{1/2,3/2}$ system confirm the production of rotationally and vibrationally excited NS(X) up to $v''=4$. A mechanism, based on the experimental data (i.e., spectral composition, laser fluence studies, excited state time histories), calculated heats of formation, and Gaussian molecular orbital calculations, is proposed to account for the observed emissions. For photolysis at 248 nm it is hypothesized that a two photon absorption promotes the ground singlet state of S_4N_4 to an upper repulsive singlet state, which rapidly dissociates ($\tau \leq 30$ ns), producing an acyclic S_3N_3 fragment and vibrationally excited monomeric NS(X). The photofragments can interact further with the excimer radiation to produce NS(B) and NS(H), respectively. A similar mechanism is proposed to account for the presence of the NS(B) and NS(C) excited states for the 222 nm photolysis.

I. INTRODUCTION

The nitrogen sulfide radical is an unstable radical which cannot be stored as a monomeric liquid or solid, and must be produced *in situ* in the gas phase. NS is isoelectronic with NO and PO, and as expected, it shares many analogous states with these diatomics. For example, the NS $B^2\Pi$ and $C^2\Sigma^+$ electronic states have the well-known NO $B^2\Pi$ and $A^2\Sigma^+$ electronic states as their analogs, respectively. In both molecules, these states give rise to the β and γ band emission, respectively. However, the NO β bands lie significantly higher in energy (approximately 40 000 cm^{-1}) than the NS($B^2\Pi$) which lie near 30 000 cm^{-1} . The γ bands of both molecules are nearly resonant in energy, lying near 43 000 cm^{-1} .

Practical investigations involving NS are not nearly as numerous as the isovalent nitric oxide, which is known to play key roles in both combustion and atmospheric chemistry. However, the radical has been detected in atmospheric pressure flames by LIF methods,¹ and it has been detected in interstellar clouds via radio frequency emission.^{2,3} The suggestion has also been made that NS may act as the active gain media in an electronic transition laser.^{4,5} Specifically, the NS($B^2\Pi$) state of the molecule has been characterized as an attractive upper laser level primarily due to its significant Franck-Condon shift with respect to the NS ground state potential well.

Fluorescent emissions from NS are typically generated by reacting active nitrogen with a sulfur compound (e.g., H_2S , S_2Cl_2 , SCl_2) in a discharge flow reactor. Such emis-

sions have produced a wealth of spectroscopic and kinetic data. For example, the spectroscopy of the $B^2\Pi$ state has been well characterized with detailed measurements of Franck-Condon factors,⁶ r centroids,⁷ vibrational transition probabilities,⁸ and perturbations.⁹ Collisional quenching and vibrational energy transfer rates have also been measured for several collider gases.^{10,11} Less information is available on the higher lying doublet states (e.g., $A^2\Delta$, $H^2\Pi$, $C^2\Sigma^+$), although studies utilizing pulsed laser techniques have begun to detail the spectroscopy of these more energetic states.⁸ In this regard, we have recently reported on the KrF laser photolysis of the inorganic cage compound tetrasulfur tetranitride.¹² S_4N_4 may be regarded as a labile polymer composed of four thiazyl (NS) units (see inset to Fig. 1).¹³ The photolysis produced fluorescent emission from several of the more energetic NS states including the $H^2\Pi_{1/2}$, $G^2\Sigma^-$, and $I^2\Sigma^+$. Strong NS($B^2\Pi$) emission was also observed, and measurements indicated the overall efficiency of conversion of absorbed photons by S_4N_4 into NS($B^2\Pi$) was $2.6\% \pm 0.7\%$. The facile photodecomposition process observed at 248 nm may be attributed to the energetic nature of S_4N_4 [$\Delta H_f(\text{solid}) = 110 \text{ kcal mol}^{-1}$],¹⁴ the molecules large absorption cross section at 250 nm ($\sigma = 4.8 \times 10^{-17} \text{ cm}^2$), and the excellent energy overlap of the KrF excimer laser with the 250 nm absorption band.

This study extends and supplements our initial investigation, and we report on further measurements at the 248 nm photolysis wavelength, our LIF studies on the production of ground state NS(X), and on the fluorescent emission and products observed in the photolysis at 222 nm. A mechanism, based on the experimental observations (spectral composition, excited state time histories, fluence stud-

^{a)}Present address: Phillips Laboratory/LIDA, Kirtland Air Force Base, Albuquerque, New Mexico 87117.

^{b)}Present address: Mathematics Department, USAFA, Colorado 80840.

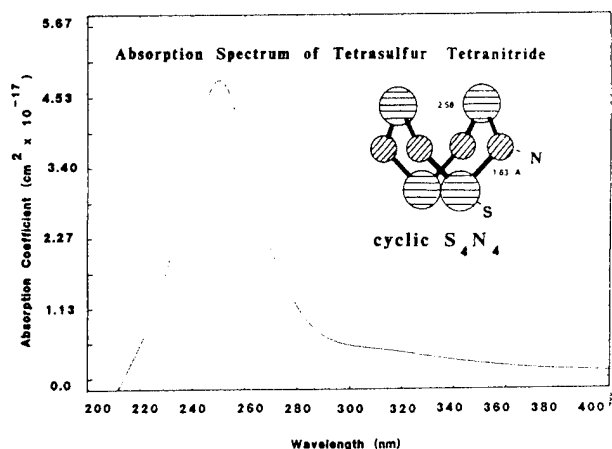


FIG. 1. UV-visible absorption spectrum of 2.92×10^{-5} M S_4N_4 in acetonitrile. The inset figure shows the cage like structure of S_4N_4 .

ies, etc.), thermochemistry, and *ab initio* calculations, is proposed to account for the observed excited state and ground state products.

II. EXPERIMENT

The experimental apparatus consists of three general sections including the photolysis chamber, the detection ensemble, and the photolysis and probe lasers.

The photolysis chamber is constructed from a cylindrical piece of aluminum tubing 25 cm in length with an inside diameter of 3.5 cm. MgF_2 windows glued to the tubes end allow for the transmission of the laser radiation. LIF emissions originating within the cell were viewed off axis, at the cells center through MgF_2 windows. The S_4N_4 (typically ≤ 1 g) was contained in a small 10 ml pyrex flask, which was connected to the chamber through a 12 mm side port. Nichrome wire wrapped around the neck of the flask, and a small heating mantle placed underneath the flask allowed for gentle heating/increased sublimation of the S_4N_4 . Recrystallization of the tetramer on the cell surfaces was prevented by wrapping the cell with heating tape and heating the surface to near 70°C . Flow through the cell was generated by a mechanical pump whose free air displacement was 500 l min^{-1} . To insure a new fill of S_4N_4 on every laser shot a flow of uhp helium buffer gas sufficient to flush the cell every 0.1 s was introduced slightly upstream of the S_4N_4 reservoir. The temperature of the He bath gas, measured at the center of the cell, was near 65°C . The total pressure in the photolysis zone was measured with a capacitance manometer and was maintained in the range 0.8 to 1.2 Torr. The pressures of sublimed S_4N_4 were typically ≤ 10 mTorr. Helium flow rates were measured with a calibrated mass flow meter.

The NS radicals produced in the photolysis were monitored by recording the LIF excitation spectrum of the $X^2\Pi \rightarrow B^2\Pi$ transition using a Nd:YAG pumped pulsed dye laser (PDL) with attendant frequency doubling. The

bandwidth of the frequency doubled radiation was near 0.01 nm. Pulse energies $\leq 100 \mu\text{J/pulse}$ were employed in the LIF scans.

Photolysis of S_4N_4 was carried out with a excimer laser operated on KrF (248 nm) or KrCl (222 nm). The full-width at half maximum (FWHM) pulse width of this laser was 1 nm. The fluence of the excimer laser was varied from $1\text{--}85 \text{ mJ cm}^{-2}$. The PDL could be delayed from 0.5 to 255 μs from the photolysis pulse. The actual minimum delay was limited to $\sim 2 \mu\text{s}$ due to the presence of prompt NS(*B*) fluorescence. The photolysis and probe lasers were arranged to counter propagate through the gas medium, the cross section of the photolysis beam being much larger than that of the probe beam. The LIF was filtered and detected by either a 1P28 or a R1463-01 photomultiplier tube (PMT), with the latter tube specific for photon counting. The signals from the PMT were sent, without amplification, straight to a gated photon counter operated in the boxcar mode. The photon counter was interfaced to a 80286 personal computer for data collection and manipulation. The spectral response of the dye laser/filter/PMT combination was measured, and used to correct the LIF excitation spectra. Spectra of the prompt emissions produced by the photolysis were recorded by replacing the bandpass filter with a 0.5 m monochromator. Alternatively, prompt emissions were dispersed with a 0.25 m polychromator and detected with a 1024 element silicon diode array. Calibration of the systems spectral sensitivity was performed with an Optronics Laboratory deuterium lamp and standard lamp.

The time histories of the emissions were collected with a 100 MHz oscilloscope which was interfaced via a GPIB to the 80286 PC. Storage and manipulation of the temporal traces were performed with Asystant/GPIB software.

S_4N_4 was prepared by reacting sulfur(II)chloride with NH_3 in CCl_4 solution, according to the method given by Villena-Blanco and Jolly.¹⁵ The S_4N_4 , formed in the reaction



was isolated by a soxhlet extraction with dry dioxane. On cooling large orange S_4N_4 crystals appeared, which were filtered and dried in air. The purity of the material was checked by FTIR and uv-vis. and indicated no appreciable impurities aside from traces of sulfur. A typical uv-vis. spectrum of S_4N_4 in acetonitrile is given in Fig. 1, and shows one primary unresolved vibronic band centered near 250 nm and a secondary much less intense feature (~ 310 nm) to the red of the primary. The main uv band at 250 nm has been attributed to either an $n \rightarrow \pi^*$ transition in NS¹⁶ or to a $\sigma \rightarrow \sigma^*$ transition in the S-S interaction.¹⁷ The 250 nm band has a large absorption cross section of $4.8 \times 10^{-17} \text{ cm}^2$. Deeper in the uv, an additional strong absorption is observed close to 185 nm. The gas¹² and solution phase spectra are nearly identical.

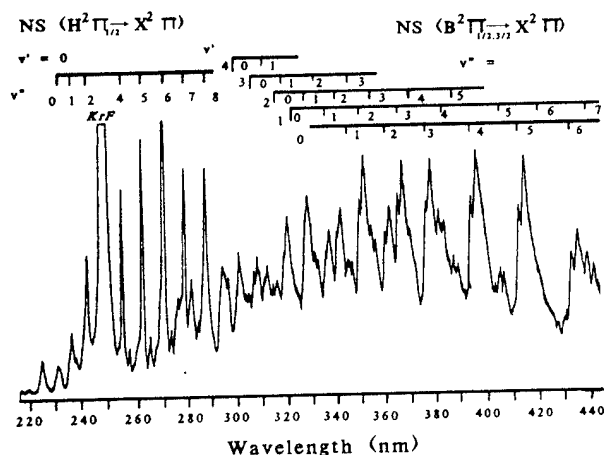


FIG. 2. Emission spectrum produced at the 248 nm photolysis wavelength. The broad band near 248 nm is due to the KrF laser spike.

III. RESULTS

A. Photolysis at 248 nm

On photolysis of ~ 10 mTorr of S_4N_4 a bright blue emission was clearly visible to the eye. Figure 2 shows the spectrum of this prompt emission collected with the 0.25 m polychromator/diode array assembly. The emission extends from the uv (~ 200 nm) into the green (~ 550 nm) and comprises two distinct band systems. The broader and more extensive double headed band system was readily identified as $NS(B^2\Pi_{1/2,3/2} \rightarrow X^2\Pi_{1/2,3/2})$, and shows the characteristic $1/2-3/2$ spin orbit components ($A_0 = 90$ cm^{-1}). A second much sharper spectral progression is evident in the 200–330 nm region. By comparison of the vibrational term values calculated for these bands and by comparison of the band frequencies with the known electronic states of NS, a single progression originating out of $v'=0$ for $NS(H^2\Pi_{1/2} \rightarrow X^2\Pi_{1/2})$ was identified. We have recently completed a detailed analysis of this system, reporting on the Franck-Condon factors, r centroids, radiative lifetime, and collisional quenching constants of various species with the $NS(H^2\Pi)$ state.¹² As is evident in the spectrum, the 248 nm laser radiation strongly overlaps the $H_{1/2}(0,3)$ transition near 248.41 nm. The large Franck-Condon factor (FCF) calculated for this band¹² (0.1342) and the sharp appearance of the progression suggests that this state is produced via a resonant interaction with the laser radiation.

A Stern-Volmer quenching study of the $NS(H)$ state indicated a collision free radiative lifetime of 87 ± 14 ns and facile quenching by He, CF_4 , and N_2 , with the latter two gases quenching near gas kinetic rates.¹² Several bands to the blue of the KrF laser spike are not attributable to $NS(H)$ and have been assigned to progressions out of $NS(I^2\Sigma^+)$ and $NS(G^2\Sigma^+)$, although unequivocal assignment of these bands is made difficult by the large number of nested energy states in the 40 000–45 000 cm^{-1} range.¹²

Time profiles of the $NS(B)$ and $NS(H)$ emission were

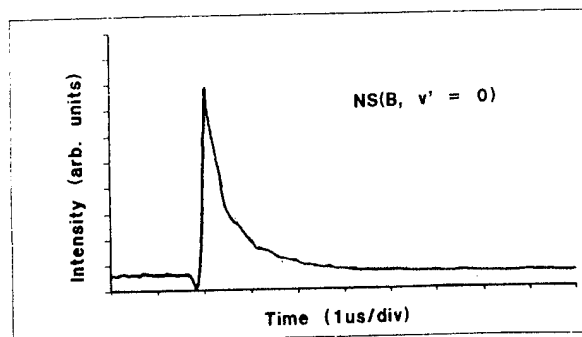


FIG. 3. Temporal profile of the $NS(B \rightarrow X)$ emission.

recorded for various He buffer gas pressures. Figure 3 shows the time profile of the $NS(B \rightarrow X)$ intensity recorded for the 0,4 band near 394.4 nm with no added quencher. The profile reveals a rapid rise of ~ 30 ns followed by a much slower decay over several microseconds. The lifetime of the decay of 1.1 ± 0.2 μs compares favorably with the known radiative lifetime of $NS(B, v'=0)$ of 1.04 ± 0.1 μs ,¹⁰ and we associate the decay with radiative and collisional removal of the excited state. The rise was found to track the excimer laser pulse (FWHM pulse time = 17 ns), and was invariant with added quencher. The time history of the $NS(H \rightarrow X)$ fluorescence was similar, and also indicated a pressure invariant, laser limited rise but with a considerably faster decay rate as noted above, i.e., $\tau_{1/e} = 87$ ns.¹² Both the $NS(H)$ and $NS(B)$ intensities were found to vary as the third power of the laser flux.

From Fig. 2 it is readily apparent that progressions out of higher v' levels of the B state are obscured due to the strong overlap by the H fluorescence. However, since the B radiative lifetime is considerably longer than the H , the H fluorescence was easily discriminated against by setting a photon counter gate delay equivalent to several H lifetimes, e.g., 625 ns. This gate delay also discriminates against any overlapping transitions from other NS states in this region, namely the $NS(G)$ and $NS(I)$ whose lifetimes are estimated to be ≤ 20 ns. The time delayed $B \rightarrow X$ spectrum recorded with the 0.5 m mono/1P28/gated photon counter is shown in Fig. 4. The spectrum, collected for a gate width of 2 μs and for an excimer flux of 70 mJ cm^{-2} , reveals a highly excited nascent vibrational distribution with population in levels up to at least $v'=10$. It is known that $NS(B)$ ceases to fluoresce from vibrational levels above $v'=12$ because of predissociation to $N(^4S) + S(^3P)$.¹⁸ However, population in higher vibrational levels could not be confirmed.

As an aid in measuring the excited vibrational populations and rotational temperatures a spectral simulation code¹⁹ was employed to fit synthetic spectra with the experimentally obtained spectra, and a relevant fit to the $NS(B)$ spectrum is shown in Fig. 4. The vibrational distribution yielding this fit is plotted in Fig. 5 which plots the relative vibrational population against the vibrational term energy. We note that the intensity discrepancies between

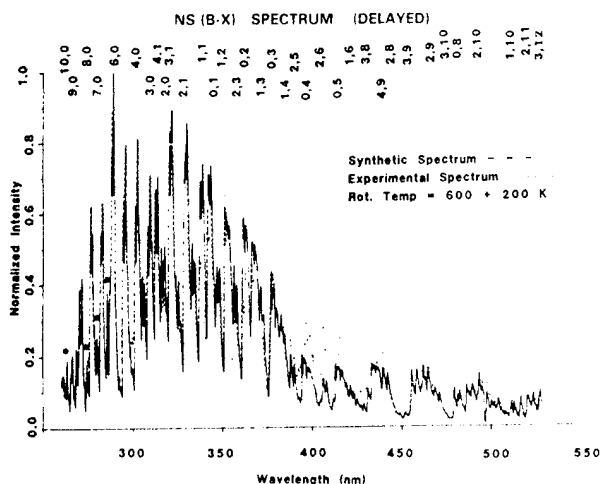


FIG. 4. Time delayed $NS(B \rightarrow X)$ spectrum with a superimposed synthetic spectrum. The peaks marked with an asterisk do not belong to the $NS(B)$ system and are probably due to emission from higher lying states of NS , eg., $NS(H)$, $NS(G)$, and $NS(I)$.

the synthetic and experimental spectrum in the 390–450 nm region, i.e., notably the (0,4), (1,5), (2,6), (0,5), and (0,6) may be due to photon counter pulse pile up. Consequently, larger uncertainties in the relative populations of the $v'=0, 1$, and 2 levels are indicated in Fig. 5. From Fig. 5 it is evident that the photolysis produces a non-Boltzmann vibrational distribution with large relative populations in high $NS(B)$ v' levels. In contrast to the vibrational excitation, a fairly cool rotational temperature of 600 ± 200 K was calculated. Hence, under these photolysis conditions the nascent $NS(B)$ is generated vibrationally hot yet rotationally cool. Further, an analysis of the rotational temperature for the H state¹² revealed a similarly cool rotational temperature of 330 ± 100 K.

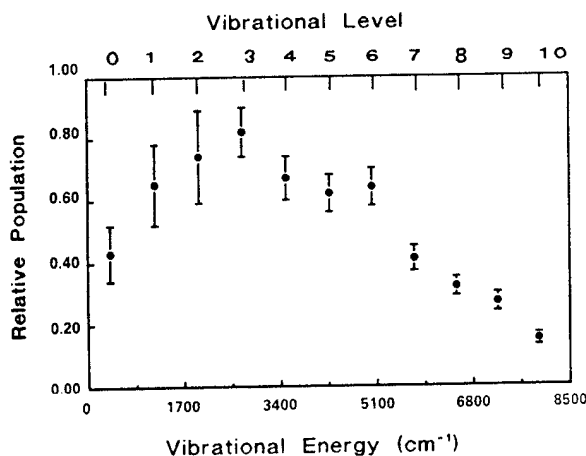


FIG. 5. Nascent $NS(B^2\Pi)$ vibrational population distribution produced from the 248 nm photolysis of S_4N_4 . The total pressure in the cell was 0.8 Torr.

Other photolysis products such as sulfur or metastable states of nitrogen were not detected. For example, no prompt emission from N_2^* or S_2^* was detected. Production of the first excited state of nitrogen, $N_2(A^3\Sigma^+)$, was tested for by adding a small amount of NO to the photolysis chamber. The presence of $N_2(A)$ would typically be signaled by strong NO γ band emission due to the rapid energy transfer reaction: $N_2(A) + NO(X) \rightarrow N_2(X) + NO(A)$.²⁰ No γ band emission was detected. From NO(A) detection limits determined in previous flow tube experiments²¹ we estimate the $N_2(A)$ density to be $\leq 1 \times 10^6$ mol cm^{-3} . The production of $S_2(X)$ was investigated, as described below, by LIF excitation scans on the $S_2(X^3\Sigma_g^- \rightarrow B^3\Sigma_u^-)$ system.

B. Photolysis at 222 nm

Photolysis of S_4N_4 at 222 nm probes vibronic structure, lying on the wing, to the blue of the primary absorption centered near 250 nm. The absorption cross section at 222 nm is equal to 8.14×10^{-18} cm^2 , and while considerably reduced from the 248 nm value is, nonetheless, substantial and provides a further probe of the photodissociation dynamics of the molecule.

Photolysis of 10–20 mTorr of the tetramer at the KrCl wavelength again produced a visible blue fluorescence, albeit much weaker in intensity than that observed in the 248 nm case. Wavelength dispersion of the emission produced a spectrum, similar to that shown in Fig. 3, with two distinct band systems. $NS(B \rightarrow X)$ emission was again observed in the 270–550 nm region with fluorescence originating from v' levels as high as eight. However, the $NS(B)$ emission intensity generated via 222 nm photolysis was < 0.1 of the $NS(B)$ intensity observed during the 248 nm photolysis, for similar conditions of fluence. More strikingly, $NS(H)$ emission was no longer observed in the short wavelength region being replaced with the double banded spectrum shown in Fig. 6(a).

This spectrum is attributable to the $NS(C^2\Sigma^+ \rightarrow X^2\Pi_{1/2,3/2})$ transition and shows only a single progression originating out of $v'=2$. Each band in the spectrum shows two components separated by 221.5 cm^{-1} equivalent to the spin orbit energy splitting of the NS ground state.²² The short and long wavelength components are due to the $1/2$ and $3/2$ transitions, respectively.

Temporal histories recorded for the (2,4) and (2,5) transitions with no added diluent gas showed very spiked Gaussian intensity profiles with a FWHM of 17 ns. The profiles were unaffected by addition of Ar up to 9 Torr. From these time histories the $NS(C^2\Sigma^+, v'=2)$ fluorescent lifetime is estimated to be ≤ 10 ns. This is consistent with a 6.5 ns radiative lifetime determined by Silvers and Chiu for the $NS(C)$ $v'=0$ level via a Hanle effect measurement.²³ In a more detailed study of the $NS(C)$ state Chiu and Silvers²⁴ observed absorption, emission, and fluorescence from the $v'=0, 1$, and 2 levels. They noted a weakening of the bands originating from $v'=1$ and 2 relative to that from the $v'=0$ level. They ascribed this diminution in intensity to a weak predissociation in the $v'=1$ and 2 levels,

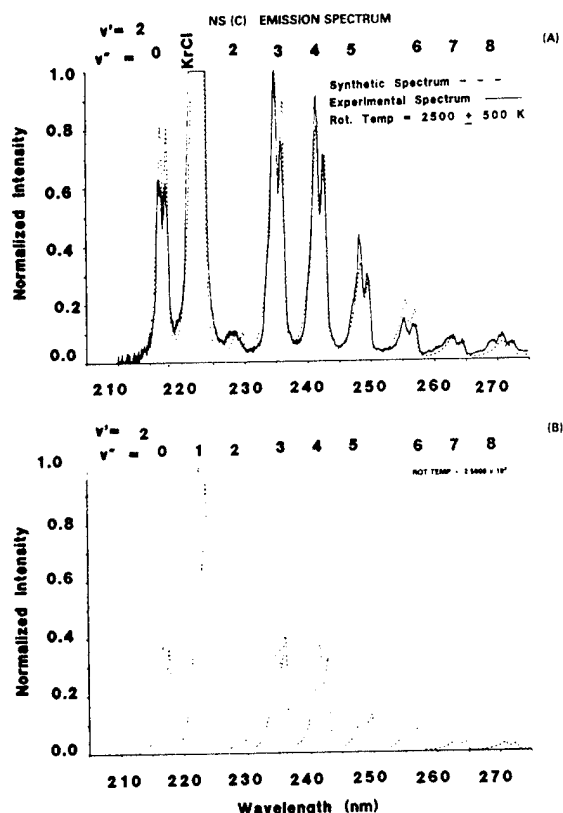


FIG. 6. (a) Emission spectrum collected in the 200–300 nm region for photolysis at 222 nm. The broad band near 222 nm is the KrCl laser spike. (b) Synthetic spectrum of the NS(C²Σ⁺ v'=2) progression showing the relative magnitude of the (2,1) band.

an idea supported by configuration interaction calculations on the C²Σ⁺ adiabatic potential well.²⁵ Hence, the short radiative lifetime we measure for the v'=2 level may be due to predissociation.

It is of interest to compare the photolytically induced spectrum in Fig. 7(a) with Chiu and Silver's fluorescence spectrum (their Fig. 3) obtained by exciting the NS(X) produced in an active nitrogen discharge with a deuterium lamp. They observe strong emission out of v'=0 and much weaker v'=1 and 2 progressions. Moreover, their (2,v'') band intensities are barely discernable from the baseline noise, and only the (2,1), (2,3), and (2,4) are observable. In marked contrast, the photolytically induced spectrum shows no emission from the v'=0 and 1 levels and intense emission only from v'=2, with this progression extending to at least v''=8. This behavior suggests interaction of the 222 nm excimer radiation with an energetically resonant state of NS. From the C spectrum it is clear that the (2,1)_{1/2} and (2,1)_{3/2} bands at 222.46 and 223.56 nm are resonant with the 222 nm laser pulse (FWHM=1 nm), and that excimer laser pumping of these transitions may give rise to the observed spectrum, provided the photodecomposition creates a nascent ground state population which is vibrationally excited, i.e., NS(X, v''=1) must be populated. As noted above, in the 248 nm case an analo-

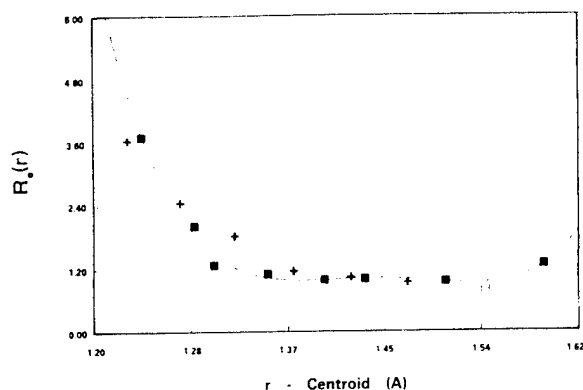


FIG. 7. The apparent dependence of the electronic transition moment on the *r*-centroid for NS(C²Σ⁺, v'=2) as given by a plot of (p_{v',v''}/q_{v',v''})^{1/2} vs *r*. The solid line represents a fourth-order polynomial fit to the data. □—estimated value for the (2,2) band based on p_{2,2} ≈ 1000—Σ p_{v',v''}, + —Jeffries *et al.* data for NS(C²Σ⁺, v'=0); this data was not included in the polynomial fit.

gous LIF process is hypothesized to account for NS(H) fluorescence, i.e., the 248 nm radiation pumps the NS(X, v''=3) → NS(H_{1/2}, v'=0) transition at 248.4 nm, thereby requiring nascent population in NS(X, v''=3). LIF excitation scans on the NS X→B transition, described below, confirm the production of vibrationally excited ground state populated up to at least v''=4 in both the 222 and 248 nm photolysis.

A number of experiments were performed in which the relative intensity of the NS C-X emission was recorded as the incident fluence of the 222 nm pulse was varied. The data indicate a quadratic dependence of the NS(C-X) intensity on excimer fluence.

C. Determination of Franck-Condon factors, *R* centroids, and vibrational transition probabilities for the NS(C²Σ⁺) state

Due to the enhancement of the NS(C, v''=2) emission spectrum relative to others reported to date,²⁴ a more extensive spectral analysis of the emission was undertaken, with calculations of FCF's, *r* centroids, vibrational transition probabilities and transition moments. An RKR computer code was employed in calculating the potential function *U*(*r*) and classical turning points for both NS(C) and NS(X) using existing Dunham coefficients for each state.²² FCF's and *r* centroids were thus obtained for the first three, and only observed, vibrational levels of the C state, and are presented in Table I. These values compare favorably with past values calculated using Morse wave functions.^{8,24}

Vibrational transition probabilities (p_{v',v''}) were calculated from the relation

$$p_{v',v''} \propto A_{v',v''} (\lambda_{v',v''})^3, \quad (1)$$

where *A* is the Einstein coefficient for spontaneous emission and is proportional to the intensity of fluorescence in a given vibrational band at wavelength λ_{v',v''}. Relative

TABLE I. RKR Franck-Condon factors and r centroids for NS($C^2\Sigma^+$).

Transition	$(q^{1/2} + q^{3/2})/2^a$	$(r^{1/2} + r^{3/2})/2$
0,0	612	1.474
0,1	280	1.425
0,2	80	1.379
0,3	18	1.335
0,4	3.8	1.296
0,5	0.64	1.257
0,6	0.11	1.215
1,0	311	1.530
1,1	161	1.485
1,2	301	1.432
1,3	158	1.388
1,4	50	1.342
1,5	14	1.303
1,6	3.2	1.270
1,7	0.65	1.220
2,0	68	1.590
2,1	382	1.539
2,2	18	1.505
2,3	202	1.435
2,4	200	1.400
2,5	88	1.350
2,6	31	1.304
2,7	9	1.287
2,8	2	1.242

^aValues multiplied by 1000.

$A_{v',v''}$ were obtained from area integration of the discrete v',v'' spectral bands taken from the 0.25 m polychromator/diode array response corrected spectrum shown in Fig. 6(a) [excluding the (2,1) band]. Using the known $\lambda_{v',v''}$ ²² Eq. (1) was used to calculate relative $p_{v',v''}$ for the $v'=2$ progression. The results, presented in Table II, are compared with the RKR computed Franck-Condon factors ($q_{v',v''}$), and indicate a gradual increase in $p_{v',v''}$ over $q_{v',v''}$ with increasing v'' . This implies a variation of the electronic transition moment [$R_e(r_{v',v''})$] with internuclear separation. The r centroid relation,²⁶

$$p_{v',v''} = [R_e(r_{v',v''})]^2 q_{v',v''}, \quad (2)$$

TABLE II. Comparison of NS($C^2\Sigma^+$, $v'=2$) vibrational transition probabilities with the RKR Computed Franck-Condon factors.

$v'=2, v''=$	$(q^{1/2} + q^{3/2})/2^a$	$p^{c,p}$
0	68	109
1	382	(254) ^b
2	18	16
3	202	202 ^c
4	200	194
5	88	107
6	31	50
7	9	36
8	2	30

^a p and q values multiplied by 10³.^bThe $p_{2,1}$ value was estimated from: $p_{2,1} \approx 1000 - \sum p_{v',v''}$.^cThe $p_{2,3}$ value is normalized to the $q_{2,3}$ value.

was used to quantify this variation. Figure 7 plots the electronic moment as $(p_{v',v''}/q_{v',v''})^{1/2}$ vs r centroid. According to the RKR calculations, the r centroid varies from 1.24 Å for the (2,8) band to 1.59 Å for the (2,0). Over this interval a smooth decrease in $R_e(r_{v',v''})$ is readily apparent. A similar variation was noted by Jeffries *et al.*⁸ in their LIF spectroscopic study of the NS($C, v'=0$) state, and we have included their data for comparison in Fig. 7. A fourth order polynomial fit to the averaged 1/2 plus 3/2 data yielded the following expression:

$$R_e(r_{v',v''}) = \text{const} [1 - 2.76 r + 2.86 r^2 - 1.31 r^3 + 0.226 r^4] \quad (3)$$

and gives the variation of the transition moment for the region sampled: $1.2 \text{ Å} \leq r_{v',v''} \leq 1.6 \text{ Å}$.

Introducing the functional form for $R_e(r_{v',v''})$ given by Eq. (3), and using the RKR calculated $q_{v',v''}$ (see Table I) in the spectral simulation code a best fit NS(C) spectrum was computed and is graphically overlaid on the experimental spectrum. The simulation correctly predicts the (2,2) vibrational node and fits the higher v'' bands correctly in accord with the increasing $R_e(r_{v',v''})$ in this region. Based on the width of the vibronic bands a rotational temperature of 2500 ± 500 K was determined. Since the (2,1) band should have considerable intensity [i.e., $q_{(2,1)} = 0.382$], and since this band is spectrally obscured by the 222 nm laser light a synthetic spectrum of the entire $v'=2$ progression is presented in Fig. 6(b). This spectrum indicates the relative magnitude of the (2,1) band.

D. NS($X^2\Pi - B^2\Pi$) LIF excitation scans for 248 nm photolysis

The operation of photolytic channels which produce rotationally and vibrationally excited NS(X) was probed by searching for LIF from NS fragments. Excitation spectra were recorded by monitoring NS($B-X$) emission through bandpass filters. Two separate wavelength regions were scanned: 300–310 nm and 360–372 nm using Rh 640 and LDS 750 dyes, respectively. These experiments clearly showed that rotationally and vibrationally excited NS(X) is produced by the 248 nm photolysis as indicated by the LIF spectra shown in Figs. 8 and 13. All of the spectra were corrected for the wavelength dependence of the PDL/filter/PMT combination. As mentioned previously, the minimum excimer pulse to PDL pulse delay time was limited to 2 μ s due to the prompt NS(B) fluorescence. No NS LIF was observable with the PDL probe pulse alone.

As a potential photolytic product, the presence of diatomic sulfur was tested by scanning for LIF on the $S_2(X^3\Sigma_g^- \rightarrow B^3\Sigma_u^-)$ transition. Two wavelength regions were examined: 300–310 nm and 360–370 nm. Since the lifetime of $S_2(B)$ (37 ns) is considerably shorter than NS(B) the NS(B) fluorescence was discriminated against by setting a small gate delay with a gate width equivalent to several $S_2(B)$ lifetimes, i.e., 100 ns. Further, several of these experiments were carried out with high PDL fluences (laser induced pumping rates $\geq 1 \times 10^{10} \text{ s}^{-1}$) in order to saturate the S_2 transitions. Under these experimental con-

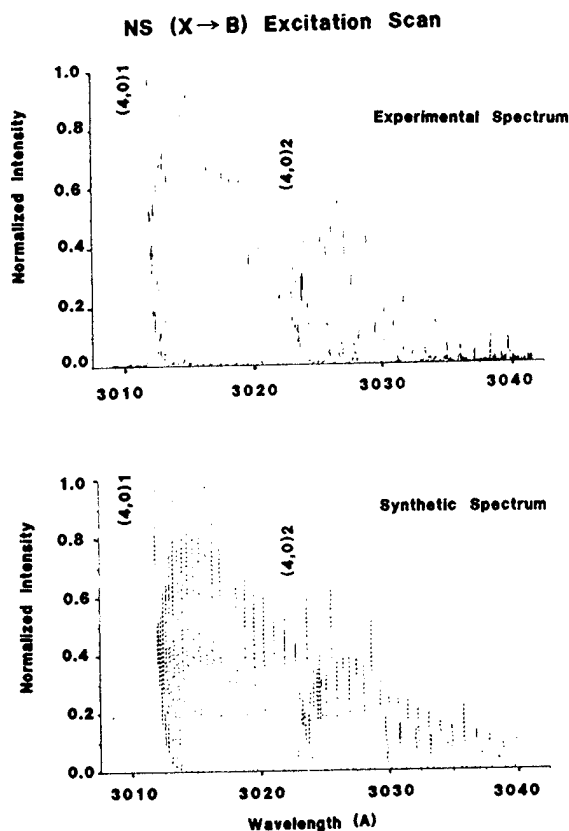


FIG. 8. Experimental (Expt) and simulated (Sim) LIF excitation spectra of the (4,0) transition of the $B^2\Pi_{1/2,3/2}-X^2\Pi_{1/2,3/2}$ system of NS produced via the photolysis of S₄N₄ at 248 nm. 1 and 2 designate the 1/2 and 3/2 spin-orbit components, respectively. The total pressure in the photolysis cell was 0.8 Torr, and the probe dye laser delay time was 70 μ s.

ditions no S₂($B \rightarrow X$) fluorescence was detected. Based on a two level model for near saturated fluorescence in diatomic molecules²⁷ we calculate a S₂($X^3\Sigma_g^-$) detection limit, for our experimental conditions, of 1×10^9 mol cm⁻³.

E. Internal energy distribution of the NS(X) fragments

Since the linewidth of the probe laser (0.01 nm) was not sufficient to fully resolve the individual rotational lines of the NS LIF spectra, the spectral simulation code was modified and was used as an aid in determining vibrational and rotational population distributions. The simulation employed a Gaussian line shape function, a laser line width parameter and the following equation for rotational line intensities:

$$I = kq_{v',v''} \nu_{v',v''} S_{N',N''} P_{v''} Q^{-1} \exp\{-B''N''(N''+1)/kT\}, \quad (4)$$

where k is a proportionality constant, q is a Franck-Condon factor, $\nu_{v',v''}$ is the transition frequency, $S_{N',N''}$ is the Hönl-London factor appropriate to a $\Delta\Lambda=0$ transition, $P_{v''}$ is the population of the v'' vibrational level, Q is

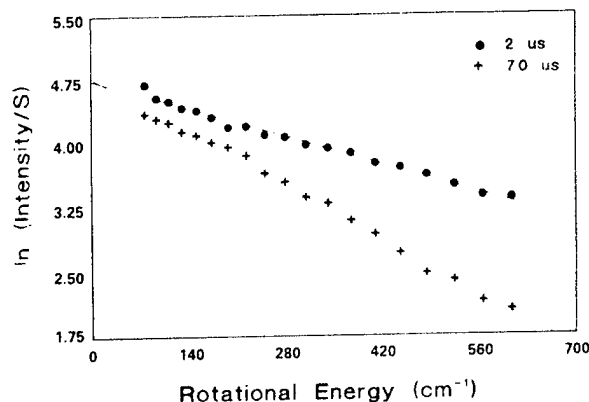


FIG. 9. Quantum state distribution of NS($v''=0$) as measured from (4,0) excitation spectra collected at photolysis to probe pulse delay intervals of 2 and 70 μ s, respectively. The latter spectrum is shown in Fig. 8.

the partition function, B'' is the rotational constant, and T is the rotational temperature. Equation (4) is applicable to a Boltzmann rotational distribution. An excitation scan for the (4,0) band of the $B-X$ system is presented in Fig. 8. The appearance is typical for an unperturbed band of this parallel transition, and should show an R branch head, a red degraded P branch, and no Q branch. However, due to the limited laser resolution the P and R branches remain unresolved. The spectrum collected after a 70 μ s delay appears thermalized ($N''_{\max}=31.5$), and is, indeed, well fit by a spectral simulation utilizing a 340 K rotational temperature. A excitation spectrum recorded for a shorter photolysis to probe pulse delay interval (2 μ s) showed a much flatter and broader rotational distribution with a much less distinct R branch head and population in higher N'' ($N''_{\max}=58.5$), behavior consistent with a more highly excited rotational population in the ground state. A synthetic fit to this spectrum indicated a rotational temperature of 800 ± 200 K. These "best fit" T_R 's are in close agreement with the T_R values calculated directly from the observed (response corrected) spectra. This is indicated in Fig. 9, which plots $\log(I/S_{N',N''})$ vs $-B''N''(N''+1)$ for the (4,0) excitation scans described above. The plots are quite linear, indicative of a Boltzmann distribution in this region. From the slopes of the lines rotational temperatures of 800 and 350 K were determined for the 2 and 70 μ s delay times, respectively.

Rotational relaxation was evident as the pump to probe delay time was increased. This is shown in Fig. 10, which plots the rotational temperature of the (4,0)_{1/2} band vs number of collisions with the helium bath gas for low fluence ($F \leq 10$ mJ cm⁻²) photolysis. Evidently, NS($X, v=0$) is formed with a near nascent rotational temperature of 800 ± 200 K, and a few hundred collisions are required to thermalize the distribution.

The variation in the (4,0)_{1/2} LIF intensity as a function of laser fluence was recorded for conditions of both high and low laser fluence. For these measurements the photolysis to probe pulse delay was set to 20 μ s, sufficient

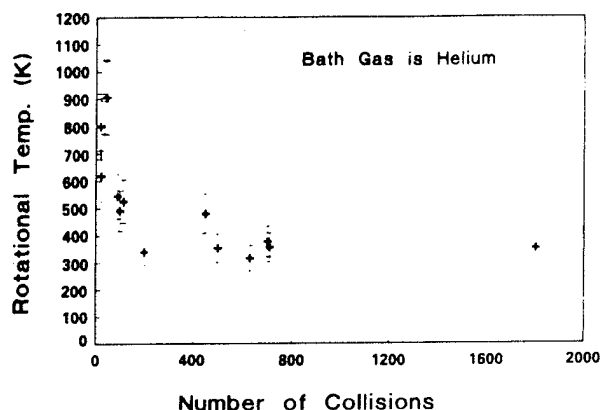


FIG. 10. Collisional cooling of $NS(X, v''=0, N'')$ for low fluence photolysis conditions. +—248 nm photolysis, Δ—222 nm photolysis.

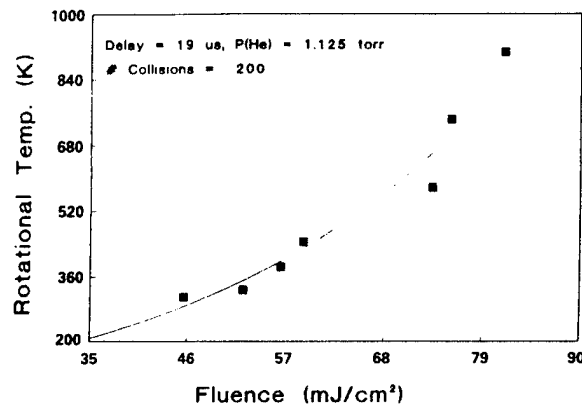


FIG. 12. Variation of the $NS(X, v''=0)$ rotational temperature with KrF laser fluence. The solid line represents an exponential fit, of the form $y = a_0 \exp(a_1 x)$, to the data.

time to allow for the relaxation of the rotational manifold. In the low fluence regime ($0.8\text{--}25\text{ mJ/cm}^2$) the rotational distributions were indeed thermalized. Figure 11 shows a log-log plot of the integrated fluorescent intensity vs excimer laser fluence for the low fluence photolysis. A least squares fit to the data yielded a slope of 2.0 ± 0.2 . This quadratic dependence indicates that 2 KrF photons are required to generate an $NS(X)$ photofragment. For the high fluence measurements the rotational distributions did not appear relaxed, and a substantial variation in the rotational quantum state distribution was evident as the laser flux was varied. This effect is quantified in Fig. 12, which graphs the rotational temperature of the $(4,0)_{1/2}$ band vs laser fluence. It is apparent that under high fluence conditions the rotational distribution is much more excited than would be predicted for a quenched distribution. A nearly exponential decrease in rotational temperature with fluence is seen, and as the fluence is reduced the temperature approaches the thermal limit (near 340 K). This behavior is suggestive of a fluence dependent rotational excitation process in the gas medium.

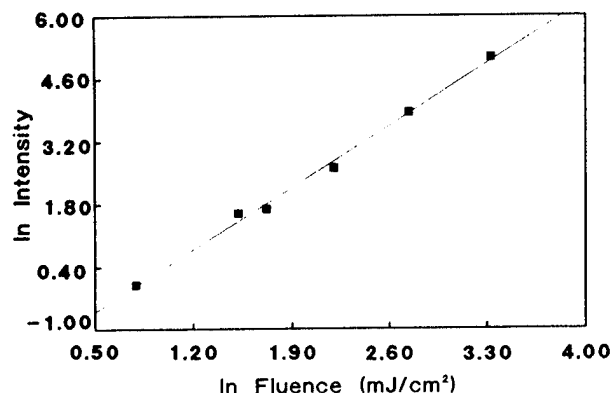


FIG. 11. A plot of the log of the integrated emission intensity of the $NS(4,0)_{1/2}$ band vs log of the KrF laser fluence. The slope of 2.0 ± 0.2 indicates two photons are required to generate the NS ground state.

The variation in the LIF intensity of the $(0,2)_{1/2}$ band was also recorded as a function of laser fluence. In this experiment the delay separating photolysis to probe pulse was set to 70 μs , and the KrF fluence was varied in the range 3 to 17 $mJ\text{ cm}^{-2}$. The results, for this higher vibrational level, also indicated a quadratic dependence of intensity with fluence.

Population in vibrational levels above $v''=0$ was probed by scanning the 360–372 nm region. Figure 13 displays a typical LIF excitation scan of this region, collected for a delay interval of 70 μs and at a total pressure of 1.2 Torr. Under these experimental conditions the rotational distribution is equilibrated (i.e., $T_{rot} = 340\text{ K}$) while the vibrational distribution remains unperturbed. Hence, the spectral simulation designed to determine relative $P_{v'}$ was simplified as only a single rotational temperature in Eq. (4) needed to be specified.

The rate constant for quenching vibrationally excited $NS(X)$ by He has not been reported. However, we note that excitation spectra collected under low collision conditions (~ 30 collisions) and under high collision conditions (~ 1300 collisions) showed no significant differences in the vibrational distribution. This indicates the $NS(X)$ –He VET is not a facile process.

Population in the $v''=2, 3$, and 4 levels is evident in the spectrum of Fig. 13(a). Population in $v''=4$ is indicated by the presence of the weak $(3,4)$ bandhead near 361 nm. The spectral code was used in determining the relative vibrational populations in the 2, 3, and 4 levels and an optimized fit is shown in Fig. 13(b). The fractional vibrational populations obtained in this manner are 0.89, 0.07, and 0.03 for $v''=2, v''=3$, and $v''=4$, respectively. This distribution was found to be independent of laser fluence. The fit was such that changing $P_{v''=4}$ from 0.03 to 0 removed the $(3,4)$ bandhead, in clear disagreement with the experimental data. Population in higher v'' levels was not evident. The region of the $(5,6)_{1/2}$ band in the vicinity of 371.0 nm was scanned. The FCF for this band is equivalent to the $(0,2)$ transition, with strong LIF signals from the latter being observed. However, no LIF signals were de-

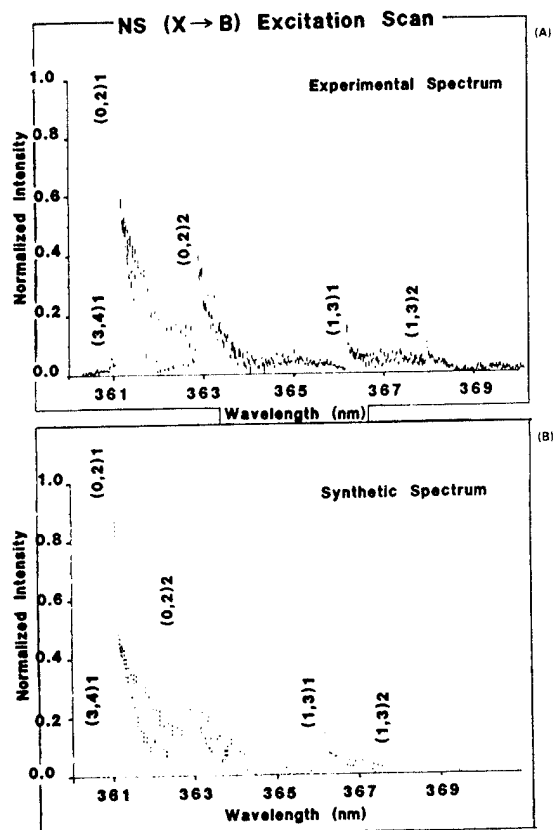


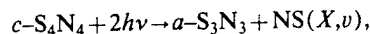
FIG. 13. Experimental (a) and synthetic (b) NS ($X \rightarrow B$) LIF excitation spectra showing population in $v''=2$, $v''=3$, and $v''=4$ vibration levels.

tected in this region even with substantially higher pressures of S_4N_4 in the photolysis cell. From determinations of signal to noise ratios, i.e., $-2S/N$ in the LIF scans we estimate $P_{v''=6} < 0.01$.

IV. DISCUSSION

The photolytic process at 248 nm leading to the formation of NS(B) and NS(H) is complicated by the variety of $(SN)_x$ intermediates which may be formed, and by the energetics of these species. However, in view of the data, presented above, it appears that the NS(B) and NS(H) are formed from different precursor species. For example, the emission spectrum (Fig. 4) indicates the nascent NS(B) is produced vibrationally hot, in a non-Boltzmann distribution with v' levels as high as ten populated. The NS(B) is also formed with some degree of rotational excitation as $T_{rot} = 600 \pm 200$ K. In contrast, the NS(H) appears rotationally cold, and the collected emission is reminiscent of a fluorescence scan with only a single vibrational level ($v'=0$) emitting. Additional considerations, as previously noted, such as the energy overlap of the $H(0,3)$ transition with the KrF frequency, the population detected in ground state vibrational levels, and the disappearance of the H fluorescence when the excimer wavelength is changed clearly indicates the H state is formed by laser excitation of vibrationally excited ground state NS fragments. Since the

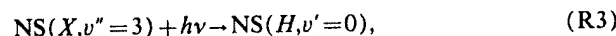
KrF wavelength is above the dissociation limit for NS(B), the B fluorescence cannot arise from an analogous KrF excitation of NS(X) molecules. Rather, some higher order $(SN)_x$ homolog must be the precursor to NS(B). We further note that the temporal history of the B emission indicates that the NS(B) is not generated via a collisional process. Rather, its production appears photolytically induced. The fluence data indicates that NS(B), as well as the more energetic NS(H), is formed in a three photon process. Aside from the prompt NS(B) and NS(H) emissions, the excitation scans reveal that rotationally and vibrationally excited NS(X) is also a product of the photolysis, and is produced in a two photon event. In light of these considerations, the following general mechanism is proposed to qualitatively account for the NS(B), NS(H), and NS(X,v) states produced in the KrF photolysis of S_4N_4 :



$$\Delta H = -132 \text{ kcal mol}^{-1}, \quad (R1)$$



$$\Delta H = -21 \text{ kcal mol}^{-1}, \quad (R2)$$



where reaction (R3) shows the resonant excitation which produces the NS(H) state, and where c and a represent the cyclic and acyclic isomers, respectively. The heats of reaction have been calculated from $\Delta H_f(S_xN_x)$ values previously determined via a MOPAC calculation.²⁸

Reaction (R1) depicts a multiphoton excitation of cyclic S_4N_4 to an excited singlet state which subsequently dissociates yielding vibrationally excited NS(X) fragments and an acyclic S_3N_3 fragment. The large value of the exothermicity for this process is not surprising, considering the 2 uv photon excitation contributes $230 \text{ kcal mol}^{-1}$ at the 248 nm wavelength. The heat of reaction is sufficient to provide for the vibrational excitation of the NS(X) fragment ($v''=4$ requires 13.5 kcal), and for a large remnant energy balance of over $100 \text{ kcal mol}^{-1}$. For comparison, a one photon excitation would be much less exothermic ($-17 \text{ kcal mol}^{-1}$) and would be nearly thermal neutral when the vibrational energy in the NS fragment is accounted for. That two photons are required to reach the dissociative state is also supported by the results of MO calculations on $c-S_4N_4$, as described below.

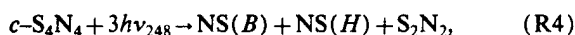
If the partitioning of excess energy between the NS(X) and S_3N_3 photofragments in reaction one is statistical in nature, the more massive S_3N_3 fragment, with 12 vibrational modes, would consume the majority of the vibronic energy. Further, provided the excited S_4N_4 electronic state, from which dissociation occurs, has approximately the same S-N geometry as the S_4N_4 ground state, the energy available to the NS fragment would not be expected to exceed that available from simple geometric relaxation of the NS bond length in $c-S_4N_4$. The energy available in contracting the N-S bond length in $c-S_4N_4$ (1.63 \AA)¹³ to its equilibrium value in monomeric NS (1.495 \AA)²² is

readily obtained from the RKR potential well of the NS ground state. We calculate that $8.6 \text{ kcal mol}^{-1}$ of vibrational energy can be imparted to the released NS(X) fragment. This represents enough energy to populate NS(X) up to $v''=3$. This result agrees reasonably well with the experimental measurements which showed small relative populations of 0.07 and 0.03 in the $v''=3$ and $v''=4$ levels, respectively, and no measurable population in higher levels. Thus, it appears that the excited state is sufficiently long lived (on the order of a few vibrational periods) to allow for, at least, partial vibrational energy randomization in the transitional S_4N_4 structure.

Evidently, from the rotational excitation observed in the NS(X , $v=0$) fragment, a relatively small fraction of the excess energy available in the primary photodissociation ends up in NS rotation. Rotational energies much higher than 1000 cm^{-1} (2.9 kcal) were not detected. Intuitively, the presence of some rotational excitation in the NS photofragments indicates that the dissociation is not linear, and that there is some excitation of the bending modes in the transition.

The photofragments produced in reaction one may undergo secondary photolytic processes, as indicated by reactions (R2) and (R3). Reaction (R2) shows the NS(B) being formed from the single photon excitation/dissociation of an $\alpha\text{-S}_3\text{N}_3$ intermediate. The observation of NS(B , $v_{\text{max}}=10$) places an energy constraint on reaction (R2), and we are required to choose the cyclic form of S_2N_2 over the acyclic form, since the latter would lead to $\alpha+23 \text{ kcal mol}^{-1}$ endothermic process. The reaction exothermicity thus calculated ($-21 \text{ kcal mol}^{-1}$) is, considering the error of the MOPAC²⁸ calculation, just sufficient to populate NS up to its observed vibrational maximum. Thus, it would appear that the reaction exothermicity is completely consumed in NS(B) vibration. Since it is reasonable to assume that some energy is partitioned to NS(B) translation and S_2N_2 vibration-translation, the ΔH for reaction (R2) is likely to be $< -21 \text{ kcal mol}$. This would require a larger energy content, than determined by the MOPAC calculation, for the $\alpha\text{-S}_3\text{N}_3$ precursor. As explained above, the $\alpha\text{-S}_3\text{N}_3$ molecules are likely to be formed with considerable internal excitation.

Other S_4N_4 photodecomposition mechanisms may certainly be written. However, the majority of these can be ruled out based on considerations of energetics and the experimental data. For example, a mechanism involving the nonlinear absorption of three photons by the tetramer to produce NS(B) and NS(H),



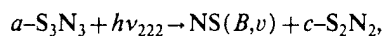
is endothermic by 37 kcal mol^{-1} , and does not account for the specific NS(H , $v'=0$) fluorescence or the two photons required to produce the ground state.

The data for the KrCl photolysis is qualitatively similar to that obtained in the KrF photolysis. For example, the 222 nm emission spectrum indicates formation of vibrationally hot NS(B), the LIF scans show that rotationally and vibrationally excited ground state NS photofragments are produced, and the NS(C) emission indicates a

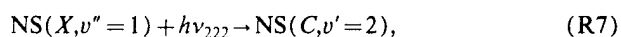
resonant excitation by the laser on an NS($X-C$) transition. Further, the time histories of the emissions suggest the NS(B) and NS(C) formation rates are photolytically driven and are independent of collisional processes. Given these similarities an analogous mechanism is proposed for the photodissociation at 222 nm:



$$\Delta H = -32 \text{ kcal mol}^{-1}, \quad (R5)$$

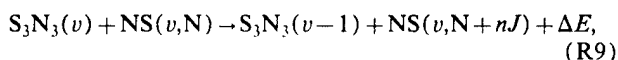
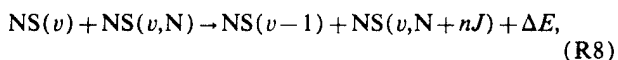


$$\Delta H = -35 \text{ kcal mol}^{-1}, \quad (R6)$$



where the linear dissociation of the tetramer [reaction (R5)] is supported by the quadratic dependence of the NS(C) fluorescence intensity on KrCl excimer fluence. The energy release for reactions (R5) and (R6) is high enough to account for the observed NS(X) and NS(B) vibrational excitation, i.e., NS(X , $v=4$) requires $13.5 \text{ kcal mol}^{-1}$ and NS(B , $v=8$) requires $17.5 \text{ kcal mol}^{-1}$. The observation of NS(B , $v_{\text{max}}=8$) again restricts the choice of the S_2N_2 photofragment to the cyclic form.

The strong variation in T_{rot} with KrF fluence that is depicted in Fig. 12 suggests the operation of a fluence dependent, rotational excitation process in the photolysis zone. A second order process involving an efficient $V \rightarrow R$ energy transfer could account for the observed behavior. Due to the large absorption cross section of S_4N_4 at 248 nm large densities of NS(X , v'') and $S_3N_3(v)$ may be produced from the primary photolysis step [reaction (R1)]. These species could react further in energy transfer processes



where nJ indicates n additional rotational quanta. The densities of vibrationally excited photofragments will depend on laser fluence. For high fluence photolysis ($F \geq 75 \text{ mJ cm}^{-2}$) the calculated dissociation is near unity.²⁹ If we assume the $V \rightarrow R$ transfer has a $\sim 20 \mu\text{s}$ lifetime, i.e., the rotational excitation process was observed at a $20 \mu\text{s}$ delay, and that the high fluence photolysis of 10 mTorr S_4N_4 produces $\sim 1 \times 10^{15} \text{ mol cm}^{-3}$ of NS(v) + $N_xS_x(v)$ photofragments then the calculated second order rate constant $k_{v-r} \approx 10^{-11} \text{ cm}^3 \text{ s}^{-1}$. This $V \rightarrow R$ rate coefficient is not untypical of those reported by Moore for a large class of polyatomics.³⁰

Molecular orbital calculations, both semiempirical³¹ and *ab initio*,³² indicate the S_4N_4 ground state to be a singlet, and specify the intense 250 nm absorption band as the molecules highest occupied molecular orbital-lowest unoccupied molecular orbital (HOMO-LUMO) transition; giving it a $B_2 \rightarrow E$ designation. The LUMO is a degenerate Π orbital and is antibonding, with respect to the S-S linkage. The *ab initio* calculations indicate that the $B_2 \rightarrow E$ energy separation is $224 \text{ kcal mol}^{-1}$, and that there are four,

nearly resonant, energy states (designated by *) situated 230 kcal above the E level (LUMO). Since these calculations have not incorporated electron correlation, the energy separations are clearly too large ($\sim 2x$); this may be seen by comparing the measured $B_2-E \Delta E$ of 120 kcal mol $^{-1}$ (obtained from the 250 nm spectral feature shown in Fig. 1) with the calculated $B_2-E \Delta E$ value of 224 kcal mol $^{-1}$. Applying a correction factor of $\times 0.5$ to the calculated values yields a B_2 to * state ΔE of 227 kcal mol $^{-1}$, which is in good agreement with the fluence and thermochemical data indicating that two 248 nm photons (230 kcal) are required to reach the dissociative state. The calculations suggest that a two photon absorption by S_4N_4 is a resonant process (sequential excitation) in which the first photon promotes an electron to the E antibonding Π orbital (perhaps with rupture of the weak S linkage), and the absorption of a second photon promotes the electron from the E state to one of the four upper * states. It is likely that the * states are repulsive or very weakly bound, and rapidly dissociate to yield a nonlinear $a-S_4N_4$ intermediate. The temporal histories of the emissions indicate that the lifetimes of these states is $\tau \leq 30$ ns.

V. SUMMARY AND CONCLUSIONS

Emission from several electronically excited states of NS is observed when the energetic molecule S_4N_4 is photolyzed with radiation from an excimer laser. Photolysis at 248 nm generates fluorescence from the $B(^2\Pi_{1/2,3/2})$, $H(^2\Pi_{1/2})$, $G(^2\Sigma^-)$, and $I(^2\Sigma^+)$ states of NS. NS($B(^2\Pi_{1/2,3/2})$) and NS($C(^2\Sigma^+)$) fluorescence is observed when the photolysis wavelength is changed to 222 nm. The NS(H) and NS(C) spectra are postulated to arise from a resonant interaction between the KrF and KrCl excimer photons, respectively, and vibrationally hot ground state NS. LIF excitation scans confirm the production of rotationally and vibrationally excited NS(X) up to $v=4$. An analogous mechanism is thought to generate some of the $v'=2$ bands of NS(I, G).¹²

The experimental data, thermochemistry, and *ab initio* calculations on the tetramer support a nonlinear (two photon) dissociation step for parent S_4N_4 at the 248 nm wavelength. It is postulated that the dissociation produces vibrationally excited NS and an acyclic S_3N_3 photofragment. The observation of the maximum vibration in NS(X), i.e., $v'=4$ is consistent with statistical energy partitioning in the photofragments and suggests the $a-S_3N_3$ segment is formed with considerable internal excitation. The data indicates the $a-S_3N_3$ fragment may undergo further photodissociation leading to the production of vibrationally hot NS(B) and an S_2N_2 molecule, and that these dissociations occur on a time scale much shorter than the laser pulse. Surprisingly, no evidence for the formation of sulfur or nitrogen was obtained. This may be contrasted with the explosive or thermal decomposition mechanisms which are known to generate both nitrogen and sulfur.^{33,34}

The short radiative lifetime measured for the NS(C , $v'=2$) state ($\tau < 10$ ns) may be indicative of some predissociation in this vibration. The NS(C) intensity distribution and the calculated FCF's are used to evaluate the C

states electronic transition moment variation with internuclear separation; a small dependence was found with R_e increasing with decreasing r .

The photolysis of S_4N_4 at excimer wavelengths may be used as an alternate method for producing the NS radical for kinetic and spectroscopic study. In comparison to the standard method for NS production (reaction of active nitrogen plus sulfur compound) the photolysis is largely free from interferences, i.e., S_2 , N_2 , and creates a relatively high distribution of vibrationally excited ground state. The latter effectively red shifts the absorption spectrum of NS such that NS electronic states with energies in excess of 43 000 cm $^{-1}$ are more readily accessed via optical excitation.

ACKNOWLEDGMENTS

The authors express their appreciation to Dr. Gilbert Mains for his work on the *ab initio* M. O. calculations on S_4N_4 . We also express our thanks to Dr. Robert Coombe, which two of the authors (A.P.O. and T.L.H.) know as scientific mentor and friend, for helpful discussions relating to this work, as well as past works.

- ¹ J. B. Jeffries and D. R. Crosley, *Combust. Flame* **64**, 55 (1986).
- ² C. A. Gottlieb, J. A. Ball, E. W. Gottlieb, C. J. Lada, and H. Penfield, *Astrophys. J.* **200**, L147 (1975).
- ³ T. B. H. Kuiper, B. Zuckerman, R. K. Kakar, and E. N. R. Kuiper, *Astrophys. J.* **200**, L151 (1975).
- ⁴ T. L. Henshaw and A. P. Ongstad, *Investigation of NS($B^2\Pi$) as the Optically Active Medium for a Short Wavelength Chemical Laser* (1989), unpublished report.
- ⁵ D. G. Sutton and S. N. Suchard, *Appl. Opt.* **14**, 1898 (1975).
- ⁶ K. Raghuveer and N. A. Narasimham, *J. Astrophys. Astron.* **3**, 13 (1982).
- ⁷ H. Obase, I. Nagano, M. Tsuji, and M. Nishimura, *J. Phys. Chem.* **89**, 257 (1988).
- ⁸ J. B. Jeffries, D. R. Crosley, and G. P. Smith, *J. Phys. Chem.* **93**, 1082 (1989).
- ⁹ A. Jenouvier and B. Pascat, *Can. J. Phys.* **58**, 1275 (1980).
- ¹⁰ J. B. Jeffries and D. R. Crosley, *J. Chem. Phys.* **86**, 6839 (1987).
- ¹¹ I. J. Wysong, J. B. Jeffries, and D. R. Crosley, *J. Chem. Phys.* **91**, 5343 (1989).
- ¹² T. H. Henshaw, A. P. Ongstad, and R. I. Lawconnell, *J. Chem. Phys.* **96**, 53 (1992).
- ¹³ Tetrasulfur tetranitride (S_4N_4) is in the form of an eight-membered ring of alternating N and S atoms. The N-S bond distances are all equivalent at 1.63 Å, which lies between the value for a NS single bond (1.74 Å) and that for an NS double bond (1.54 Å). In a similar manner, the distance between the two trans sulfur atoms (2.58 Å) is substantially shorter than the sum of the van der Waals radii (3.7 Å) and somewhat longer than a S-S single bond (2.08 Å). This implies weak S-S bonding an idea supported by molecular orbital calculations (Ref. 31). It is believed that it is this weak bonding between the sulfur atoms that causes the molecule to pucker into its characteristic tub or boat configuration. The NS bond order of 1.5 is most plausibly explained by a π electron system, which is due to $p_z(\text{nitrogen})-d_{\pi}(\text{sulfur})$ overlapping. See H. G. Heal, in *Inorganic Sulfur Chemistry*, edited by G. Nickless (Elsevier, Amsterdam, 1968); O. Glemser, *Angew. Chem. Intern. Edit.* **2**, 530 (1963).
- ¹⁴ C. K. Barker, A. W. Cordes, and J. L. Margrave, *J. Phys. Chem.* **69**, 334 (1965).
- ¹⁵ M. Villena-Blanco and W. L. Jolly, *Inorg. Synth.* **9**, 98 (1967).
- ¹⁶ J. Mason, *J. Chem. Soc. A*, 1567 (1969).
- ¹⁷ P. S. Braterman, *J. Chem. Soc.* 2297 (1965).
- ¹⁸ Y. Matsumi, T. Munakata, and T. Kasuya, *J. Phys. Chem.* **88**, 264 (1984).

- ¹⁹R. I. Lawconnell, *NS(B) Spectrum Theory and Code*, FJSRL TR-89-0005, USAFA, CO 80840, 1989.
- ²⁰W. G. Clark and D. W. Setser, *J. Phys. Chem.* **84**, 2225 (1980).
- ²¹A. P. Ongstad, T. L. Henshaw, R. I. Lawconnell, and W. G. Thorpe, *J. Phys. Chem.* **94**, 6724 (1989).
- ²²K. P. Huber and G. Herzberg, *Constants of Diatomic Molecules* (Van Nostrand, New York, 1979).
- ²³S. J. Silvers and C. Chiu, *J. Chem. Phys.* **61**, 1475 (1974).
- ²⁴C. Chiu and S. J. Silvers, *J. Chem. Phys.* **63**, 1095 (1975).
- ²⁵G. C. Lie, S. D. Peyerimhoff, and R. J. Buenker, *J. Chem. Phys.* **82**, 2672 (1985).
- ²⁶P. A. Fraser, *Can. J. Phys.* **32**, 315 (1954).
- ²⁷Assuming a two level system, in steady state, and near saturation [see A. P. Baronavski and J. R. McDonald, *Appl. Opt.* **16**, 1897 (1977)] and R. P. Lucht in *Laser Spectroscopy and its Applications*, edited by L. J. Radziemski, R. W. Solarz, and J. A. Paisner (Marcel Dekker, New York, 1987), the detection limit may be calculated from $N_1^0 = \{4\pi\eta_p/(A Vc \epsilon \Omega \Delta t)\} \times \{[Q + A + (B_{12} + B_{21})I_v]/B_{12}\} I_v$, where N_1^0 is the lower state number density of the unperturbed system, η_p is the number of photons (incident on the photocathode) required to generate 1 photoelectron, A and B are Einstein coefficients for levels 1 and 2, Vc is the fluorescence probe volume, ϵ is the efficiency of the optical collection system, Ω is the solid angle subtended by the collection optics, Δt is the laser pulse time, Q is the total upper level quenching rate, and I is the laser intensity. The calculation was done for the (6,0), $R(20)$ line for saturable pumping, i.e., $(B_{12} + B_{21})I_v \gg Q + A$, and used the following values: $\eta_p = 6.5$ (15% quantum efficiency), $A = 2.7 \times 10^7 \text{ s}^{-1}$, $Vc = 0.016 \text{ cm}^3$, $\Delta t = 1 \times 10^{-8} \text{ s}$, $\epsilon = 0.1$, and $\Omega = 0.012 \text{ sr}$.
- ²⁸MOPAC (see J. J. P. Stewart, MOPAC Manual (6th ed.), *A General Molecular Orbital Package*, FJSRL TR-88-0007, USAFA, CO 80840, 1988) was employed, using a MNDO-PM3 Hamiltonian with a restricted Hartree-Fock calculation, to obtain the heats of formation of the various S_xN_x intermediates. The heats of formation, as given in Ref. 12, at 298 K are ΔH_f (kcal mol⁻¹) = 81.2, 117, 54, 112.3, 54.8, and 98 for $c\text{-S}_4\text{N}_4$, $a\text{-S}_4\text{N}_4$, $c\text{-S}_3\text{N}_3$, $a\text{-S}_3\text{N}_3$, $c\text{-S}_2\text{N}_2$, and $a\text{-S}_2\text{N}_2$, respectively.
- ²⁹R. Bellman, G. Birnbaum, and W. G. Wagner, *J. Appl. Phys.* **34**, 780 (1963).
- ³⁰C. B. Moore, *J. Chem. Phys.* **43**, 2979 (1965).
- ³¹A. G. Turner and F. S. Mortimer, *Inorg. Chem.* **5**, 906 (1966).
- ³²We are grateful to Professor Gilbert Mains for carrying out the all electron *ab initio* calculations at the HF/6-31G* level at NCSA under Grant No. CHE890003N.
- ³³M. Goehring, *Ergebnisse und Probleme der Chemie der Schwefelstickstoff Verbindungen* (Akademie-Verlag, Berlin, 1957).
- ³⁴R. D. Smith, *Chem. Phys. Lett.* **55**, 590 (1978).

Second-harmonic generation in planar waveguides of doped silica

**John J. Kester and Paul J. Wolf
W. Roc White**

a reprint from Optics Letters

Second-harmonic generation in planar waveguides of doped silica

John J. Kester and Paul J. Wolf

Frank J. Seiler Research Laboratory, U.S. Air Force Academy, Colorado Springs, Colorado 80840-6528

W. Roc White

Department of Physics, U.S. Air Force Academy, Colorado Springs, Colorado 80840-5000

Received September 15, 1992

Second-harmonic generation was produced in germanium-doped silica planar waveguides prepared by simultaneous illumination with 1064- and 532-nm laser light. During preparation using prism coupling to specific waveguiding modes, the film-generated second-harmonic intensity grew as a function of preparation time until it saturated. The growth rate and saturation level for *p*-polarized second-harmonic intensity was an order of magnitude greater than that observed for the *s* polarization. The efficiency for a 2-cm waveguide length was at least 0.5%. The comparison of experimental results indicates a mechanism for this planar geometry that is similar to that producing harmonic effects in optical fibers.

The efficient production of frequency-doubled light in optical fibers has been observed through optical processing with the fundamental frequency ω (Ref. 1) or additionally seeded with frequency-doubled light 2ω .² The process is attributed to the formation of a spatially varying dc field within the fiber, resulting in quasi-phase-matching between ω and the fiber-generated 2ω .³ Whereas the process for localized modification of optical properties is not fully understood, it has been linked with the atomic and molecular structure associated with dopants and defects within the fiber.⁴⁻⁶ These effects have been characterized by nonlinear time-dependent growth^{1,7} followed by saturation at efficiencies greater than 5%.⁸ Because of their one-dimensional nature, no input polarization dependence has been reported for second-harmonic generation (SHG) from fibers⁸ or ridge waveguides.⁹

This Letter describes the observation of second-harmonic light generated in two-dimensional waveguiding films that have a composition similar to the optical fibers. We present measurements of second-harmonic growth, saturation, and erasure in specific waveguiding modes of optically processed films. In addition, the dependence of these phenomena on the polarization of the input coupled light is detailed.

The waveguides were produced by ion-beam sputtering of high-purity silica and germanium onto commercial optical-grade fused-silica substrates. The sputter deposition was carried out by an argon-ion beam at a rate of 0.11 nm/s in a partial pressure of 1×10^{-4} Torr of oxygen. The two films used in this study were approximately 2 and 4 μm thick and had an average surface roughness of 1.5 nm. Auger analysis indicated that the germanium content was approximately 6 at. % and was substantially oxidized.

The experimental geometry is shown in Fig. 1. The film was illuminated with 1064-nm (ω) and/or

532-nm (2ω) radiation which was Q switched at 1.22 kHz and mode locked with an average power of as much as 500 mW. This maximum average power produced laser pulses with a peak power of 150 kW. A half-wave plate controlled the polarization of both the ω and 2ω light with a polarization ratio of greater than 98% for both frequencies and polarizations. The laser light was focused with a 23-cm focal-length lens and prism coupled into the film. Scattering from waveguided light at the film-air interface was collected by a fiber-optic waveguide and detected by a Hamamatsu 1P28 photomultiplier tube (PMT). The waveguided light emitted from the film edge was focused by a 10 \times microscope objective and filtered for detection of only 532-nm light by the PMT. Typically 300–1000 laser pulses were detected by the PMT, averaged by a boxcar, and collected by a computer. Larger SHG signals were detected by a photodiode that was sensitive to ω and 2ω . During measurement of film-generated second-

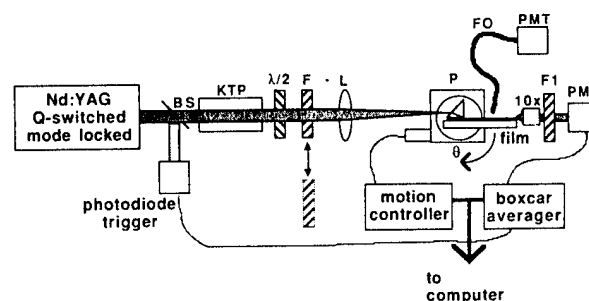


Fig. 1. Experimental setup for thin-film waveguiding experiments. Laser light is coupled into different waveguiding modes by rotation of the film and prism assembly P. To optically prepare the film, filter F is removed to allow illumination of film by ω and 2ω light. To measure film-generated second-harmonic light, F blocks 2ω light. Filter F1 passes only second-harmonic light to the PMT. BS, beam splitter; L, lens; FO, fiber-optic waveguide.

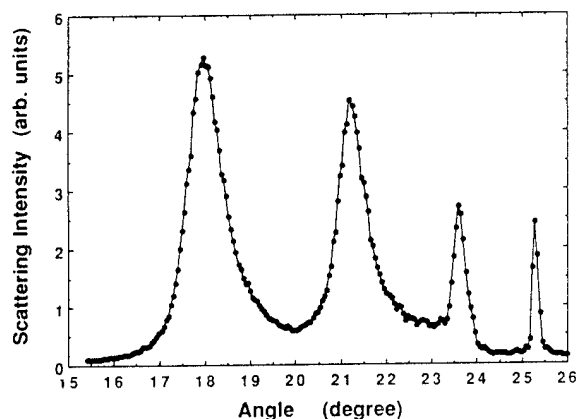


Fig. 2. Scattering intensity from thin-film waveguiding modes versus the laser light external angle to the coupling prism. The input beam was s polarized with a 532-nm wavelength.

harmonic intensities, an IR-transmitting filter was placed before the sample assembly to block the 532-nm seed light.

Waveguiding was initiated by coupling ω and/or 2ω light into the film at the right-angle corner of the prism-film interface. The angles for maximum coupling efficiency were determined by detecting the intensity of scattered light from waveguiding modes as a function of the external coupling angle (Fig. 2). The angular coupling ranges for the lowest-order ω and 2ω modes were 0.64° and 0.35° , respectively. The index of refraction for p-polarized ω and 2ω illumination was calculated¹⁰ to be 1.5234 and 1.5401, respectively, by using the coupling angle for peak scattering intensities. Small anisotropies (0.002) were calculated for s-polarized indices that were slightly greater than the experimental error (0.001). These index values agree with the dispersion measurements obtained by using visible and near-IR transmission measurements.¹¹ The waveguide scattering intensity as a function of distance along the waveguiding path indicated that losses in the waveguide were approximately 5 dB/cm.

Initial experiments attempted to produce harmonic generation from films prepared with only 1064-nm illumination. After preparation times exceeding 8 h, no second-harmonic signal was observed. In our film experiments, incident peak laser powers of as much as 100 kW were incident upon the coupling prism, but because of the absence of an air gap in this geometry the maximum light coupled into the waveguide was of the order of 1 kW. The majority of the incident beam was reflected at the prism-film interface. It would appear that the required threshold of approximately 5-kW peak power to initiate efficient second-harmonic intensities with only the fundamental wavelength⁸ was never reached.

When 1064- and 532-nm light was simultaneously coupled into waveguiding modes of a germania-doped silica film, film-generated second-harmonic (FGSH) light grew as a function of time after initiating illumination, as shown in Fig. 3. The second-harmonic signal was detected by briefly blocking the 532-nm seed beam during the growth process and measuring the

FGSH signal with only IR illumination. The data indicate an initial quadratic dependence of the second-harmonic intensity for approximately 20 min before becoming nearly linear for as much as 4 h when the second-harmonic intensity saturates. Multiple paths within the film were prepared, and, in general, saturation occurred between 2 and 10 h. The time to reach saturation and the maximum FGSH intensity level is highly dependent on the intensity $I(\omega)$ and the ratio of intensities $I(2\omega)/I(\omega)$ coupled into the film. The long preparation times before saturation in our thin films relative to fiber preparation times were attributed to the low preparation power levels within the film, which are due to low coupling efficiency of the laser light.

After saturation, the FGSH effect was stable at room temperature. Prepared films retained approximately the same FGSH efficiency over a period of 10 days. One growth study was stopped and restarted 15 h later, with the same efficiency and growth rate as before the interruption.

To ensure that the second harmonic was generated in the film, an output prism coupler was added to intercept both the ω and 2ω light in an unprepared waveguiding path. After the output-coupled 2ω light reached saturation, the prism was removed, and the second-harmonic light was then observed from the edge of the film, as shown in Fig. 1. The second-harmonic light again grew as a function of time and saturated. Because the only change was the addition of a longer, unprepared waveguiding path, we conclude that the additional second-harmonic light was generated within the newly illuminated waveguide path.

At the saturation point, the efficiency of SHG was determined by comparing the collected output power of FGSH with the fundamental light intensity. After compensating for detector sensitivity, the output at the fundamental frequency was 190 μ W and the output at the second harmonic was approximately 1 μ W, which gave an efficiency of approximately 0.5%. The

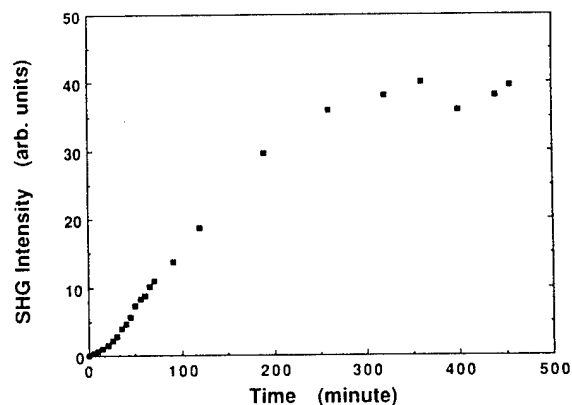


Fig. 3. Intensity of second-harmonic light generated in the film versus preparation time. The peak power coupled into the film for preparation was approximately 1 kW for the 1064-nm light and 5 W for the 532-nm light. The FGSH intensity was measured after coupling only 1064-nm radiation into the film with a peak power of 0.8 kW.

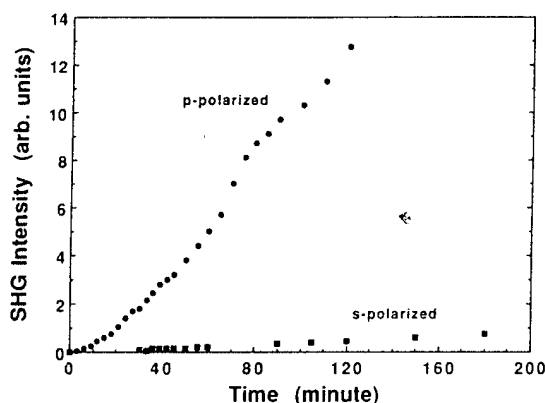


Fig. 4. Intensity of FGSH versus preparation time for *s*- and *p*-polarized input preparation beams. The output-coupled intensities of the 1064- and 532-nm preparation beams were the same for the two polarizations.

FGSH light could be observed visually near the saturation intensities.

Both the growth rate and the saturated intensity levels of the FGSH light produced in these doped thin films displayed a dependence on the polarization of the input beams, as illustrated in Fig. 4. The coupling angle for these data was chosen so that the ratio $I(2\omega)/I(\omega)$ was the same for both *s* and *p* polarizations, where $I(\omega) \approx 200 \mu\text{W}$ and $I(2\omega) \approx 4 \mu\text{W}$. The film was initially illuminated with *s*-polarized ω and 2ω light, and measurements were made as described above for time-dependent growth measurements. After the film was irradiated with the *s*-polarized beams for 3 h, a half-wave plate was adjusted to produce *p*-polarized ω and 2ω illumination. The change in the polarization to *p*-polarized input light produced a *p*-polarized FGSH signal that grew an order of magnitude faster than with *s*-polarized preparation light and a corresponding *s*-polarized output. The saturated intensities (not shown) of the FGSH light were also an order of magnitude greater for the *p*-polarization compared with the *s*-polarized light, but the time for the FGSH intensity to reach saturation was similar for both polarizations. This anisotropy in the polarization dependence may arise when preferentially ejected electrons predicted by some models¹² are effectively confined normal to the plane of the waveguide, while those ejected in the plane would diffuse, further producing a smaller effective χ^2 . This model would require either long-lived or multiple photoexcitations to move electrons to the waveguide boundary.

For the experiments described above, FGSH signals were observed only when the input beams propagated along their respective lowest-order waveguiding modes. The width of the waveguiding modes for ω and 2ω allowed a substantial fraction of the power at the optimal coupling angles to be propagated simultaneously in the film. Typically, the FGSH light was observed after only a few minutes of initiating propagation. In contrast, after 30 min of illumination, no FGSH light was observed for coupling into the second-order mode of the 1064-nm light. The lack of observed FGSH light for this mode

could be due to a mismatch of the optimal coupling angles for the ω and 2ω light, thereby reducing the intensity of copropagating beams. Alternatively, the antisymmetric nature of the second-order 1064-nm mode and the third-order 532-nm mode could produce poor overlap and thus no observable harmonic intensity.

In fiber experiments, grating erasure was demonstrated by a number of techniques, including propagating only the 2ω seed beam through the fiber.⁷ We attempted to erase the light-induced grating in the film by initially preparing the doped film with the *p*-polarized input beam in the lowest-order IR waveguiding mode and subsequently illuminating the film with only 2ω light after removing the 1064-nm input beam. The green seed beam illuminated the film at various 2ω coupling angles. After illumination at 532 nm for periods as long as 6 h, the initial preparation angles and $I(\omega)$ conditions were restored, and no decrease in the FGSH was observed.

In conclusion, we have made what is to our knowledge the first observation of harmonic generation in two-dimensional amorphous doped glass films. These results in thin films are in agreement with observations of growth and saturation of harmonic generation in fibers. The anisotropic response to the input polarization dependence produced by the thin-film geometry offers new insight into the mechanism of the second-harmonic effect. For future studies these films offer the capability of more controlled testing of the optical processing because of the ability to excite and detect specific waveguiding modes through prism coupling. In addition, the simplified geometry allows *in situ* characterization that can identify the microscopic cause of these effects.

We thank the Developmental Optical Facility at Phillips Laboratory, Kirtland Air Force Base, New Mexico, for film production and Scott Urban and Skip Pribyl for their assistance in data accumulation.

References

1. U. Österberg and W. Margulis, *Opt. Lett.* **11**, 516 (1986).
2. R. H. Stolen and H. W. K. Tom, *Opt. Lett.* **12**, 585 (1987).
3. R. H. Stolen, in *Nonlinear Waves in Solid-State Physics*, A. D. Boardman, T. Twardowski, and M. Bertolotti, eds. (Plenum, New York, 1990), pp. 297–324.
4. D. Z. Anderson, V. Mizrahi, and J. Sipe, *Opt. Lett.* **16**, 796 (1991).
5. L. J. Poyntz-Wright, M. E. Fermann, and P. St. J. Russell, *Opt. Lett.* **13**, 1023 (1988).
6. B. Ehrlich-Holl, D. M. Krol, R. H. Stolen, and H. W. K. Tom, *Opt. Lett.* **17**, 396 (1992).
7. A. Krotkus and W. Margulis, *Appl. Phys. Lett.* **52**, 1942 (1988).
8. U. Österberg, *Proc. Soc. Photo-Opt. Instrum. Eng.* **1171**, 192 (1990).
9. R. Kashyap, B. J. Ainslie, and G. D. Maxwell, *Electron. Lett.* **25**, 206 (1989).
10. R. Ulrich and R. Torge, *Appl. Opt.* **12**, 2901 (1973).
11. R. Swanepoel, *J. Opt. Soc. Am. A* **2**, 1339 (1985).
12. N. B. Baranova, A. N. Chudinov, A. A. Shulginov, and B. Ya. Zel'dovich, *Opt. Lett.* **16**, 1346 (1991).

Second Harmonic Generation in Low-Water Fused Silica by Proton Implantation

Leanne J. Henry

Frank J. Seiler Research Laboratory

2354 Vandenberg Drive, Suite 6H79

USAF Academy CO 80840-6272

Telephone: (719)472-3502, Fax (719) 472-3649

e-mail: henrylj%fjsrl%usafa@dfmail.usafa.af.mil

Thomas G. Alley

Frank J. Seiler Research Laboratory

2354 Vandenberg Drive, Suite 6H79

USAF Academy CO 80840-6272

Dennis S. Rand

Frank J. Seiler Research Laboratory

2354 Vandenberg Drive, Suite 6H79

USAF Academy CO 80840-6272

John J. Kester

Frank J. Seiler Research Laboratory

2354 Vandenberg Drive, Suite 6H79

USAF Academy CO 80840-6272

A nonlinear optical layer having a $\chi^{(2)}$ as high as 1.4 pm/V was generated in low-water fused silica by proton implantation.

Second Harmonic Generation in Low-Water Fused Silica by Proton Implantation

Leanne J. Henry, Thomas G. Alley, Dennis S. Rand and John J. Kester

Frank J. Seiler Research Laboratory
2354 Vandenberg Drive, Suite 6H79
USAF Academy CO 80840-6272
Tel. (719) 472-3502, FAX (719) 472-3649
e-mail - henrylj%fjsrl%usafa@dfmail.usafa.af.mil

Second harmonic generation (SHG) in poled fused silica, which was first reported by Myers, Mukherjee and Brueck⁽¹⁾ in 1991, has increased in importance because of a multitude of potential device applications. Such applications include electro-optic switching, frequency doubling crystals, parametric amplification, parametric oscillation, and linear electro-optic modulation/frequency conversion which can be monolithically integrated into optical fibers and planar integrated circuit geometries. Because of these potential applications, much work has been done to understand the phenomenon of SHG in poled fused silica.

In the past, a second-order nonlinearity has been induced in fused silica by either parallel plate⁽¹⁾ or corona poling.⁽²⁾ Through parallel plate poling, Myers et al.⁽¹⁾ were able to induce an optically active region of thickness 5-10 μm on the positively biased face of a sample. The second-order nonlinearity, $\chi^{(2)}$, associated with this region in natural fused quartz was found to be on the order of 1 pm/V. But, for the higher purity UV grade synthetic fused silica having only 10 percent as many impurities as natural fused quartz, the magnitude of the nonlinearity was found to be an order of magnitude lower.⁽¹⁾ Based on this data, Myers proposed that the SHG originated from a space charge region created by migrating impurity ions and electrons. This was further supported by the ratio of electro-optical coefficients, r_{33}/r_{31} , which was found by Long et al.⁽³⁾ to have a value of 3.0. This is consistent with ∞_{mm} symmetry and a space charge region.

Besides parallel plate and corona poling, nonlinearity has also been induced in various glasses by electron implantation. Kazansky et al.⁽⁴⁾ reported second-order nonlinearities as large as 0.7 pm/V upon implantation of lead silicate glass with electrons. Russell et al.⁽⁵⁾ also reported the generation of nonlinearity in lead glass, Ge doped silica glass, Nb doped silica glass, Ti+Zr doped silica glass, lead germanate glass and phosphate glass by electron implantation. Although nonlinearity was induced in the above mentioned materials, attempts to induce nonlinearity in fused silica by electron implantation have failed. In fact, Kazansky et al.⁽⁶⁾ reported the erasure of nonlinearity induced by thermal poling upon electron implantation.

Because of the apparent role of the space charge region in the generation of a second order nonlinearity, fused silica with a low-water content was implanted with protons in an attempt to break the centrosymmetry and produce a space charge region. Protons were implanted using a pelletron at energies ranging from 200 to 725 keV and dosages ranging from 0.25 to 3.0 mC. The depth of the implanted region increased from approximately 1.5 μm to 8.0 μm at proton energies of 200 and 725 keV, respectively. The level of SHG was studied in two ways: (1) as a function of proton implantation energy at a constant dosage of 2 mC (approximately 5×10^{16} protons/cm²),

and (2) as a function of dosage (0.25 to 3.0 mC) at a fixed proton energy of 526 keV. Upon implantation of the desired dosage of protons, the SHG profile was obtained by scanning a polarized 1.06 μm Q-switched Nd/YAG laser beam at an incident angle of 60° across a diameter of the irradiated region of the sample. Prior to striking the sample, the beam was reduced to between 10 and 60 mW of power and was filtered to remove 532 nm radiation. After traversing the sample and generating second harmonic, the beam was filtered to remove all radiation except wavelengths of 530 ± 10 nm. After measurement of the strength of the frequency doubled radiation with a PMT, the absolute level of d_{33} ($d_{33} = \frac{1}{2}\chi^{(2)}$) obtained by comparison with a y-cut quartz standard.

To evaluate the distribution of optical activity in the irradiated region of the sample, linear scans were performed across a diameter of the irradiated area, and each point recorded was the time averaged response of a photomultiplier tube to the SHG signal. For a proton implantation energy of 253 keV, Figure 1a, we found the distribution of nonlinearity induced within the irradiated area to be a maximum at the center of the region, falling off on either side. But, as the proton implantation energy increased, the strong central region became an optically active annulus of increasing diameter (Figure 1b). The central region which had no visible damage, showed very little nonlinearity. The annular region, on the other hand, was quite optically active. The peaks in Figure 1b correspond to the linear scan passing through opposite sides of the annulus. The optically active annulus and less optically active central region are believed to originate from an accelerator beam profile which became annular with increasing diameter as the implantation energy increased. As a result, the portion of the sample corresponding to the beam center probably received very little irradiation and, therefore, had much less optical activity. Kazansky et al.⁽⁵⁾ observed a similar distribution of nonlinearity in lead silicate glass that had undergone electron beam irradiation. A second harmonic signal was observed at the edges of the irradiated region which was twice that in the center.

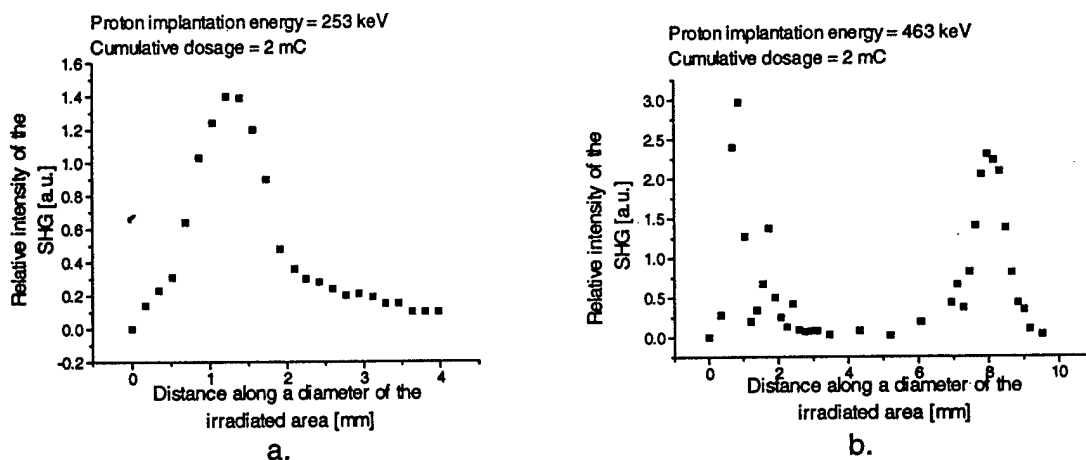


Figure 1 - Relative intensity of the SHG [a.u.] vs distance [mm] along the sample surface for a cumulative proton dosage of 2 mC. Proton implantation energies are: a. 250 keV, b. 463 keV.

The strength of the nonlinear optical signal was first evaluated as a function of the proton implantation energy which ranged from 200 keV to 725 keV at a constant dosage of 2 mC. Upon evaluation of the nonlinear optical coefficient, d_{33} , for the various proton energies (Figure 2) d_{33} was found to be dependent on the proton energy. Each

point in Figure 2 represents a different sample. Each d_{33} value was calculated from the maximum SHG signal found along a single linear scan through the implanted region of the sample. Because a linear scan through a different line of the implanted area might produce a slightly different result, these values are believed to be good within ± 0.1 pm/V. Saturation of d_{33} in the range 0.5 to 0.6 pm/V appeared to occur for proton energies in excess of 410 keV. One exception was found to occur for a sample of fused silica implanted with 568 keV protons where a d_{33} value of 0.68 was generated. Finally, from Figure 2, a minimum proton implantation energy of approximately 350 keV was found to be necessary to generate substantial nonlinearity in fused silica.

One conclusion that can be drawn based on the above data is that proton implantation of fused silica is capable of creating a nonlinear optical region exhibiting a value of d_{33} at least as large as obtainable from parallel plate poling (i.e., approximately 0.5 pm/V). In addition, the potential exists for even larger nonlinearities as evidenced by the d_{33} value of 0.68 pm/V generated by a proton implantation energy of 568 keV.

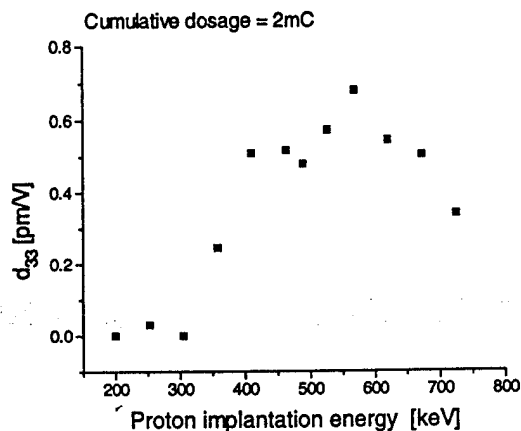


Figure 2 - Maximum d_{33} [pm/V] vs proton implantation energy [keV].

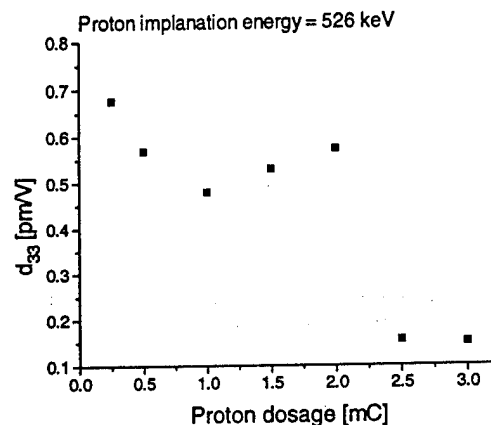


Figure 3 - Max. d_{33} [pm/V] vs dosage [mC] for a proton implantation energy of 526 keV.

The effect of proton dosage at a fixed implantation energy of 526 keV was studied next. This particular proton energy was selected because of its relatively large nonlinear response at a dose of 2 mC. The dosages studied ranged from 0.25 mC to 3.0 mC. As is apparent from Figure 3, values of the nonlinear optical coefficient, d_{33} , ranging from 0.48 to 0.68 pm/V were obtained at dosage levels between 0.5 and 2.0 mC. When compared to the nonlinear optical coefficient, d_{33} , produced by parallel plate poling, the values of d_{33} produced by proton implantation using these parameters are up to 36 percent greater. Another observation apparent from Figure 3 was that as the dosage level increased, the level of d_{33} achieved decreased after a certain point. This was most likely due to extensive lattice damage brought about from prolonged proton bombardment.

In conclusion, the distribution of SHG on the surface of a sample of irradiated fused silica was found to become an annulus of increasing diameter as the energy of the proton beam increased. This damage pattern was most likely the result of an annular beam profile brought about by repulsion of the positively charged protons. By smoothing out the beam profile or moving the sample during irradiation, it should be

possible to induce a uniform area of nonlinearity stronger than that achievable through traditional parallel plate poling.

In addition, for a constant dosage of 2 mC, a threshold proton implantation energy of 400 keV was found to be necessary to generate a nonlinear region in a sample of fused silica. As the proton implantation energy increased above 358 keV, $\chi^{(2)}$ (where $\chi^{(2)} = 2d_{33}$) appeared to generally saturate between 1.0 and 1.2 pm/V for proton implantation energies greater than 400 keV. One exception was found for a proton energy of 568 keV which produced a value of $\chi^{(2)}$ of 1.4 pm/V. For a proton implantation energy of 526 keV, the optimum dosage level was found to be between 0.25 and 2.0 mC. At these levels, values of $\chi^{(2)}$ between 1.0 and 1.4 pm/V were found to occur. Finally, values of $\chi^{(2)}$ larger than 1.4 may be achievable by finding the optimal combination of proton implantation energy and dosage.

References

1. R. A. Myers, N. Mukherjee and S. R. J. Brueck, Opt. Lett. **16** 1732 (1991).
2. A. Okada, K. Ishii, K. Mito and K. Sasaki, Appl. Phys. Lett. **60** 2853 (1992).
3. X. -C. Long, R. A. Myers and S. R. J. Brueck, Opt. Lett. **19**(22) 1819-1821 (1994).
4. P. G. Kazansky, A. Kamal and P. St. J. Russell, Opt. Lett. **18**(9) 693-695 (1993).
5. P. St. J. Russell, P. G. Kazansky and A. Kamal, SPIE (Photosensitivity and self-organization in optical fibers and waveguides) **2044**, August 1993, Quebec, Canada.
6. P. G. Kazansky, A. Kamal and P. St. J. Russell, Opt. Lett. **18**(14) 1141-1142 (1993).

**First-Principles Characterization of Structure and Properties of E' Centers
in Silica Glass**

Shashi P. Karna

Frank J. Seiler Research Laboratory

2354 Vandenberg Dr., Suite 2A35

United States Air Force Academy CO 80840-6272

Phone: (719) 472-2655

Fax: (719) 472-3649

e_mail: karna@gauss.usafa.af.mil

John J. Kester

Frank J. Seiler Research Laboratory

2354 Vandenberg Dr., Suite 6H79

United States Air Force Academy CO 80840-6272

Phone: (719) 472-3122

Fax: (719) 472-3649

e_mail: KesterJJ%FJSRL%USAFA@dfmail.usafa.af.mil

Electronic structure and properties of E' center and its precursor in α -SiO₂ have
been calculated for the first time by *ab initio* Hartree-Fock method.

First-Principles Characterization of Structure and Properties of E' Centers in Silica Glass

Shashi P. Karna and John J. Kester
Frank J. Seiler Research Laboratory
2354 Vandenberg Dr., Ste 2A35
U.S. Air Force Academy CO 80840-6272
Phone: (719) 472-2655
FAX: (719) 472-3649

The recent observations of second harmonic generation (SHG) of the infrared (IR) light in doped silica glass fibers,^{1,2} planar waveguides,^{3,4} and poled silica glass⁵ have attracted a great deal of attention in understanding the mechanism and origin of nonlinear optical (NLO) processes in $a\text{-SiO}_2$. A number of possible mechanisms have been proposed^{6,7} to explain the experimental observations. However, in so far as these phenomenological models describe the observed SHG in fibers and waveguides, they do not address the microscopic mechanism of optical nonlinearity in silica glass. An understanding of the atomic-scale mechanism of NLO properties in $a\text{-SiO}_2$ is important, not only for increasing our fundamental knowledge, but also for modeling new materials with yet enhanced optical susceptibility and faster response time for device applications. Here we present the results of first-ever *ab initio* studies of microscopic structure-NLO property relationships in systems containing free spin electrons, such as $a\text{-SiO}_2$.

Considering the structure of $a\text{-SiO}_2$ as a continuous random network of Si-O,⁸ its second order NLO coefficient, $\chi^{(2)}$, should vanish by virtue of symmetry. The possibility of observing SHG in silica glass based materials, therefore, requires a non-centrosymmetric structure created either by intrinsic defects or by external dopants. In this work, we concentrate on characterizing the *intrinsic* defect and its possible contribution to the observed NLO properties of $a\text{-SiO}_2$.

Among the various intrinsic defects identified to date, the E' centers constitute the single most important paramagnetic point defect in amorphous silica.⁹ From the similarity of the electron spin resonance (esr) spectrum of the γ -ray irradiated silica glass with that observed in radiation induced α -quartz,¹⁰ Griscom concluded¹¹ that the atomic-scale structure of the paramagnetic center in $a\text{-SiO}_2$ was similar to that of E_1' . The current accepted structure of the E_1' centers in α -quartz is based on the Feigl, Fowler and Yip model.¹² According to this model, the E_1' center in irradiated quartz is produced by asymmetric relaxation of $\equiv\text{Si-Si}\equiv^+$ created by an O⁻ vacancy. The unpaired electron spin is located on a tetrahedral Si atom in the Si-O (sp^3 hybridized) bond and the 'hole' containing Si (Si^+ ion) relaxes to sp^2 hybridization, containing its three SiO bonds in the same plane. The two types of Si centers in E' in this model are characterized by the two distinct (423 G and 8G) hyperfine splitting observed in the esr spectrum and both attributed to ^{29}Si nuclei ($I=1/2$).

The extensive work of Griscom,^{9,11} aided by the quantum mechanical studies of Fowler and coworkers^{12,13} in the past several years have recognized the E' , the E_1' equivalent in silica glass. It is now also believed the E' centers constitute the intrinsic Frenkel defects (vacancy-interstitial pairs) in amorphous silica created by melt quenching and/or the action of ionizing particle irradiations.⁹

In order to establish the structure-NLO property relationship of E' , we have calculated the geometry, one-electron properties, and linear and nonlinear optical properties of four model systems by the *ab initio* Hartree-Fock method. The model systems selected (Fig. 1) for our study, though smaller in dimension than one would consider adequate for modeling purposes, contain all the essential structural features of the proposed E' center⁹ and its precursor. The

technical advantage of selecting the four model systems of the present study is that it allowed us to perform accurate calculations by the first-principles quantum mechanical method.

The oxygen vacancies (II-IV) will be designated as follows: Structure II will be denoted as V_O^0 , structure III will be denoted as V_O^{+1} , and structure IV will be denoted as V_O^{-1} . The notation is such that V_O denotes an oxygen vacancy and the superscript indicates the charge on the vacancy. Accordingly, a positive charge indicates a 'hole' and a negative charge indicates an 'electron'. The precursor, (structure I) will be denoted as P. The geometry of P and the three vacancies, V_O^0 , V_O^{+1} , and V_O^{-1} were optimized by the *ab initio* Hartree-Fock method using a double zeta plus polarization (DZP) Gaussian type basis set. For the property calculations, the DZP basis was further augmented by adding a set of diffuse p (0.025) and d(0.025) functions on Si, diffuse p(0.05) and d(0.05) functions on O, and a diffuse p(0.1) function on H. The numbers in parentheses are the orbital exponents.

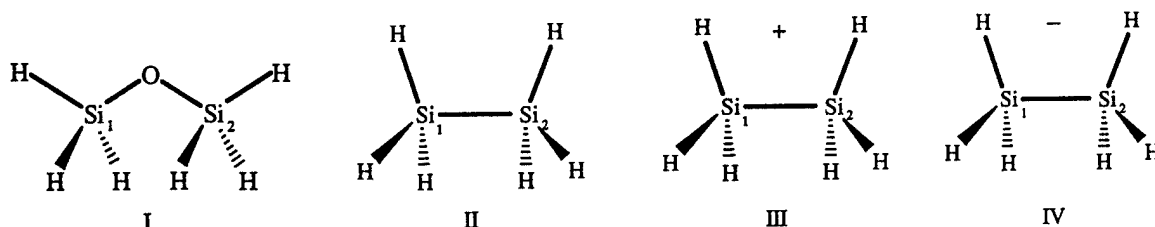


Figure 1.

The geometry optimization and the calculation of one-electron properties were performed by the HONDO-8 suite of programs.¹⁴ The linear and the nonlinear optical properties were calculated using the recently developed XNLOP program.¹⁵ The XNLOP program is a general purpose computer code for calculating the static (dc field) and dynamic (frequency-dependent) linear and NLO properties of molecules within the framework of the time-dependent coupled perturbed Hartree-Fock (TDCPHF) theory. The details of the TDCPHF method for the closed shell systems are described in the works of Karna and Dupuis,¹⁶ Karna,¹⁷ and those for the open-shell systems have been given in a recent work by Karna.¹⁵

The calculated bond distance and bond angles of the systems were in reasonable agreement with the available experimental^{18,19} and the most recent theoretical values²⁰ For example, the $R_{Si-O}=1.633$ Å, $R_{Si-H}=1.474$ Å, $\angle SiOSi=150$ degrees, and $\angle HSiO=109.5$ degrees obtained for P (structure I) in the present study, agrees well with the corresponding values obtained recently in a similar calculation²⁰ and also with the experimental data.¹⁹ We believe the calculated geometries of other structures (II-IV) also have similar accuracy. During the geometry optimization, no attempt was made to force the symmetry on the structures. This had the effect that in the systems where symmetry would cause the dipole moment to vanish, e.g. in V_O^0 , the relaxed geometry leads to a nonzero value of the dipole moment.

Table 1. Calculated values of R_{Si-Si} (Å) and dipole moment (D)

Structure	I	II	III	IV
R_{Si-Si}	3.164	2.367	2.786	3.370
μ_x	-0.00258	0.01344	0.00262	0.14997
μ_y	-0.30653	0.11267	0.02290	0.14714
μ_z	0.05827	0.00923	-0.00109	0.02770
$ \mu $	0.31204	0.11384	0.02307	0.14997

In order to examine the geometry relaxation and its effect on calculated properties, the calculated Si-Si distance and the dipole moment of structure I - IV are listed in Table 1. It is noted that a neutral O vacancy brings the two Si atoms much closer by about 0.08 Å with respect to the precursor (P). A negative O vacancy (O⁻) creating the V_O⁺¹ structure also brings the two Si atoms closer with respect to P, but the decrease in the Si-Si bond length is now smaller than that in V_O⁰. On the other hand, a positive O vacancy (O⁺) that leaves behind an electron, thus creating V_O⁻¹, considerably elongates the Si-Si distance with respect to P.

The calculated changes in the Si-Si distance is consistent with the composition of the highest occupied molecular orbital (HOMO). In the case of P, the HOMO is a *nonbonding* p_z orbital situated on the oxygen atom. In the case of V_O⁰ the HOMO is a σ-type (sp³) *bonding* MO and the lowest unoccupied molecular orbital (LUMO) is its *antibonding* complement, a σ-type (sp³) orbital. In the case of V_O⁺¹, an electron is removed from the σ bonding MO of the neutral vacancy which leads to the weakening of the binding between the Si atoms and elongation of the Si-Si bond. In the case of V_O⁻¹, an electron is added in the antibonding (σ*) MO of the neutral vacancy which destabilizes the bonding between the Si atoms, resulting in a large R_{Si-Si}.

The components of the linear polarizability tensor, α(-ω;ω), and first-hyperpolarizability tensor, β(-2ω;ω,ω), for the two neutral species, P (structure I) and V_O⁰ (structure II), calculated at a fundamental wavelength, λ=1.064 μm are listed in Table 2. It is noted that whereas the linear polarizabilities of the precursor and the neutral oxygen vacancy are very similar, the NLO polarizability tensor is vastly different for the two structures. In fact, the observable vector quantity, β_i (= Σ_j (β_{ijj}+β_{jij}+β_{jjj})/5) for the V_O⁰ structure is vanishingly small because of its nearly centrosymmetric structure.

Table 2. Components of α(-ω;ω) (10⁻²⁴ esu) and β(-2ω;ω,ω) (10⁻³² esu) for P (structure I) and V_O⁰ (structure II) calculated at λ=1.064 μm

Struct.	α _{aa}	α _{bb}	α _{cc}	β _{aab}	β _{bbb}	β _{bbc}	β _{bcc}	β _{ccc}
I	8.27	7.35	7.40	5.85	6.71	-0.02	11.86	0.03
II	10.65	7.68	7.67	-0.24	-7.13	10.27	7.75	-10.27

Even if the V_O⁰ had a completely non-centrosymmetric structure, as would be expected in silica glass, its NLO coefficient is expected to be quite small due to the fact that the outermost electrons in its valence space occupy a strongly bonded σ MO.

Table 3. The hyperfine coupling constants, a_{iso} (G), and T_{ii} (G) for V_O⁺¹ and V_O⁻¹

Struct.	Center	a _{iso}	T _{xx}	T _{yy}	T _{zz}
III	Si ₁	-17.77	15.84	15.68	-31.52
	Si ₂	-17.75	15.83	15.67	-31.50
IV	Si ₁	-323.21	13.64	12.55	-26.19
	Si ₂	-323.74	13.75	12.55	-26.30

The ²⁹Si hyperfine coupling constants of the two paramagnetic species, V_O⁺¹ (structure III) and V_O⁻¹ (structure IV), calculated by spin-unrestricted Hartree-Fock method are listed in Table 3. It is immediately clear that the 420 G spectrum observed by Griscom¹¹ could not be

due to a V_O^{+1} center. Such a large hyperfine splitting, according to the present calculation would require excess electron spin on the Si nuclei, as may be possible by an 'electron' trapping, resulting in a V_O^{-1} (structure IV) type structure. Of course, the smaller hyperfine splitting of 8G observed by Griscom¹¹ could very well be due to a V_O^{+1} center as the present calculation does yield a small a_{iso} value for this species. In fact, the value of a_{iso} for V_O^{+1} calculated after removing the lowest contaminating component from the spin density matrix, reduces to ~11 G, in much closer agreement with the experiment. An important implication of these results is that it does not fully support the hitherto accepted structure of the E' center.^{9,12,13} Rather, the present study indicates an 'electron'-'hole' pair having two ^{29}Si nuclei with distinct electronic environments as the source of the observed esr spectra. A more detailed analysis of the electronic and NLO properties of the model E' systems, presently underway in our laboratory, will be able to provide additional information about the structure of this important defect in silica glass.

References

1. U. Österberg and W. Margulis, *Opt. Lett.* **11**, 516 (1986)
2. R. H. Stolen and H. W. K. Tom, *Opt. Lett.* **12**, 585 (1987)
3. J. J. Kester, P. W. Wolf, and W. R. White, *Opt. Lett.* **17**, 1779 (1986).
4. P. S. Weitzman, J. J. Kester, and U. Österberg, *Electron. Lett.* **30**, 697 (1994).
5. R.A. Myers, N. Mukherjee, and S.R.J. Brueck, *Opt. Lett.* **16**, 1732 (1991).
6. V. Dominic and J. Feinberg, *Phys. Rev. Lett.* **71**, 3446 (1993).
7. M. L. Brauer, I. Dajani, and J. J. Kester, *Electron. Lett.* **30**, 297 (1994).
8. W. H. Zachareisen, *J. Am. Chem. Soc.* **54**, 3841 (1932).
9. D. L. Griscom, *Proc. Mat. Res. Soc.* **61**, 213 (1986).
10. R. H. Silsbee, *J. Appl. Phys.* **32**, 1459 (1961).
11. D. L. Griscom, *Phys. Rev. B* **20**, 1823 (1979); *ibid.* **22**, 4192 (1980).
12. F. J. Feigl, W. B. Fowler, and K. L. Yip, *Solid State Commun.* **14**, 225 (1974).
13. K. L. Yip and W. B. Fowler, *Phys. Rev. B* **11**, 2327 (1975); J. K. Rudra and W. B. Fowler, *Phys. Rev. B* **35**, 8223 (1987) and references therein.
14. M. Dupuis, A. Farazdel, S. P. Karna and S. Maluendes, *Modern Techniques in Computational Chemistry*, Ed. E. Clementi (ESCOM, Leiden, 1990), p. 277.
15. S. P. Karna, *J. Chem. Phys.*, submitted for publication.
16. S. P. Karna and M. Dupuis, *J. Comp. Chem.* **12**, 487 (1991).
17. S. P. Karna, *Chem. Phys. Lett.* **214**, 186 (1993).
18. J. A. Aronson, R. C. Lord, and D. W. Robinson, *J. Chem. Phys.* **33**, 1004 (1960).
19. M. J. Barrow, E. A. V. Ebsworth, and M. M. Harding, *Acta. Crystall. B* **35**, 2093 (1979).
20. M. R. Bär and J. Sauer, *Chem. Phys. Lett.* **226**, 405 (1994), and references therein.

Modal and Polarization Properties of SHG in Doped-Silica Waveguides:

Transverse Modulation Effects

John J. Kester

Frank J. Seiler Research Laboratory

2354 Vandenberg Dr., Suite 6H79

USAF Academy CO 80840-6272

Tel. (719) 472-3133, FAX (719) 472-3649

e-mail KesterJJ%FJSRL%USAF@dfmail.usafa.af.mil

Iyad Dajani

Frank J. Seiler Research Laboratory

2354 Vandenberg Dr., Suite 6H79

USAF Academy CO 80840-6272

Peter Ranon

Frank J. Seiler Research Laboratory

2354 Vandenberg Dr., Suite 6H79

USAF Academy CO 80840-6272

Thomas Alley

Frank J. Seiler Research Laboratory

2354 Vandenberg Dr., Suite 6H79

USAF Academy CO 80840-6272

Waveguide mode combinations and polarization effects are measured and calculated for planar germanium-doped silica waveguides.

Modal and Polarization Properties of SHG in Doped-Silica Waveguides: Transverse Modulation Effects

John J. Kester, Iyad Dajani, Peter Ranon, and Thomas Alley

Frank J. Seiler Research Laboratory
2354 Vandenberg Dr., Suite 6H79
USAF Academy CO 80840-6272
Tel. (719) 472-3133, FAX (719) 472-3649
e-mail KesterJJ%FJSRL%USAF@dfmail.usafa.af.mil

The generation of second harmonic light in optically modified fibers¹ and thin films² has been shown to arise from a periodic modulation of the second-order susceptibility, $\chi^{(2)}$, along the direction of propagation.³ This longitudinal modulation allows the phase matching of the generated second harmonic light with the fundamental wave. The efficiency of the second harmonic for different waveguiding modes and different polarizations is governed by an additional modulation in the transverse direction. The overlap of $\chi^{(2)}$ with the transverse profiles of the optical electric fields across the waveguide, as described by the overlap integral, governs the modal response of the waveguide generated light.⁴ Unlike the traditional second harmonic generation (SHG) processes, the overlap integrals describing higher order modal combinations may be on the same order as the overlap integral describing the combination of the lowest order modes. In planar waveguides the difference in the transverse charge density governs the polarization dependence.

Theoretical predictions of second harmonic light from various fiber mode combinations have indicated that relative efficiencies within an order of magnitude are possible for lower order modes.⁵ Furthermore, they found the fiber-generated SHG was produced in the same mode as that used during the seeding process. Recent experimental work with modal combinations in fibers showed that while the seeding was typically carried out with one second harmonic mode, the fiber generated SHG was reported in a number of modes.⁶ In one experiment the SHG was not observed in the second harmonic seeding mode.

We report here on the modal and polarization properties of SHG in germanium-doped planar waveguides. While there has been experimental observation of polarization effects in planar waveguides² no theoretical models have been proposed. The film-generated second harmonic (FGSH) was measured for different modal combinations and polarizations and was compared to the theoretical predictions based on the asymmetric photoionization model. The cause of the variation in the efficiency for different mode combinations is attributed to the confinement of the beams within the waveguide and the overlap integrals. These modal combinations can be used for possible optical switch applications.

The waveguides were produced by ion beam sputtering and consisted of 6M percent of germania in silica. The experimental setup is shown in Fig. 1. A fundamental beam at 1.06 μm was produced by a Q-switched mode-locked Nd:YAG laser. A second harmonic beam, produced by KDP, was separated and recombined with a slight offset to allow prism coupling into specific waveguiding modes of the film with TM or TE polarization. After simultaneous illumination by the fundamental and second harmonic beam, FGSH light was observed by reading the grating with a fundamental beam having a power equal to the power of the writing beam.

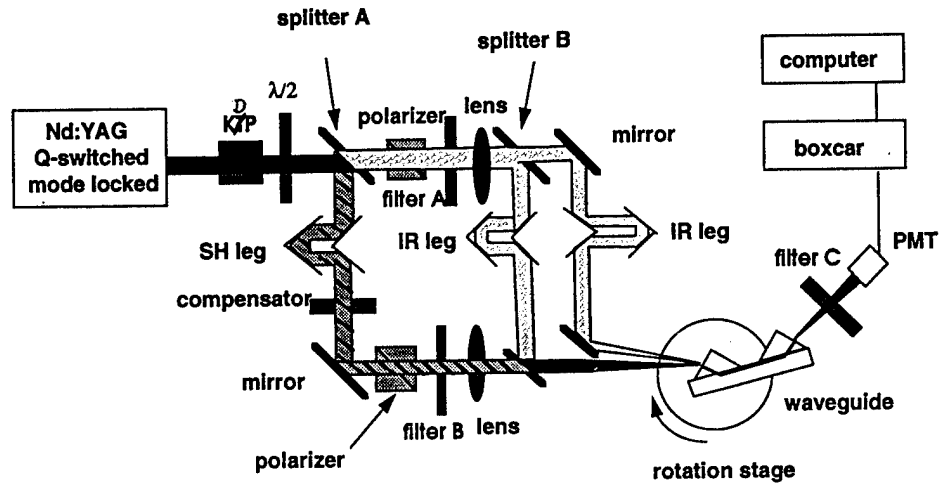


Figure 1. Experimental setup

Films prepared with both beams in either TM or TE polarization show almost three orders of magnitude difference in FGSH light (Fig. 2). This difference is not due to differences in the overlap integral between the two polarizations, but rather to the space charges that arise due to the asymmetric photoionization current⁷, $J_{pi} \propto E_{\omega}^2 E_{2\omega}$, and the backfield field current, $J_{bf} = \sigma^{(1)} E_{DC}$, where $\sigma^{(1)}$ is the linear conductivity. At saturation the continuity equation, $\frac{\partial \rho}{\partial t} + \nabla \cdot J = 0$, yields $\nabla \cdot J = 0$. However, the most general solution is not $J_{pi} = -J_{bf}$, but rather, $\nabla \cdot (J_{pi} + J_{bf}) = 0$. Only by adopting the general solution can one explain the difference in FGSH power between the two polarizations. The photoionization current will be the same for either polarization, however, the divergence of the current is much larger for the TM configuration. The larger divergence in the current for the TM polarization will yield a larger charge density and higher effective second order susceptibility. This has been verified through numerical simulations.

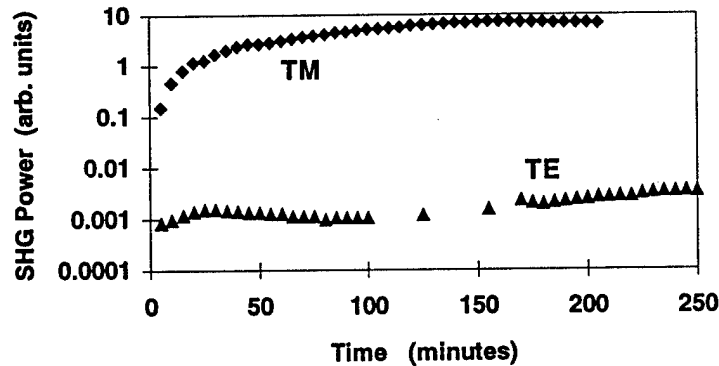


Figure 2. Growth of film generated second harmonic for TM and TE polarizations

Using only TM polarization the planar waveguides were conditioned using the fundamental and second harmonic in various lower order mode combinations. For each mode combination the FGSH was allowed to grow until saturation. The output FGSH

powers were then normalized to the lowest order mode combination and by the factor $1/P_{\omega}^4 P_{2\omega}$ for the seeding beams powers (Table 1.).

When the film was conditioned by seeding in one particular mode, the subsequent FGSH light was observed substantially in the same order mode. Some light was observed in adjacent modes. However, the percentage of FGSH light observed in other modes was in exactly the same percentage ($\pm 0.2\%$) as that observed for scattering of light from one mode to another within the waveguide. Thus, there is no appreciable SHG light generated in other modes that is in excess of the FGSH scattered light from the mode in which it was conditioned.

The relative power generated is calculated for various low order mode combinations by normal mode analysis.⁸ For TM modes, the dominant component of the electric field is in the transverse direction, i.e., normal to the plane of the waveguide. In the case where the writing and reading IR beams are in the same mode, the overlap integral describing the FGSH produced in the same waveguiding mode as the seed green is:

$$G(z) = \int_{-a}^a \int_{-\infty}^{\infty} \chi_{iii}^{(3)} [|\Phi_{1,k}|^4 + (r_1 + 1/3) \Phi_{1,k}^2 \Psi_{1,k}^{*2} + (1/3) r_1 |\Psi_{1,k}|^4] \Phi_{2,l}^2 + ((r_2 + 2/3) \times |\Phi_{1,k}|^2 \Phi_{1,k} \Psi_{1,k}^* + (1/3)(2r_1 + r_2) \Phi_{1,k} |\Psi_{1,k}|^2 \Psi_{1,k}^*) \Phi_{2,l} \Psi_{2,l}^* + (2/3) r_2 |\Phi_{1,k}|^2 |\Psi_{1,k}|^2 |\Psi_{2,l}|^2] dx dy \quad (1)$$

where the IR beams are assumed to be in mode k , the seed and generated green are assumed to be in the mode l , and where Φ and Ψ represents the transverse profiles of the transverse and longitudinal components of the optical fields. The coefficients r_1 and r_2 are obtained from experimental results.⁹

The predicted FGSH powers are listed in Table 1 with two different normalizations. The column marked *Total Predicted Power* calculates the power in various modes when normalized to the total power propagating in the waveguide for the conditions used in our experimental setup. This column can then be compared with the experimental results observed. A very rough correlation can be observed between the experimental and calculated SHG powers. The difference is primarily attributed to variability among the mode combinations in the temporal and spatial overlap of the fundamental and second harmonic used for conditioning the waveguide. In addition, the input and output prism coupling efficiency varies from one mode combination to another. However, the key point is that SHG can be produced in various mode combinations and that they have been predicted and measured to be within an order of magnitude for lower order modes.

Table 1. Experimental and predicted SHG powers for various mode combinations

Fundamental Mode	Second Harmonic Mode	Measured Power	Total Predicted Power	Waveguide Predicted Power
0	0	1.0	1.0	1.0
0	1	0.39	0.30	0.31
0	2	0.51	0.36	0.38
1	0	0.10	0.13	0.28
1	1	0.34	0.40	0.89
1	2	0.58	0.21	0.48

Contributions from modal confinement and the overlap integral were examined. The column marked *Waveguide Predicted Power* normalizes the output to the power confined within the waveguide itself. This column excludes power that is outside the

waveguide in the evanescent fields. When comparing the calculated total power and waveguide power it is observed that ratios are similar for a specific fundamental waveguide mode. When the fundamental mode increases from zeroth to first order, a large discrepancy is observed due to the increased electric fields outside the waveguide. With better confinement conditions the SHG powers in the $TM_{\omega,1}$ - $TM_{2\omega,1}$ could be up to 90% of the $TM_{\omega,0}$ - $TM_{2\omega,0}$ mode combination.

A waveguide was then modified to produce multiple gratings within the same spatial region of the waveguide. The waveguide was modified by directing a fundamental and second harmonic beam into the film as described above. The FGSH was allowed to grow to a specific level. The same region of the waveguide was then illuminated by directing a fundamental beam into a different waveguide mode along with the second harmonic beam in the same mode used previously. There was no FGSH initially observed with this mode combination. A FGSH signal was allowed to grow from this new mode combination to a level similar to the first mode combination. While some erasure of the original grating occurred during the growth of the second grating, second harmonic light was observed in the same mode (the same mode originally used to condition the film) when illuminated by only the fundamental beams from either of the two waveguiding modes. With proper temporal and spatial overlap the second harmonic beams can be made to interfere, which is the basis of an optical switch.

In conclusion we have found that combining different waveguiding modes produces the same order of magnitude FGSH as the lowest order mode combination. Unlike fibers, the FGSH was produced in the same waveguiding mode as the seed second harmonic wave. Furthermore, we found that TM modes produced many orders of magnitude greater SHG power than the TE modes. This is due primarily to the greater charge density induced with TM polarization, and appears to be consistent with the asymmetric photoionization model.

References

1. U. Osterberg and W. Margulis, Opt. Lett. **11**, 516 (1986).
2. J. J. Kester, P. Wolf, and W. R. White, Opt. Lett. **17**, 1779 (1992).
3. H. Stolen and H. W. K. Tom, Opt Lett **12**, 585 (1987).
4. R. H. Stolen, in Nonlinear Waves in Solid State Physics, A. D. Boardman, T. Twardowski, and M. Bertolotti, eds (Plenum, New York), pp 297-324, (1990).
5. P. S. Weitzman and U. Osterberg, IEEE J Quantum Elec. **29**, 1437 (1993).
6. B. Poumellec, Optical Materials **3**, 169 (1994)
7. E. Dianov, P. Kazansky, and D. Yu Stepanov, Sov J. Quantum Elect. **19**, 575 (1990).
8. I. Dajani, J. Mod. Optics (accepted for publication).
9. V. Dominic, Ph.D. Thesis, Univ of Southern California (1993).

Second-harmonic generation efficiencies in germanium-doped planar waveguides: a normal-mode analysis

I. Dajani, Frank J. Seiler Research Laboratory,
United States Air Force Academy, Colorado Springs, CO 80840-6272

June 14, 1995

Abstract

Second-harmonic generation in germanium-doped silica planar waveguides seeded by a fundamental wave and its second harmonic is investigated using normal-mode analysis. The effects of self- and cross-phase modulation are included in this analysis. A set of two coupled equations that describe the evolution of the amplitude of the writing second-harmonic beam along the direction of propagation is obtained. The solution to these coupled equations is used to write the effective $\chi^{(2)}$ grating. This grating is then used to determine the second-harmonic power generated when the beam is read with only a fundamental wave propagating in a particular waveguiding mode. Due to diffraction, the conversion efficiency saturates as a function of waveguide length. It is also found that if the reading fundamental wave is in the same mode as the writing fundamental wave, relatively significant SHG is obtained with the generated second harmonic wave propagating primarily in the same mode as the seed second-harmonic wave. The power generated in any of the higher order modes is on the same order as that for the lowest order mode.

1 Introduction

Efficient doubling of 1064nm radiation was originally observed in germanium-doped silica fibers [1]. The fibers used in the early experiments were illuminated with intense infra-red light for several hours before green light (532nm) could be observed. It was later demonstrated that the

preparation time can be reduced considerably if the fibers were additionally treated with a small amount of green light [2]. This process is known as external seeding. Typically, in such a process, the second-harmonic power grows for about 30 minutes before finally saturating. Efficiencies of up to 5 percent have been achieved. More recently researchers have been able to observe this process in germanium-doped optical planar waveguides [3].

Since silica is centro-symmetric, its second-order susceptibility $\chi^{(2)}$ vanishes. Thus, it appears that efficient second-harmonic generation (SHG) in glass should not be possible. Several theories have since been proposed to explain this surprising phenomenon. Although this phenomenon is not yet fully understood, it is now generally agreed upon that a semi-permanent dc electric field is produced via a third-order or higher optical process in the fiber [2, 4, 5, 6]. This dc field breaks down the inversion symmetry and produces a non-vanishing $\chi^{(2)}$. A non-vanishing $\chi^{(2)}$, however, is not sufficient for efficient SHG. Due to linear dispersion effects, phase-matching generally cannot be maintained as the wave and its second-harmonic travel along the waveguide, and thus, even with a non-vanishing $\chi^{(2)}$ efficient SHG might not be achieved. Therefore, it appears that the induced $\chi^{(2)}$ is also periodic in the direction of propagation with a periodicity matching the phase mismatch between the fundamental and its second harmonic.

The infra-red peak power used in the fibers and planar waveguide experiments is usually on the order of 10 KW, with the green seed power typically being two orders to three orders of magnitude less. The effective transverse area is typically on the order of $10^{-11}m^2$. Therefore, the induced optical dc field obtained through a four-wave mixing process is on the order of a few hundred volts per meter. It can be shown that the required induced semi-permanent dc field is a few orders of magnitude higher than the optical dc field [7]. Researchers were able to generate efficient SHG by applying an external periodic dc electric field to both germanium-doped silica fibers and planar waveguides [8, 9]. The required external field was on the order of a few MV/m [10]. It was therefore hypothesized by some researchers that the nonlinear interaction of the optical fields causes some form of charge separation that leads to a build-up in an internal dc electric field which eventually saturates. One promising model that explains this charge separation is the asymmetric photoionization model [11, 12, 13]. In this model, one and two photon absorption processes interfere resulting in electrons being ejected in a preferential direction. In its simplest form, the asymmetric

photoionization current is given by:

$$j \propto E_{\omega}^{*2} E_{2\omega} + c.c. \quad (1)$$

The resulting dc electric field, E_{dc} , then interacts with the optical fields to produce SHG through a four-wave mixing process characterized by $\chi^{(3)}(-2\omega; 0, \omega, \omega)$, where $\chi^{(3)}$ is the third-order susceptibility. Therefore, the induced $\chi^{(2)}$ is given by:

$$\chi^{(2)} = 3\chi^{(3)} E_{dc} \quad (2)$$

We examine here this process of second-harmonic generation in thin-film planar waveguides for *TM* launched modes. This is motivated by experimental results that showed much higher SHG efficiencies for *TM* launched modes than those obtained for *TE* launched modes [3]. Thus, the induced dc electric field builds-up more effectively normal to the waveguide (along the optic axis) than in the plane of the waveguide. Using normal-mode analysis, and including the effects of self-phase and cross-phase modulation, we compute the efficiency of generating different waveguiding modes for various combinations of infra-red and green waveguiding modes during the writing process. Infra-red light in different modes is also used during the reading process.

2 Derivation of amplitude equations

We will now derive the equation that describes the evolution of the complex amplitude of the second-harmonic light using normal-mode analysis. It should be pointed out that we are considering a time-independent model, and thus we do not address the saturation of this process in time. We note, however, that a normal-mode analysis will offer a considerable reduction in computational time over more numerically-based techniques. This is crucial for the time-dependent case in which coupled equations for the induced dc electric field and the optical fields have to be solved at each time step, as the computations could prove to be exhaustive.

The method used here is as follows: Using a simple model to describe E_{dc} , we will initially solve for the amplitude of the writing fundamental and second-harmonic waves launched in particular modes, and then use the result to determine the $\chi^{(2)}$ grating. Once the grating is written, the power of the green light generated in the different waveguiding modes when it is read with only an

infra-red beam, also launched in a particular mode, is computed. It is assumed that the generated second-harmonic wave does not affect the $\chi^{(2)}$ grating.

We consider a germanium-doped silica planar waveguide sandwiched between two semi-infinite dielectric media, both possessing zero second-order susceptibility. The direction of propagation is taken to be in the z -direction. The optic axis is perpendicular to the direction of propagation and is taken to be in the y -direction. The wave diffracts in the unconfined x -direction and we assume that such diffraction has a fundamental Gaussian profile.

Using normal mode analysis, one can express the electric field for TM modes, $\mathbf{e}_{i,j}$, oscillating at a given frequency ω_i , i.e. $\omega_1 = \omega$ and $\omega_2 = 2\omega$, and propagating in a particular waveguiding mode j as:

$$\mathbf{e}_{i,j}(\mathbf{x}, t) = (1/2)\mathbf{E}_{i,j}(\mathbf{x})e^{-i\omega_i t} + c.c. \quad (3)$$

The spatial parts of the field components, $E_{i,j}^{(y)}$ and $E_{i,j}^{(z)}$ are given by:

$$E_{i,j}^{(y)}(\mathbf{x}) = A_{i,j}(z)\phi_{i,j}(y)\theta_{i,j}(x, z)e^{i\beta_{i,j}z} \quad (4)$$

$$E_{i,j}^{(z)}(\mathbf{x}) = A_{i,j}(z)\psi_{i,j}(y)\theta_{i,j}(x, z)e^{i\beta_{i,j}z} \quad (5)$$

where $A_{i,j}$ accounts for the modulation of the amplitude along the direction of propagation due to nonlinear interactions as well as linear losses, $\phi_{i,j}$ and $\psi_{i,j}$ describe the distribution of the y and z components of the field along the optic axis, respectively, $\theta_{i,j}$ describes the profile of these components along the unconfined x -direction at a given point z and accounts for the diffraction of the wave, and $\beta_{i,j}$ is the propagation constant. Typically, in optical planar waveguides $E^{(z)} \ll E^{(y)}$.

The field distribution in the y -direction for $E_{i,j}^{(y)}$ is given by:

$$\begin{aligned} \phi_{i,j}(y) &= B \exp \left[-\sqrt{\beta_{i,j}^2 - n_{i,1}^2 k_i^2} (y - a) \right] & y > a \\ &= C \cos \left(\sqrt{n_{i,0}^2 k_i^2 - \beta_{i,j}^2} y - \delta_i \right) & -a < y < a \\ &= D \exp \left[\sqrt{\beta_{i,j}^2 - n_{i,2}^2 k_i^2} (y + a) \right] & y < -a \end{aligned} \quad (6)$$

where the waveguide is taken to lie between $-a$ and a , $k_i = \omega_i/c$ is the free space wave number, and where $n_{i,0}$, $n_{i,1}$, and $n_{i,2}$ are the indices of refraction at frequency ω_i of the waveguide, the dielectric above the waveguide, and the dielectric below the waveguide, respectively. The coefficients

B , C , D and the phase shift δ_i are determined from the boundary conditions. The profile in the y -direction of the z component of the field, $\psi_{i,j}$, is related to $\phi_{i,j}$, by: $\psi_{i,j} = i\beta_{i,j}^{-1}\partial_y\phi_{i,j}$. The profile in the x -direction, $\theta_{i,j}$, is taken to be a fundamental Gaussian slowly varying in the z -direction, $\partial_z^2\theta_{i,j} \ll 2i\beta_{i,j}\partial_z\theta_{i,j} \ll \beta_{i,j}^2\theta_{i,j}$, and is given by:

$$\theta_{i,j}(x, z) = \frac{1}{\left[1 + (2iz/\beta_{i,j}w_{i,j}^2)\right]^{1/2}} \exp\left[\frac{-x^2}{w_{i,j}^2 + (2iz/\beta_{i,j})}\right] \quad (7)$$

where $w_{i,j}$ represents the spot size of the beam in the x -direction at $z = 0$.

The fundamental wave is treated in the undepleted pump limit. Since, the seed second-harmonic power is much smaller than that of the seed fundamental wave, self-phase modulation (SPM) dominates over cross-phase modulation (XPM). For a seed fundamental wave launched in a particular mode k , and in the limit of a slowly-varying amplitude, $(d^2A_{1,k}/dz^2) \ll 2i\beta_{1,k}(dA_{1,k}/dz) \ll \beta_{1,k}^2A_{1,k}$, coupled mode theory gives [14]:

$$2i\beta_{1,k}e^{i\beta_{1,k}z} \left[\frac{dA_{1,k}}{dz} + \frac{\alpha_1}{2}A_{1,k} \right] \int_{-\infty}^{\infty} \int_{-\infty}^{\infty} |\Phi_{1,k}(x, y, z)|^2 dx dy = -\frac{\omega^2}{\epsilon_0 c^2} \int_{-\infty}^{\infty} \int_{-\infty}^{\infty} \mathbf{P}_s(\mathbf{x}, \omega) \cdot [\Phi_{1,k}^*(x, y, z)\hat{\mathbf{y}} + \Psi_{1,k}^*(x, y, z)\hat{\mathbf{z}}] dx dy \quad (8)$$

where for brevity we use $\Phi_{1,k} = \phi_{1,k}\theta_{1,k}$ and $\Psi_{1,k} = \psi_{1,k}\theta_{1,k}$, α_1 is the power attenuation constant for the fundamental wave due to linear losses, and where $\mathbf{P}_s(\mathbf{x}, \omega)$ is the Fourier transform of the nonlinear polarization due to SPM. Coupling to other waveguiding modes through SPM is for most cases small and is ignored here. The double integral on the left hand side of the equation above is independent of z . Double integrals of this form are henceforth represented by $\kappa_{i,j}$:

$$\kappa_{i,j} = \int_{-\infty}^{\infty} \int_{-\infty}^{\infty} |\Phi_{i,j}(x, y, z)|^2 dx dy \quad (9)$$

Due to the amorphous nature of glass, the non-vanishing components of the third-order tensor $\chi_{ijkl}^{(3)}$ are of the form $\chi_{iiii}^{(3)}$ and $\chi_{iijj}^{(3)}$ including all permutations of the indices i and j . Furthermore, these non-vanishing components are related by:

$$\chi_{iijj}^{(3)} = \chi_{ijij}^{(3)} = \chi_{jiij}^{(3)} = (1/3)\chi_{iiii}^{(3)} \quad (10)$$

$$\chi_{iiii}^{(3)} = \chi_{jjjj}^{(3)} \quad (11)$$

Therefore, the polarization responsible for SPM is given by:

$$P_k^{(i)}(\mathbf{x}, \omega) = \frac{3\epsilon_0\chi_{iiii}}{4} \left(|E_{1,k}^{(i)}|^2 E_{1,k}^{(i)} + \frac{2}{3} |E_{1,k}^{(j)}|^2 E_{1,k}^{(i)} + \frac{1}{3} (E_{1,k}^{(j)})^2 (E_{1,k}^{(i)})^* \right) \quad (12)$$

The solution of Eq. (8) is then given by:

$$A_{1,k}(z) = A_{1,k}(0) \exp \left(-\frac{\alpha_1}{2} z + i\eta_1 \int_0^z f_1(z') |A_{1,k}(z')|^2 dz' \right) \quad (13)$$

$$|A_{1,k}(z)|^2 = |A_{1,k}(0)|^2 e^{-\alpha z} \quad (14)$$

where $\eta_1 = (3\omega^2)/(8c^2\kappa_{1,k}\beta_{1,k})$, and $f_1(z)$ is the overlap integral given by:

$$f_1(z) = \int_{-\infty}^{\infty} \int_{-\infty}^{\infty} \chi_{iiii}^{(3)} (|\Phi_{1,k}|^4 + |\Psi_{1,k}|^4 + (4/3)|\Phi_{1,k}|^2 |\Psi_{1,k}|^2 + (2/3)\Phi_{1,k}^2 \Psi_{1,k}^{*2}) dx dy \quad (15)$$

For the second-harmonic wave seed, SPM is much smaller than XPM. For a wave launched in a particular mode l , coupled mode theory then gives:

$$2i\beta_{2,l}\kappa_{2,l}e^{i\beta_{2,l}z} \left[\frac{dA_{2,l}}{dz} + \frac{\alpha_2}{2} A_{2,l} \right] = -\frac{4\omega^2}{\epsilon_0 c^2} \int_{-\infty}^{\infty} \int_{-\infty}^{\infty} [P_c(\mathbf{x}, 2\omega) + P_{shg}(\mathbf{x}, 2\omega)] \cdot [\Phi_{2,l}^*(x, y, z)\hat{y} + \Psi_{2,l}^*(x, y, z)\hat{z}] dy dx \quad (16)$$

where $\Phi_{2,l} = \phi_{2,l}\theta_{2,l}$ and $\Psi_{2,l} = \psi_{2,l}\theta_{2,l}$, α_2 is the power attenuation constant for the second harmonic wave due to linear losses, $P_c(\mathbf{x}, 2\omega)$ is the Fourier transform of the nonlinear polarization responsible for XPM, $P_{shg}(\mathbf{x}, 2\omega)$ is the Fourier transform of the nonlinear polarization responsible for SHG. Coupling to other waveguiding modes is small and is neglected here. Since the effect of dispersion on $\chi^{(3)}$ is small, the polarization responsible for XPM is given by:

$$P_c^{(i)}(\mathbf{x}, 2\omega) = \frac{3}{2}\epsilon_0\chi_{iiii}^{(3)} \left(|E_{1,k}^{(i)}|^2 E_{2,l}^{(i)} + \frac{1}{3} |E_{1,k}^{(j)}|^2 E_{2,l}^{(i)} \right) \quad (17)$$

For $P_{shg}(\mathbf{x}, 2\omega)$, The effective second-order susceptibility tensor $\chi_{ijk}^{(2)}$ is given by:

$$\chi_{ijk}^{(2)} = 3\chi_{ijkl}^{(3)} E_{dc}^{(l)} \quad (18)$$

where $E_{dc}^{(l)}$ is the induced static electric field. We assume here that the static electric field is effectively built up along the optic axis, i.e. the y -axis. Furthermore, we model the component of E_{dc} along y in terms of the optical fields as [15]:

$$E_{dc}^{(y)} = \frac{b}{8} \left[(E_{1,k}^{(y)})^{*2} E_{2,l}^{(y)} + r_1 (E_{1,k}^{(z)})^{*2} E_{2,l}^{(y)} + r_2 (E_{1,k}^{(y)})^* (E_{1,k}^{(z)})^* E_{2,l}^{(z)} \right] + c.c. \quad (19)$$

where b is a constant [12]; possibly a complex constant, and where r_1 and r_2 are also constants. The non-vanishing components of the induced second-order susceptibility are then $\chi_{yyy}^{(2)}$, $\chi_{yzz}^{(2)}$, $\chi_{zyz}^{(2)}$, and $\chi_{zzz}^{(2)}$. These components are related by:

$$\chi_{yzz}^{(2)} = \chi_{zyz}^{(2)} = \chi_{zzz}^{(2)} = (1/3)\chi_{yyy}^{(2)} \quad (20)$$

Strictly speaking, the asymmetric photoionization process involves a third-order conductivity tensor $\sigma_{ijkl}^{(3)}$ that has the same symmetry properties as $\chi_{ijkl}^{(3)}$ except that the Kleinman symmetry does not hold here since photoionization is believed to be a resonant process. Experimental results indicate that $\sigma_{ijji}^{(3)}/\sigma_{iiii}^{(3)} \approx 0.64$ [16]. Since from symmetry $\sigma_{ijji}^{(3)} = \sigma_{iijj}^{(3)}$, one concludes that $r_1 \approx 0.64$ and $r_2 \approx 0.36$. It should be pointed out here that a more exact treatment entails solving a time-dependent problem, with E_{dc} being obtained from the static charge distribution which is governed by the charge conservation equation.

The evolution of the complex amplitude of the second-harmonic wave along the direction of propagation is then given by:

$$\frac{dA_{2,l}}{dz} = i\eta_2 \left[\left(i \frac{\alpha_2}{2\eta_2} + 8f_2(z)|A_{1,k}(z)|^2 + bf_3(z)|A_{1,k}(z)|^4 \right) A_{2,l} + b^* f_4(z) A_{1,k}^4(z) A_{2,l}^* e^{-2i\Delta\beta z} \right] \quad (21)$$

where $\eta_2 = (3\omega^2)/(8c^2\kappa_{2,l}\beta_{2,l})$, $\Delta\beta$ is the phase mismatch given by $\Delta\beta = \beta_{2,l} - 2\beta_{1,k}$, f_2 is the overlap integral for XPM:

$$f_2(z) = \int_{-\infty}^{\infty} \int_{-\infty}^{\infty} \chi_{iiii}^{(3)} \left[(|\Phi_{1,k}|^2 + (1/3)|\Psi_{1,k}|^2) |\Phi_{2,l}|^2 + (|\Psi_{1,k}|^2 + (1/3)|\Phi_{1,k}|^2) |\Psi_{2,l}|^2 \right] dx dy$$

and where $f_3(z)$ and $f_4(z)$ are the overlap integrals for for this particular process of SHG:

$$\begin{aligned} f_3(z) = \int_{-a}^a \int_{-\infty}^{\infty} \chi_{iiii}^{(3)} \left[(|\Phi_{1,k}|^4 + (r_1 + 1/3)\Phi_{1,k}^2 \Psi_{1,k}^{*2} + (1/3)r_1 |\Psi_{1,k}|^4) |\Phi_{2,l}|^2 + ((r_2 + 2/3) \right. \\ \times |\Phi_{1,k}|^2 \Phi_{1,k}^* \Psi_{1,k} + (1/3)(2r_1 + r_2)\Phi_{1,k} |\Psi_{1,k}|^2 \Psi_{1,k}^*) \Phi_{2,l} \Psi_{2,l}^* \\ \left. + (2/3)r_2 |\Phi_{1,k}|^2 |\Psi_{1,k}|^2 |\Psi_{2,l}|^2 \right] dx dy \end{aligned}$$

$$\begin{aligned} f_4(z) = \int_{-a}^a \int_{-\infty}^{\infty} \chi_{iiii}^{(3)} \left[(\Phi_{1,k}^4 + (r_1 + 1/3)\Phi_{1,k}^2 \Psi_{1,k}^2 + (1/3)r_1 \Psi_{1,k}^4) \Phi_{2,l}^{*2} + ((r_2 + 2/3)\Phi_{1,k}^3 \Psi_{1,k} \right. \\ \left. + (1/3)(2r_1 + r_2)\Phi_{1,k} \Psi_{1,k}^3) \Phi_{2,l}^* \Psi_{2,l} + (2/3)r_2 \Phi_{1,k}^2 \Psi_{1,k}^2 \Psi_{2,l}^2 \right] dx dy \end{aligned}$$

Note that $f_2(z)$ and $f_3(z)$ are real, while $f_4(z)$ is complex. Also note that the limits of integration for the overlap integrals describing SHG, $f_3(z)$ and $f_4(z)$, are $-a$ and a as the effective $\chi^{(2)}$ grating is written inside the waveguide with the two dielectrics on the outside both possessing zero second-order susceptibility.

The equation describing the complex conjugate of the amplitude is then:

$$\frac{dA_{2,l}^*}{dz} = -i\eta_2 \left[\left(-i\frac{\alpha_2}{2\eta_2} + 8f_2(z)|A_{1,k}(z)|^2 + b^*f_3(z)|A_{1,k}(z)|^4 \right) A_{2,l}^* + bf_4^*(z)A_{1,k}^{*4}(z)A_{2,l}e^{2i\Delta\beta z} \right] \quad (22)$$

If one then uses the transformation:

$$A_{2,l}(z) = A'_{2,l}(z) \exp \left(-\frac{\alpha_2}{2}z + i\eta_2 \int_0^z [8f_2(z')|A_{1,k}(z')|^2 + bf_3(z')|A_{1,k}(z')|^4] dz' \right) \quad (23)$$

Eqs. (21) and (22) can be expressed as:

$$\frac{dA'_{2,l}}{dz} = i\eta_2 b^* f_4(z) A_{1,k}^4(z) A'_{2,l} e^{-i\zeta(z)} \quad (24)$$

$$\frac{dA_{2,l}'}{dz} = -i\eta_2 b f_4^*(z) A_{1,k}^{*4}(z) A_{2,l}' e^{i\zeta(z)} \quad (25)$$

where

$$\zeta(z) = 2 \left(\Delta\beta z + \eta_2 \int_0^z [8|A_{1,k}(z')|^2 f_2(z') + bf_3(z')|A_{1,k}(z')|^4] dz' \right)$$

Eqs. (24) and (25) can be readily decoupled to obtain:

$$\frac{d^2 A'_{2,l}}{dz^2} + \left(i\frac{d\zeta}{dz} - \frac{(df_4/dz)}{f_4} - 4\frac{(dA_{1,k}/dz)}{A_{1,k}} \right) \frac{dA'_{2,l}}{dz} - \eta_2^2 |b|^2 |f_4|^2 |A_{1,k}|^8 A'_{2,l} = 0 \quad (26)$$

The solution to Eq. (26) is then used along with Eqs. (13), (18), and (19) to determine the written $\chi^{(2)}$ grating. We note that the general solution to Eq. (26) allows for some film generated second harmonic during the writing process, and the equations used to determine the $\chi^{(2)}$ grating take this into account. However, if b is real and $b|A_{1,k}|^4$ is sufficiently small, the seed second harmonic wave undergoes a phase shift but no growth along the direction of propagation. Neglecting self- and cross-phase modulation, and linear losses, one can readily show in the plane wave limit that this holds true for $(\omega\chi^{(3)}b|A|^4)/c \ll \Delta k$, where Δk is the wavenumber mismatch.

The grating is then read with only a fundamental wave propagating in a particular mode m . The spatial parts of the field components for the generated green are expressed as:

$$E_2^{(y)}(\mathbf{x}) = \sum_j A_{2,j} \phi_{2,j}(y) \theta_{2,j}(x, z) e^{i\beta_{2,j}z} \quad (27)$$

$$E_2^{(z)}(\mathbf{x}) = \sum_j A_{2,j} \psi_{2,j}(y) \theta_{2,j}(x, z) e^{i\beta_{2,j}z} \quad (28)$$

where we sum over all possible green waveguiding modes. Applying normal mode analysis again, one can obtain the equations describing the complex amplitudes of the reading fundamental wave and the generated second harmonic. We neglect the pump wave depletion due to SHG. This is justified since the maximum conversion rate is on the order of a fraction of one percent. The amplitude for the reading fundamental wave is described by an equation similar to Eq. (13), with the overlap integral involving the waveguiding mode m . For the generated second harmonic propagating, for example, in mode n , the evolution of the complex amplitude along the direction of propagation is given by:

$$\frac{dA_{2,n}}{dz} = i\eta_3 \left[\left(\frac{i\alpha_2}{2\eta_3} + |A_{1,m}(z)|^2 f_2'(z) \right) A_{2,n} + (1/3) f_5(z) A_{1,m}^2 e^{-i(\beta_{2,n} - 2\beta_{1,m})z} \right] \quad (29)$$

where $\eta_3 = (3\omega^2)/(c^2\kappa_{2,n}\beta_{2,n})$, $f_2'(z)$ has the same form as $f_2(z)$ except that it involves mode m for the fundamental wave and mode n for the second harmonic, and where the overlap integral $f_5(z)$ is given by:

$$f_5(z) = \int_{-a}^a \int_{-\infty}^{\infty} \chi_{yyy}^{(2)} \left(\Phi_{1,m}^2 \Phi_{2,n}^* + (1/3) \Psi_{1,m}^2 \Phi_{2,n}^* + (2/3) \Phi_{1,m} \Psi_{1,m} \Psi_{2,n}^* \right) dx dy$$

Using the initial condition $A_{2,n} = 0$ at $z = 0$, one can readily obtain the solution to Eq. (29):

$$A_{2,n} = (i\eta_3/3) e^{-\xi(z)} \int_0^z f_5(z') A_{1,m}^2(z') \exp \left[\xi(z') - i(\beta_{2,n} - 2\beta_{1,m})z' \right] dz' \quad (30)$$

where $\xi(z)$ is given by:

$$\xi(z) = \frac{\alpha_2}{2} z - i\eta_3 \int_0^z f_2'(z') |A_{1,m}(z')|^2 dz'$$

Results of the numerical simulation are presented in the next section.

3 Results

The problem is simulated numerically by launching an infra-red fundamental beam along with a green second harmonic beam in a 3 cm long, 2 μm deep, germanium-doped waveguide sandwiched between silica on one side and air on the other side. The indices of refraction for the fundamental wave for the waveguide, silica and air are 1.532, 1.4496, and 1.0, respectively. The corresponding

indices of refraction for the second-harmonic are 1.546, 1.4607 and 1.0. Linear losses for the infra-red wave and its second harmonic are taken to be 0.5 dB/cm and 1.0 dB/cm, respectively. For all beams, reading, writing and generated, the spot size is taken to be $30\mu m$. Except where noted, both the power of the infra-red writing beam and the power of the green writing beam are kept constant, with the power of the reading infra-red beam set equal to that of the infra-red writing beam (20 KW peak power). The power of the green writing beam is taken to be three orders of magnitude less than that of the infra-red beam. For a given mode oscillating at a particular frequency, the power is given by:

$$P_{i,j} = (1/4) \int_{-\infty}^{\infty} \int_{-\infty}^{\infty} \mathbf{E}_{i,j} \times \mathbf{H}_{i,j}^* dx dy + c.c. \quad (31)$$

The constant b in Eq. (19) is assumed to be real and its value is adjusted to provide a maximum E_{dc} of about $10^7 V/m$ inside the waveguide.

We launch both infra-red and green seeds into the waveguide in several different waveguiding TM modes and compare the results of the different cases. The coupled equations (24) and (25) are then integrated using a fourth-order Runge-Kutta method. This is more numerically accurate than solving the second-order differential equation (26). For the parameters used in our simulations, the SHG polarization leads to a phase shift in the second harmonic seed (see the discussion below Eq. 26). The resulting $\chi^{(2)}$ grating is then used during the reading process. Different TM modes are also used during the reading process. The amplitude of the generated green is given by Eq. (30) and is computed for all possible waveguiding modes.

In all numerical simulations, a relatively significant amount of SHG is obtained when both the reading and writing infra-red beams are launched in the same TM mode. Furthermore, the generated green is found to propagate mainly in the same mode as the seed green. All other combinations generate a few orders of magnitude less power with a rapidly varying \sin^2 length dependence. As an example, Figure (1a) shows the growth of the second-harmonic power generated in the TM_0 mode as a function of distance along the direction of propagation, z , for the case of a waveguide seeded by infra-red and green beams, both launched in the TM_0 mode, and read with an infra-red beam also launched in the TM_0 mode. Note that due to linear losses and diffraction, the power generated is not quadratic in length but rather reaches a maximum value and then falls off as the SHG power obtained from the decreasing $\chi^{(2)}$ grating becomes less than the linear loss. If there

are no linear losses, the power then saturates due to diffraction. This case is shown in Figure (1b). It should be pointed out that the SHG power actually fluctuates very slightly with a periodicity of about $10.5\mu m$. This is the quasi-phase matching period for this combination of infra-red and green light modes. These observations can be explained by the phase-matching condition required for efficient SHG. In the cases in which relatively poor SHG is obtained, the phase-mismatch between the reading infra-red and the generated green is not cancelled out by the phase variation of the effective second-order susceptibility $\chi^{(2)}$ induced during the reading process. It should be pointed out, however, that it is possible for a waveguide with a different thickness and/or different indices of refraction for the waveguide and dielectrics to satisfy the phase-matching condition even though the infra-red reading beam and the dominant mode in which the generated green propagates do not correspond to the modes of the seed infra-red and green beams. Of course, in this case, the overlap between the $\chi^{(2)}$ grating, the fundamental reading wave, and the generated second-harmonic wave is not as favorable.

A result that is different than conventional SHG is that the combination of different modes of infra-red and green seed gave the same order of magnitude of SHG power as long as the infra-red used during the reading process is in the same TM mode as the writing mode even though the higher order modes are not as confined to the waveguide, where the SHG occurs, as the lowest order mode. For example, when we combined a TM_1 for the seed infra-red with a TM_1 mode for the seed green and read that with a TM_1 infra-red, the same order of magnitude of SHG was obtained as that of the case when all beams are in TM_0 . This is in agreement with experimental results [17]. Figure (2) shows the growth of the SHG power in the TM_1 mode, the dominant mode for this case, as a function of distance along the direction of propagation. The SHG power for this case is about 0.4 of that when all beams are in the lowest order mode.

Table (1) compares the SHG for various waveguiding modes normalized to the case in which both the infra-red and green are launched in the TM_0 mode. Note that, for an infra-red beam launched in a given mode, the maximum SHG obtained is when the green seed is launched in the same mode.

The results obtained in the table above can be explained by noting that for this particular process of SHG, and with the reading and writing infra-red beams in the same mode, the overlap

integral has the same form as $f_3(z)$ given in Eq. (21). The first term in the integrand is the dominant term and it involves a multiple of even powers of the infra-red and green modes. Therefore, unlike other SHG processes, there is no cancellation in the overlap integrals when different modes are used, and thus these integrals are comparable in value. Still the best overlap occurs when both the infra-red and green are in the same mode as the modes will almost match each other. Figures (3a) and (3b) show plots, properly normalized, of the integrand vs. depth in waveguide for two different combinations of modes, with $y = -1\mu m$ representing the waveguide-silica substrate interface, and $y = 1\mu m$ representing the waveguide-air interface. The area underneath each of the plots represents the overlap in y .

We also note that as long as the infra-red power used during the reading process is the same as that during the writing process, the effects of SPM and XPM are insignificant. If the intensities are considerably different, however, the efficiency is decreased. This can be attributed to that different intensities produce different SPM and XPM and the net effect in the phase mismatch is nonvanishing and builds up along the direction of propagation. To illustrate this, SPM and XPM were turned off during the reading process and the results were compared to the case when both SPM and XPM are included. Thus the case when the grating is written under high intensity but read with a much weaker beam is modeled. Figure (4) shows a plot of SHG power vs. distance along the direction of propagation for both cases.

4 Conclusion

We have formulated the problem of SHG in germanium-doped planar waveguides that possess an effective second-order susceptibility induced by seeding. This formalism is based on a normal mode analysis that includes the effects of self- and cross-phase modulation of the fundamental and its second-harmonic. The resultant equations describing the amplitude evolution of the second-harmonic were solved for various combinations of waveguiding modes. Unlike the traditional means of producing SHG, we note that considerable power is generated in the higher order modes. The conversion efficiency is limited by diffraction.

5 Acknowledgement

This work was performed while the author held a National Research Council-FJSRL Research Associateship.

References

- [1] U. Osterberg and W. Margulis, *Opt. Lett.*, **11**, 516 (1986).
- [2] R. H. Stolen and H. K. Tom, *Opt. Lett.*, **12**, 585 (1987).
- [3] J. J. Kester, P. J. Wolf, and W. R. White, *Opt. Lett.*, **17**, 1781 (1992).
- [4] A. Kamal, D. A. Weinberger, and W. H. Weber, *Opt. Lett.*, **15**, 613 (1990).
- [5] R. L. MacDonald and N. M. Lawandy, *Opt. lett*, **18**, 595 (1993).
- [6] V. Dominic and J. Feinberg, *Phys. Rev. Lett.*, **71**, 3446 (1993).
- [7] V. Mizrahi, U. Osterberg, J. E. Sipe, and G. I. Stegeman *Ipt. Lett.*, **13**, 279 (1988).
- [8] V. Mizrahi, U. Osterberg, C. Krautschik, G. I. Stegeman, J. E. Sipe and T. F. Morse, *Appl. Phys. Lett.*, **53**, 557 (1988).
- [9] P. Weitzmann, J. J. Kester, and U. Osterberg, *Electron. Lett.*, **30**, 697 (1994).
- [10] M. L. Brauer, I. Dajani, and J. J. Kester, *Electron. Lett.*, **30**, 297 (1994).
- [11] B. Ya. Zel'dovich and A. N. Chudinov, *JETP Lett.*, **50**, 439 (1989).
- [12] E. M. Dianov, P. G. Kazansky, and D. Yu. Stepanov, *Sov. J. Quantum Electron.*, **19**, 575 (1990).
- [13] D. Z. Anderson, V. Mizrahi, and J. E. Sipe, *Opt. Lett.*, **16**, 796 (1991).
- [14] D. Marcuse, *Theory of Dielectric Waveguides*, (Academic, New York, 1974).
- [15] M. L. Brauer and I. Dajani, *J. Appl. Phys.*, accepted for publication.
- [16] V. Dominic, *Ph.D Thesis*, (University of Southern California, 1993).
- [17] J. J. Kester, I. Dajani, U. Osterberg, and P. Weitzmann, *Conference on Lasers and Electro-Optics*, **8**, 90 (1994).

6 List of Captions for Figures

Figure (1) SHG Power in TM_0 vs. distance along z for a grating written with both fundamental and second-harmonic in TM_0 mode and read with fundamental in TM_0 mode a) linear losses included b) zero linear losses.

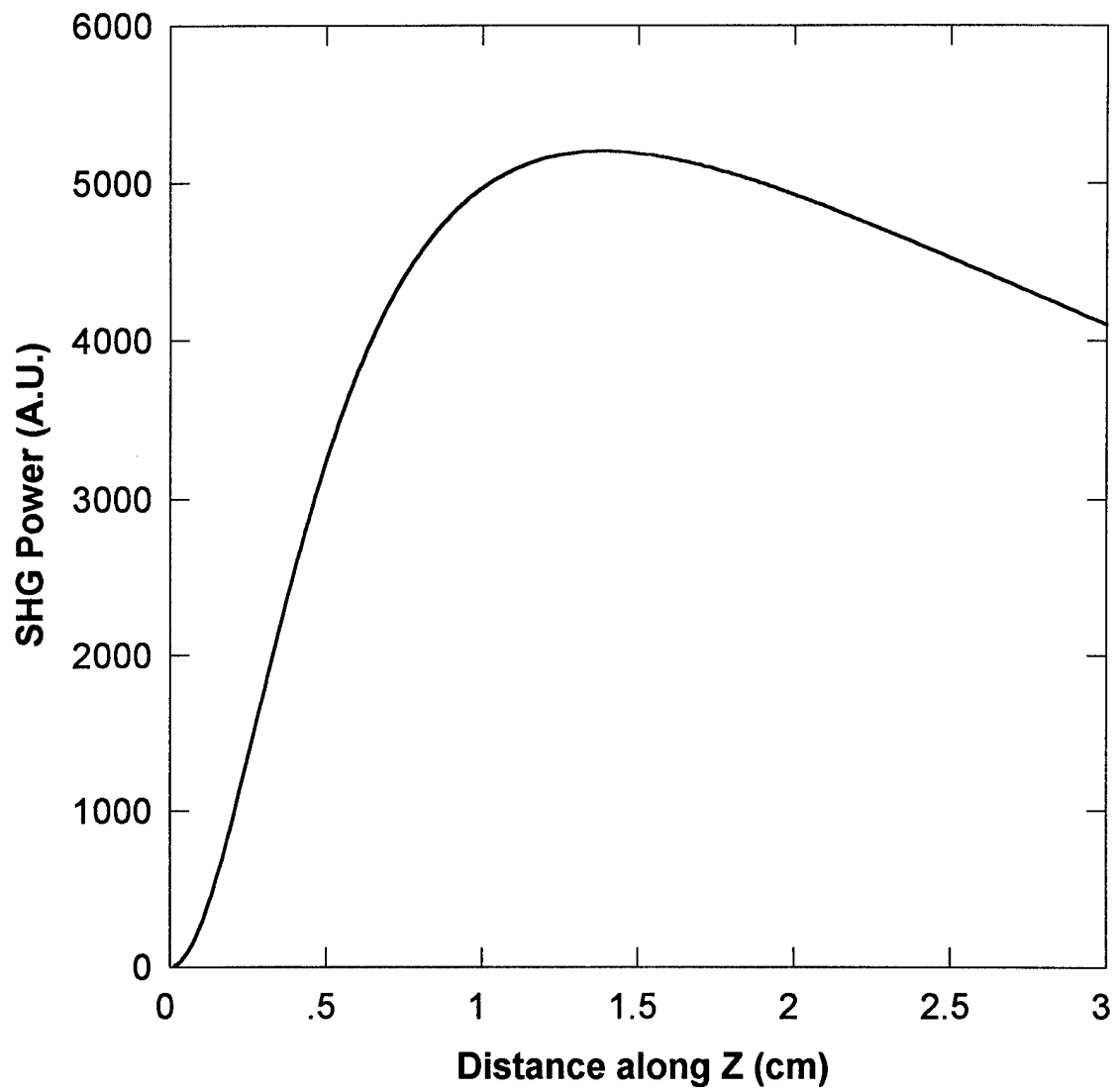
Figure (2) SHG Power in TM_1 vs. distance along z for a grating written with both fundamental and second-harmonic in TM_1 mode and read with fundamental in TM_1 mode.

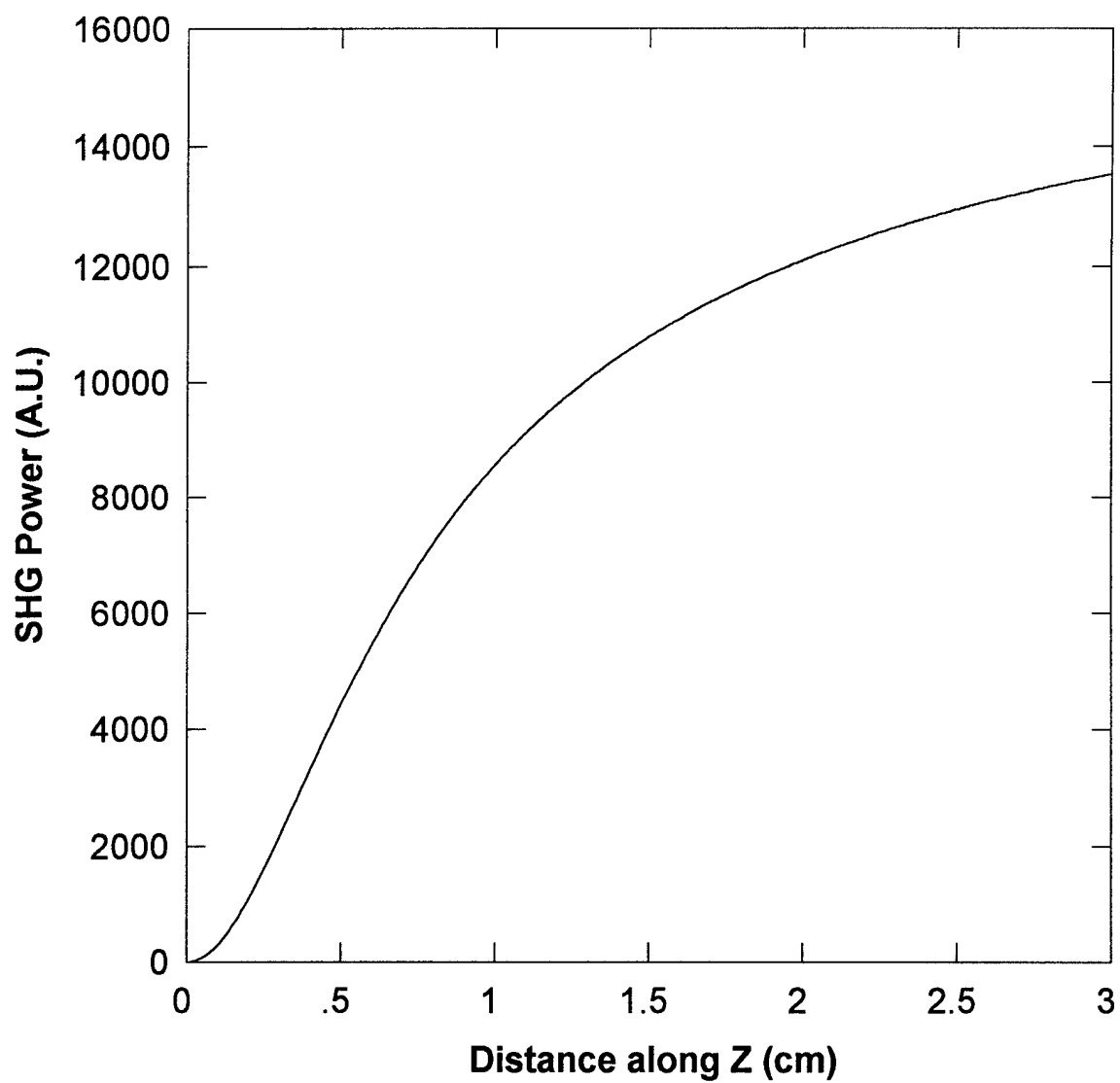
Figure (3) Overlap vs. waveguide depth for a) infra-red and green in TM_0 b) infra-red in TM_0 and green in TM_2 .

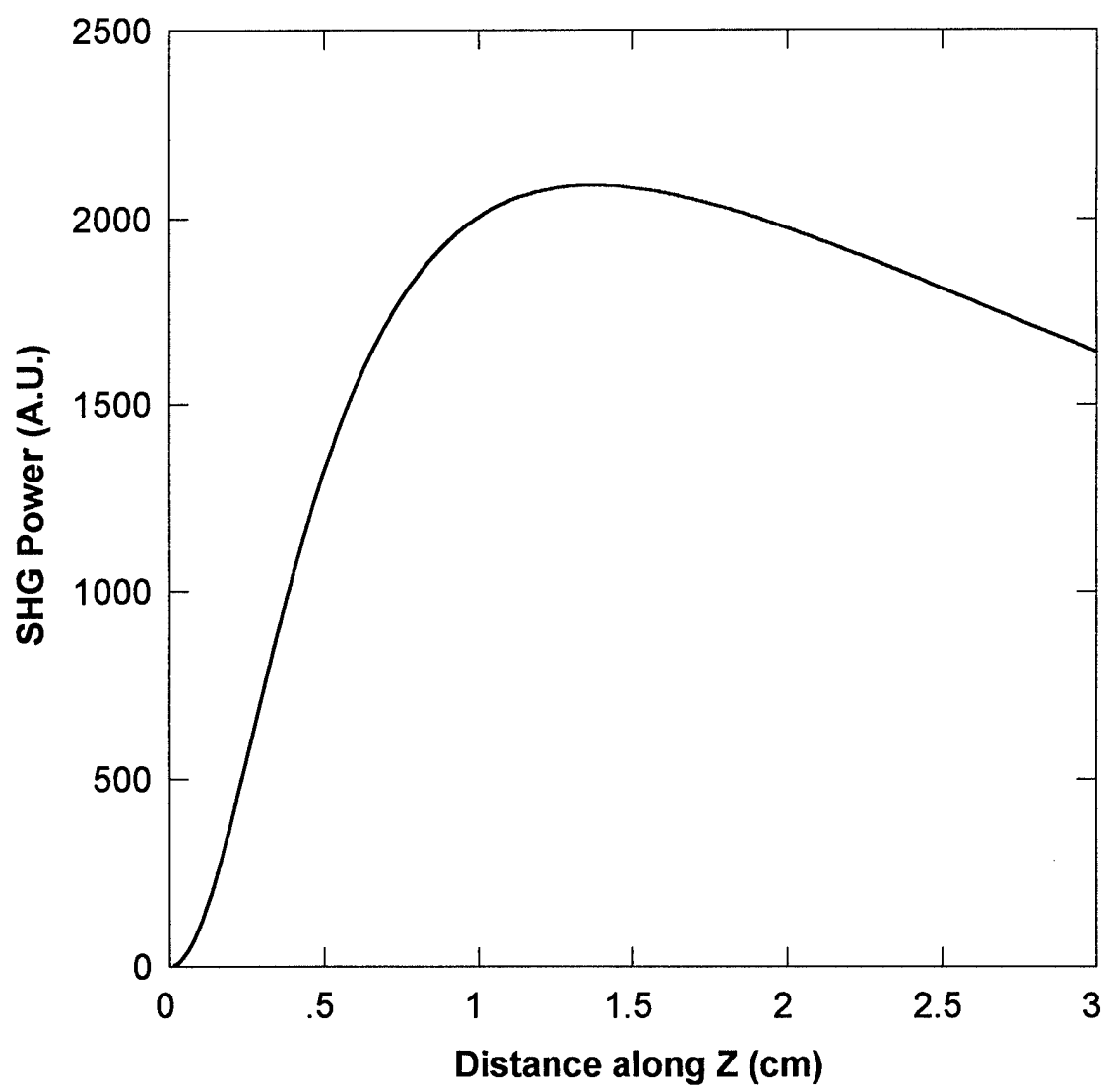
Figure (4): SHG power vs. distance along z showing effect of SPM and XPM.

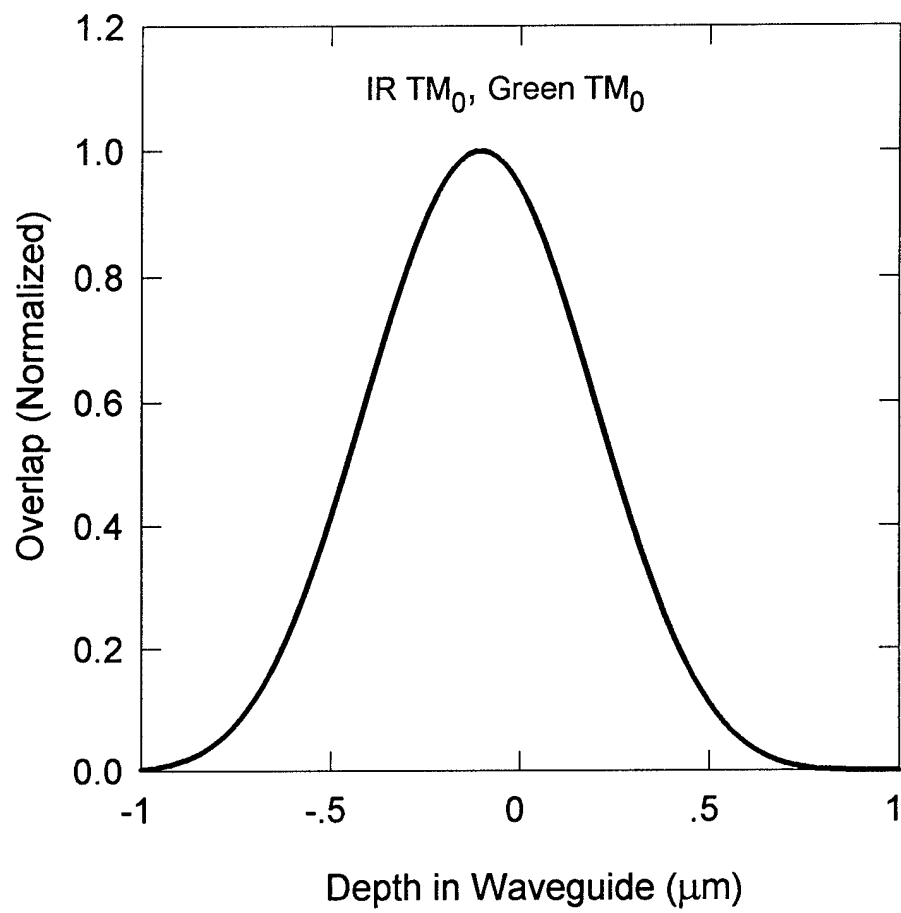
Fundamental Mode	Second Harmonic	Normalized Power
TM0	TM0	1.00
TM0	TM1	0.30
TM0	TM2	0.36
TM1	TM0	0.13
TM1	TM1	0.40
TM1	TM2	0.21

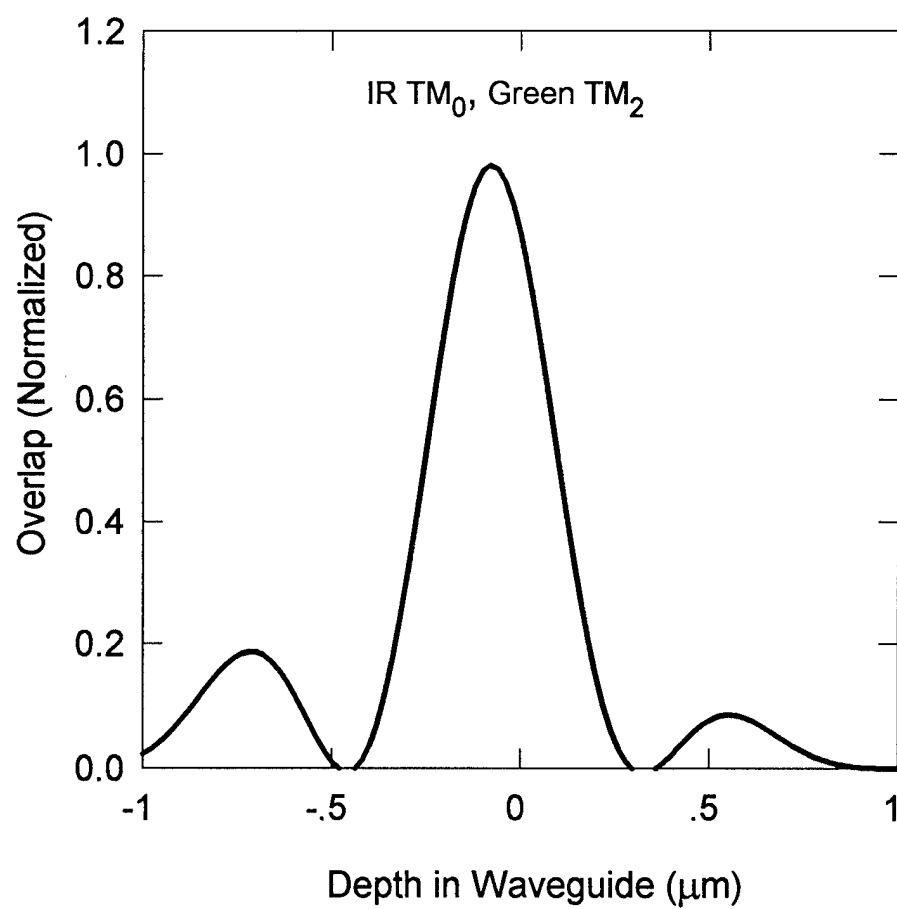
Table 1: SHG power for some of the different infra-red and green mode combinations normalized to the case in which all beams are in the lowest order mode.

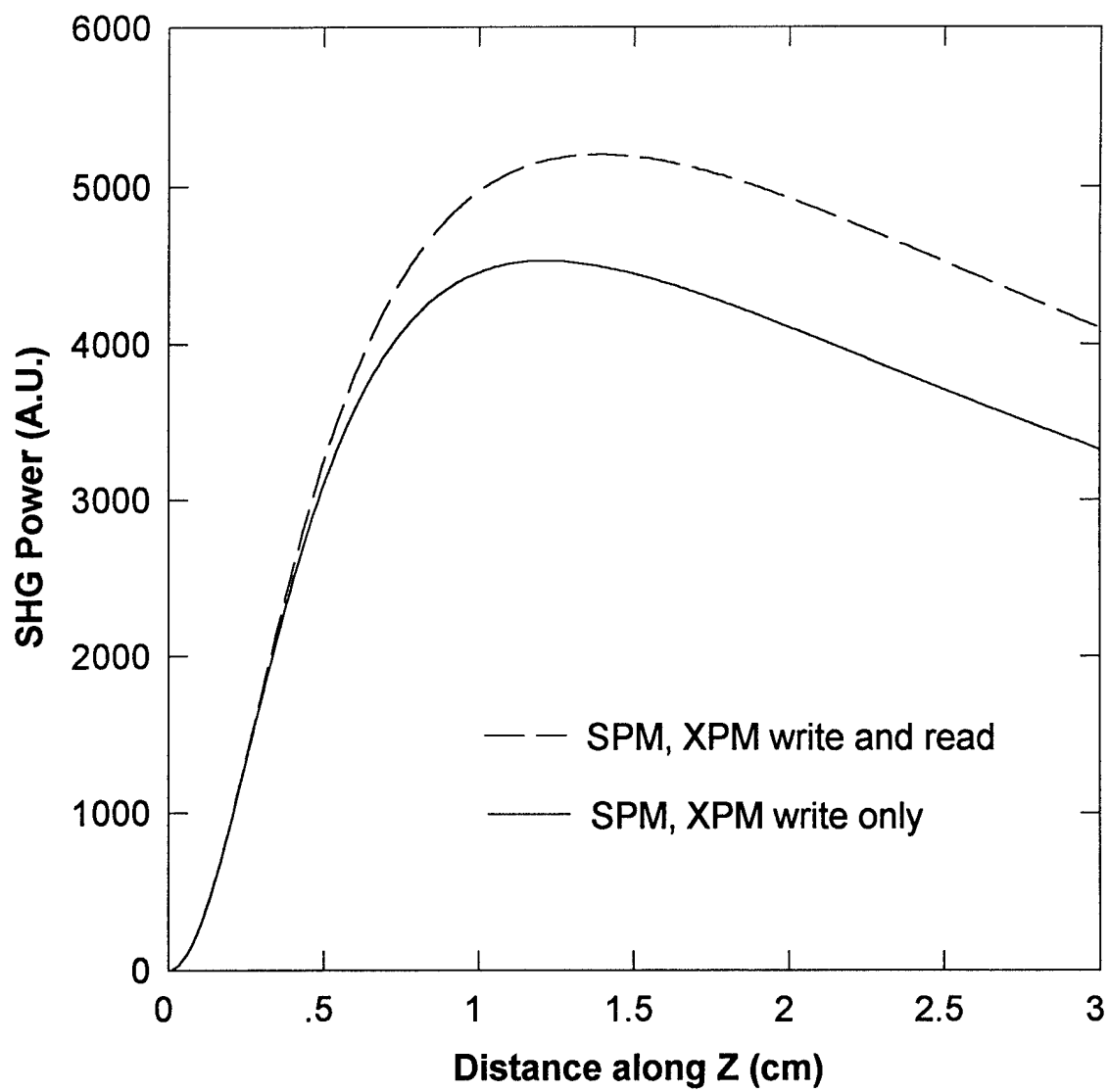












**Effect of pre-annealing on the level of second harmonic generation and defect sites achieved in poled
fused silica**

Leanne J. Henry and Alan D. DeVilbiss

Frank J. Seiler Research Laboratory

US Air Force Academy, Colorado 80840-6272

Tsung E. Tsai

Virginia Polytechnic Institute, Blacksburg, VA 24061

The level of second harmonic generation (SHG) in poled fused silica was altered by pre-annealing in aqueous and dry nitrogen atmospheres. The effect of water and heat was found to be dependent upon the lot of material. The effect on the SHG of either a wet or dry pre-anneal was sometimes found to be reversible by performing the opposite pre-annealing process. For both wet and dry pre-annealed samples, the SHG was found to have both near-surface ($<25\mu\text{m}$) and bulk components ($\approx 1.5\text{mm}$). Electron paramagnetic resonance (EPR) data reveals the presence of Si and Ge E' defect sites and shows that the relative concentrations of these sites are altered by the pre-annealing processes. EPR, along with SHG data, provide evidence for a second-order "bond effect" along with a third-order "hole filling effect" as sources of the nonlinearity.

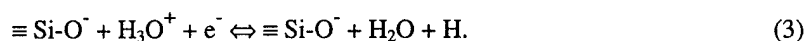
1. INTRODUCTION

Second harmonic generation (SHG) in poled fused silica, which was first reported by Myers, Mukherjee and Brueck⁽¹⁾ in 1991, has increased in importance because of a multitude of potential device applications. Such applications include electro-optic switching, frequency doubling crystals, parametric amplification, parametric oscillation, and linear electro-optic modulation/frequency conversion which can be monolithically integrated into optical fibers and planar integrated circuit geometry's. Because of these potential applications, much work has been done to understand the phenomenon of SHG in poled fused silica.

In Myers original paper on the SHG in poled fused silica⁽¹⁾, an optically active layer of thickness 5-10 μm on the positively biased face of the sample was reported. In addition, the nonlinear optical coefficient, d_{33} , was found to be on the order of 1 pm/V in poled natural fused quartz. But for higher purity UV grade synthetic fused silica having only 10 percent as many impurities as natural fused quartz, the magnitude of d_{33} was found to be an order of magnitude lower. Based on this data, Myers felt that the SHG originated from a space charge region created by migrating impurity ions and electrons. Mukherjee, et al.⁽²⁾, further proposed that the electrons were trapped in non-bridging oxygen hole centers associated with silicon which aligned upon poling.

In a later paper, Nasu et al.⁽³⁾, reported a direct dependence of the SHG on the hydroxyl content in SiO_2 glasses prepared by different methods. Nasu also reported second-order nonlinear susceptibilities on the order of .05 pm/V in addition to well-developed fringes in Maker-SHG scans of poled sol-gel derived fused silica. Based on the number and angular positions of the fringes along with the indices of refraction for 1.06 μm and 532 nm radiation in fused silica, the interaction layer was found to be the same thickness as the sample thickness. Finally, Kazansky, et al.⁽⁴⁾ reported the erasure of SHG in fused silica by electron-beam irradiation and speculated that this effect may be the result of electrons neutralizing positive charges resulting in the elimination of the space charge region. Kazansky also found the optically active region to reside from 12 to 19 μm s below the positively biased surface, in contradiction to that reported by Myers⁽¹⁾. Because the poling process involves a charging phenomenon, work by Lai, et al.⁽⁵⁾, Nicollian, et al.^(6,7), and Olthuis, et al.⁽⁸⁾ on the role of water in the charging of fused silica is also relevant. By dry annealing SiO_2 in

N₂ for 1 hour at 1000°C, Lai found that the number of electron traps were reduced nearly fourfold. Lai speculated that these traps were associated with water-related centers. Along the same lines, Nicollian reported that the ability to charge SiO₂ by avalanche injection was dependent upon the presence of water in the material. Nicollian also found a one-to-one relationship between the level of electron charging and the amount of hydrogen evolving from the material. Based on this data, Nicollian speculated the electron trapping center to be the non-bridging oxygen hole center (NBOHC). Finally, Olthuis, also having observed hydrogen evolution upon charging of SiO₂, proposed the following mechanism.



Currently, the mechanism for second harmonic generation in poled fused silica and its relationship to defect sites is not well understood. We will show that the level of second harmonic generation along with the relative concentrations of Si and Ge E' defect sites can be altered by wet and dry pre-annealing fused silica over a range of temperatures. In addition, we will present a model for the SHG in poled fused silica and show experimental evidence in support of this model.

2. EXPERIMENTAL METHODS

Manipulation of the level of SHG and defect sites in fused silica was accomplished by pre-annealing the material in an aqueous or dry nitrogen environment at temperatures up to 900°C. Infrared grade commercial fused silica having low water content was used for all of the experiments described in this paper. To determine the effect on the SHG of pre-annealing under different conditions, the nonlinear optical coefficient, d_{33} , of the pre-annealed material after poling was compared with d_{33} of the poled untouched, i.e., *as received*, material. To correlate the level of SHG with specific paramagnetic defect sites in fused silica, EPR was carried out on the pre-annealed materials.

A total of thirty six *as received* samples, each 1.59 mm thick and 25 mm in diameter, was used for the pre-anneals. Three *as received* samples, one each from lots 1, 2 and 3 for the wet pre-anneals and from lots 2, 3 and 4 for the dry pre-anneals, were used at each individual pre-annealing temperature. Each sample underwent only one pre-annealing process, either wet or dry, and was never reused for a second pre-anneal. A "lot" of material was considered to be a group of samples received from the manufacturer at one time. Such groups of samples were generally purchased months apart.

The *as received* samples were initially parallel-plate poled to generate the nonlinear optical effect. The poling process involved heating a sample in an oven from room temperature to 250°C with 7000 V applied across the plates. This typically took 1/2 hour. Following this, the sample was maintained at 250°C for 1 hour after which it was cooled to room temperature with the voltage still applied.

The baseline SHG susceptibility of the poled sample was obtained using the Maker-Fringe technique⁽⁹⁾. The experimental setup for this is shown in Figure 1. 1.06 μm radiation from a Q-switched Nd/YAG laser, which was passed through a RG695 filter to remove visible radiation as well as attenuation filters to reduce the beam power to approximately 10 mW, was focused on each sample individually to maximize the second harmonic signal. Upon irradiation of the sample with 1.06 μm radiation, the resultant frequency doubled radiation and residual 1.06 μm radiation passed through a BG18 filter and a 530 nm bandpass filter for removal of the 1.06 μm component before detection by the photomultiplier tube. Typically, 3000 Q-switched pulses were averaged by the boxcar averager and recorded in the form of a dc voltage by a computer.

To generate the Maker-Fringe pattern, the sample was rotated about an axis perpendicular to the p-polarized laser beam through the angular range $-80^\circ \leq \theta \leq +80^\circ$ in one degree steps. The resulting Maker-Fringe pattern, Figures 2 and 3, is the result of a phase mismatch, Δk , between the fundamental and second harmonic waves, equation 4:

$$\Delta k = (4\pi/\lambda)(n_\omega \cos \theta_\omega' - n_{2\omega} \cos \theta_{2\omega}') \quad (4)$$

where n_ω and $n_{2\omega}$ are the indices of refraction and θ_ω' and $\theta_{2\omega}'$ are the angles of refraction for the fundamental and second harmonic waves, respectively, and λ is the wavelength of the fundamental beam.

Theoretically, the power in the second harmonic is of the form: $P_{2\omega} = f(\theta)d^2\sin^2\Psi(L,\theta)$ where θ is the rotation angle as indicated in Figure 1, d is the nonlinear optical coefficient and L is the interaction length.⁽⁹⁾ Generally, $f(\theta)d^2$ forms the envelope describing the low-frequency structure associated with the Maker-Fringe curve while $\sin^2\Psi(L,\theta)$ creates the oscillations. In addition, the envelope, $f(\theta)d^2$, is independent of the phase mismatch, equation 4. Because a sample of poled fused silica exhibits uniaxial or $C_{\infty v}$ symmetry, the nonlinear polarization, P_{NL} , is of the following form:

$$P_{NL} = \begin{pmatrix} 0 & 0 & 0 & 0 & d_{31} & 0 \\ 0 & 0 & 0 & d_{31} & 0 & 0 \\ d_{31} & d_{31} & d_{33} & 0 & 0 & 0 \end{pmatrix} \begin{pmatrix} E_1^2 \\ E_2^2 \\ E_3^2 \\ 2E_2E_3 \\ 2E_1E_3 \\ 2E_1E_2 \end{pmatrix} \quad (5)$$

Since p-polarized radiation was used (i.e. $E_1 = E\cos\theta_\omega'$, $E_2 = 0$, $E_3 = E\sin\theta_\omega'$), and $d_{31} = 1/3 d_{33}$ for fused silica⁽¹⁰⁾, a nonlinear polarization proportional to d_{33} was obtained:

$$P_{NL} = E^2 d_{33} \begin{pmatrix} 2/3 \sin\theta_\omega' \cos\theta_\omega' \\ 0 \\ 1/3 \cos^2\theta_\omega' + \sin^2\theta_\omega' \end{pmatrix} \quad (6)$$

Because $P_{2\omega}$ is proportional to $|P_{NL}|^2$, the nonlinear optical coefficient, d_{33} was evaluated. To get an absolute value for d_{33} , a y-cut quartz standard was used as a reference. d_{33} was then computed from the following equation

$$d_{33} = d_{11,y} \left(\frac{P_{2\omega,s}''}{P_{2\omega,y}''} \frac{f_y(\theta_y)}{f_s(\theta_s)} \frac{\sin^2 \Psi_y}{\sin^2 \Psi_s} \right)^{1/2} \quad (7)$$

where the subscripts s and y represent the sample and y-cut quartz standard, respectively, and $d_{11,y}$ represents the nonlinear optical coefficient associated with y-cut quartz. Since an interaction length could not be obtained from the Maker-Fringe scans in the absence of fringes, calculations of d_{33} were based on an

interaction length equivalent to the coherence length. As a result, the values of d_{33} reported represent the lower bound. Finally, standard deviations associated with variations in the sample surfaces for the values of d_{33} reported were estimated from measurements to be on the order of ± 10 percent. Since a lower bound of d_{33} is reported, the actual errors associated with the values of d_{33} reported are almost certainly greater than ± 10 percent

After the SHG measurement, the sample was placed between grounded parallel plates for depoling to remove the nonlinear effect. As the plates were brought into close proximity to the sample, an image charge developed on the plates in proportion to the level of polarization in the sample. As the sample was heated to 250°C and the depoling process proceeded, the polarization of the sample was eliminated and the amount of image charge on the plates decreased in proportion. This loss of image charge was recorded as a function of time.

After the sample was depoled, it was either wet or dry pre-annealed in a one-zone tube furnace. The initial stage of the pre-annealing process involved centering the sample in the tube furnace and allowing nitrogen to purge the system of atmospheric gases for 20 minutes. The temperature was then increased to the specified pre-annealing temperature between 400°C to 900°C for 1.5 hours. Upon completion of the pre-annealing process, the sample was allowed to cool, within the tube furnace, to room temperature. The only difference between the wet and dry pre-annealing processes was that dry pre-annealing involved direct entry of nitrogen into the tube furnace whereas wet pre-annealing involved bubbling nitrogen through water at approximately 75°C before entry into the tube furnace.

Once the sample had been pre-annealed, it was repoled and the SHG was recorded again using a Maker-SHG scan. To determine the extent of the polarization within the sample, the sample was again depoled.

FTIR spectra of both the *as received* and pre-annealed samples were obtained with a Nicolet 510P FT-IR spectrometer in reflectance mode between 400 cm^{-1} to 4800 cm^{-1} . 1064 scans were averaged in order to reduce the noise level and allow quantitative comparison of spectra from different pre-annealing temperatures. EPR spectra were obtained at room temperature on a Bruker ESP-300 X-band spectrometer using the out-of-phase high power second harmonic mode technique.⁽¹¹⁾ The EPR parameters utilized are listed in Table 1 below.

3. RESULTS

A. EFFECT OF PRE-ANNEALING ON THE LEVEL OF SHG

The ability to alter the level of d_{33} in a sample of fused silica by wet or dry pre-annealing was found to be highly dependent on the particular lot of material. Pre-annealing data for four lots of fused silica are shown in Figures 4 and 5. Samples from lots 2 and 3 have been both wet and dry pre-annealed whereas samples from lot 1 were only wet pre-annealed and samples from lot 4 were only dry pre-annealed. From variation of d_{33} across the sample surface and variation in d_{33} among samples from the same lot of material (typically 10 percent), errors associated the percentage changes in d_{33} shown in Figures 4 and 5 are estimated to be on the order of ± 12 to ± 16 percent. These errors are shown by a few representative error bars in the figures. It must be pointed out that although the variation of d_{33} among samples from the same lot is approximately 10 percent, the variation between samples from different lots can be much more.

For wet pre-annealing, shown in Figure 4, the nonlinearity was decreased for all lots of material studied over the temperature range of pre-anneal investigated with the possible exception of lot 3 in the temperature range around 600°C. In addition, the decrease in d_{33} was greater the further the pre-annealing occurred from the 500-600°C temperature range. Unlike lots 1 and 2 which retained a sizable d_{33} when pre-annealed at temperatures greater than 600°C, the SHG associated with lot 3 was virtually quenched at higher pre-annealing temperatures.

While the trends for wet pre-annealing were somewhat similar for all lots of fused silica studied, the trends for dry pre-annealing were not. Samples from lots 2 and 4, when dry pre-annealed, shown in Figure 5, exhibited linear behavior in the percentage change in d_{33} as a function of temperature. When dry pre-annealed, the behavior of samples from lot 2 was quite distinct from the behavior when wet pre-annealed. On the other hand, the behavior of samples from lot 3 when dry pre-annealed was very similar to the behavior when wet pre-annealed. Apparently the presence of water was able to significantly affect the defect sites generating second harmonic in lot 2 whereas in lot 3, it was not. As is apparent from the figures, depending on the temperature range studied and the lot of fused silica, an increase or decrease in d_{33} may occur by both wet and dry pre-annealing. Finally, the more extreme changes in d_{33} brought about by

pre-annealing are typically much greater than the individual deviations in d_{33} observed between *as received* samples from different lots.

The increase or decrease of d_{33} brought about by either wet or dry pre-annealing has been found to be reversible to a certain extent upon performance of the opposite pre-annealing process. As an example, a sample of fused silica having a d_{33} of .34 pm/V after the initial poling, obtained a d_{33} of .16 pm/V upon dry pre-annealing in N_2 for 1 hour at 550°C. Upon subsequent wet pre-annealing under the same conditions, a d_{33} of .35 pm/V, which was nearly equal to the initial *as received* level, was obtained. In summary, the d_{33} after being decreased over 50 percent by a dry pre-anneal, was reestablished to its initial level upon wet pre-annealing. The fact that the presence of water was the only difference between the two pre-annealing processes supports the idea that water is a component in an equilibrium process between a defect site in its optically active and inactive configurations. The same reversibility was also seen when d_{33} was initially increased by wet pre-annealing and then decreased by a subsequent dry pre-anneal. As an example, a sample of fused silica having an initial d_{33} of .32 pm/V, obtained a d_{33} of .39 pm/V when wet pre-annealed for 1 hour at 550°C, a 21 percent increase. Upon subsequent dry pre-annealing under the same conditions, the d_{33} was decreased to .12 pm/V, a decrease of 69 percent.

Although d_{33} was fully reversible for some lots of fused silica, for other lots of material, d_{33} was only partially reversible. As an example, a sample of fused silica having an initial d_{33} of .32 pm/V, obtained a d_{33} of .19 pm/V when wet pre-annealed, a 40 percent decrease. When the sample was subsequently dry pre-annealed, the d_{33} was only increased to .20 pm/V, a 6 percent increase. Apparently an irreversible change of some sort occurred. According to Lee⁽¹²⁾, fused silica contains both permanent hydroxide which is formed in the material during manufacture and metastable hydroxide which is formed upon reaction of fused silica with water vapor. According to both Lee⁽¹²⁾ and Shelby⁽¹³⁾, metastable hydroxide which has been added to a material may not be totally removable. This argument coupled with evidence to be presented later on the role of hydroxide in the generation of second harmonic may explain the nonreversibility of the pre-annealing processes.

Upon poling a sample that had been wet or dry pre-annealed, multiple fringes typically emerge on the Maker-SHG scan as shown in Figures 2 and 3 for wet pre-annealed samples from lots 2 and 3. These

fringes are indicative of an optically active region throughout the entire sample bulk. Such fringes do not usually appear in poled *as received* samples, as shown in Figure 6. The two-lobed pattern shown in Figure 6 is characteristic of an interaction layer thickness less than the coherence length, i.e., a near-surface effect. The largest bulk effect relative to the near-surface effect has been found to occur when the SHG had been significantly altered. Upon dehydration, the emergence of the bulk effect relative to the near-surface effect is thought to occur from removal of the strong near-surface layer by the pre-annealing process. The strength of the SHG associated with the bulk effect generated in this way is very low. This is seen in Figures 3(d-f) for samples from lot 3 that had been wet pre-annealed at temperatures between 700°C and 900°C. When the SHG remained strong and a bulk effect emerged, hydration throughout the sample bulk is thought to be the leading factor. It has been shown by Holmberg, et al.⁽¹⁴⁾ that, even though the near-surface component of the hydration profile is an order of magnitude greater than that of the bulk, wet pre-annealing for longer times and at higher temperatures will result in a growth of the bulk component relative to the near-surface component. This is evident in Figures 2(c-f) for samples from lot 2 that had been wet pre-annealed between 600°C and 900°C.

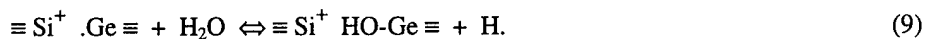
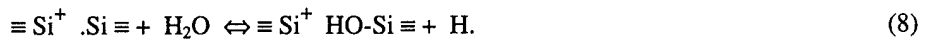
To determine the thickness of the optically active region, the experimental Maker-SHG pattern, shown in Figure 3f, was fit theoretically, Figure 7. Shown in Figure 7(a) is a theoretical Maker-SHG pattern, generated using an index of refraction value of 1.46071 for 532 nm radiation and an index of refraction value of 1.44963 for 1.06 μ m radiation. An interaction layer thickness of 1.501 mm, equivalent to the sample thickness was used. Upon comparing Figure 7(a) with Figure 7(b), it is apparent that the angular position of the fringes in the experimental curve coincide with those in the theoretical curve. This coincidence of angles implies that the SHG effect extends throughout the entire sample bulk. By examining the fringing patterns in Figures 2 and 3, it is apparent that bulk and near-surface components of the nonlinearity are simultaneously present. The relative component of the SHG from the near-surface and bulk may vary from an almost pure near-surface effect, Figure 2a, to an almost pure bulk effect, Figure 3f. Finally, one conclusion that can be drawn is that at least one microscopic cause of the SHG is not inherent to the near-surface.

B. EFFECT OF PRE-ANNEALING ON THE LEVEL OF DEFECT SITES

High power second harmonic mode electron paramagnetic resonance⁽¹¹⁾ was performed on wet and dry pre-annealed samples from lots 2 and 3. All samples were depoled except the samples from lot 2 that had been wet pre-annealed. For all lots of fused silica studied, both Si and Ge E' centers were observed, Figure 8. Note the presence of two peaks in very close proximity representing two distinct paramagnetic electron centers, each without hyperfine interaction. The peak located at a magnetic field of 3492.20 G with an associated electron Zeeman factor, g, of 1.9995 has been attributed to a germanium E' center and that located at a magnetic field of 3487.91 G with an associated g value of 2.001 has been attributed to the Si E' center.⁽¹⁵⁾ Because measurements were made in second harmonic mode, no absolute germanium density could be computed. From the very weak EPR signals obtained, concentrations of Si and Ge E' defect sites were probably less than $10^{15}/\text{cm}^3$.⁽¹⁶⁾

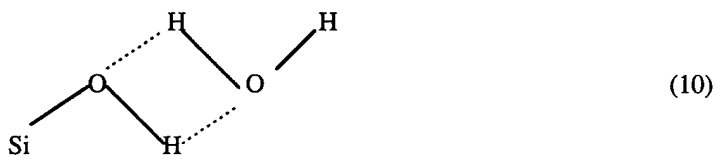
Upon comparing the level of defect sites in polarized (poled) and nonpolarized (depoled) fused silica, no significant differences were noted. This was to be expected since the SHG was largely confined to the near-surface while EPR looked primarily at the bulk.

Shown in Figure 9 are the relative concentrations of the Si and Ge E' centers along with d_{33} and FTIR data for wet pre-annealed samples from lot 2. The behavior of d_{33} can be explained in two ways, one of which points to metastable hydroxyl defects and the other to permanent hydroxyl defects as sources of the nonlinearity. First since there appears to be an inverse relationship between the level of Si and Ge E' defect sites and d_{33} , it is speculated that the optically active centers could be the precursors to the Si and Ge E' defect sites. Since water appears to be a factor causing a decrease in d_{33} on either side of a 600°C pre-annealing temperature for this lot of fused silica, as shown in Figures 4 and 5, one may speculate that water is involved in some sort of equilibrium reaction between an optically active defect site involving metastable hydroxyl and the E' center. In the literature, Devine⁽¹⁷⁾ speculates that the Si and Ge E' centers arise from their precursors via the following reactions:



where $\equiv \text{Si}^+ \cdot \text{Si} \equiv$ represents a E' center. [Note: the symbol \equiv represents the bonding of Si or Ge to three other atoms in the lattice.] Since the $\equiv \text{Si-OH}$ and $\equiv \text{Ge-OH}$ defects are the precursors to the non-bridging oxygen hole centers, these reactions would be consistent with the speculation by Mukherjee⁽²⁾ concerning the role of non-bridging oxygen hole centers in the generation of SHG and the reactions (1-3) presented by Olthuis⁽⁸⁾ for the charging of fused silica. Furthermore, FTIR spectra of wet pre-annealed samples from lot 2, as shown in Figure 9, support the above idea since the 3649 cm^{-1} peak, which corresponds to vibrations associated with internal Si-OH or pairs of Si-OH mutually linked by a hydrogen bond⁽¹⁸⁻²⁰⁾, is a maximum at a pre-annealing temperature of 700°C when the Si E' centers are at a minimum. The fact that the percentage change in the FTIR peak was less than the corresponding percentage change in d_{33} may be explained by the fact that the FTIR peak was composed of both metastable and permanent hydroxyl.

Secondly, the behavior of d_{33} may be explained by the presence of permanent hydroxyl and water in fused silica. According to Lee⁽¹²⁾, at pre-annealing temperatures less than 600°C , water diffuses into the fused silica lattice and remains in its molecular form. It is speculated that the observed decrease of d_{33} in the 400°C to 600°C pre-annealing temperature range results from the alteration of the permanent hydroxyl defect sites, $\equiv \text{Si-OH}$ and $\equiv \text{Ge-OH}$, through hydrogen bonding with water:



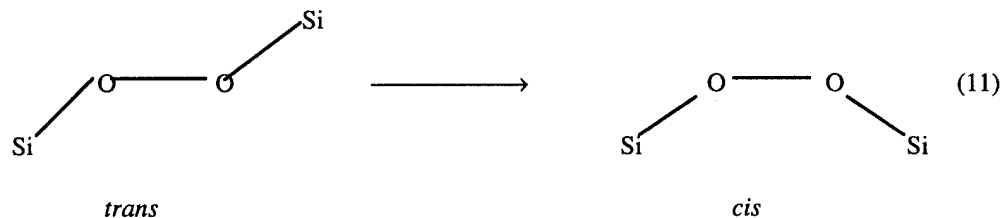
It is thought that water stabilizes the hydroxyl groups, making them immune to alteration through poling. This would explain the observed decrease in optical activity in this temperature range. As the temperature is increased from 400°C to 600°C , there is less molecular diffusion and hydrogen bonding but more reaction of water with the lattice to form metastable hydroxyl, which would account for the observed increase in d_{33} . Finally according to Lee⁽¹²⁾, at pre-annealing temperatures greater than 700°C , desorption of metastable hydroxide occurs which would explain the small observed decrease in d_{33} at pre-annealing

temperatures in excess of 600°C. Since the maximum d_{33} observed for wet pre-annealed fused silica was, within experimental error, equal to that for the dry pre-annealed samples, it is speculated that metastable hydroxyl played an insignificant role in the generation of second harmonic in this material.

For samples from lot 2 that had been dry pre-annealed, behavior similar to that observed for the corresponding wet pre-annealed samples from lot 2 was found for the relative concentrations of Si and Ge E' defect sites, as shown in Figure 10. But while d_{33} decreased on either side of a 600°C pre-annealing temperature for wet pre-annealed samples from lot 2, the level of d_{33} remained almost unchanged throughout the pre-annealing temperature range for the corresponding dry pre-annealed samples. Obviously, no correlation exists between d_{33} and either the E' centers or their removable metastable precursors for the dry pre-annealed samples from lot 2 except possibly for pre-annealing temperatures greater than 800°C. Because no other paramagnetic defect sites were found in this material, it is speculated that permanent hydroxide or a bond effect was the contributor to the SHG. Upon examination of the image charge data in Figure 10, it is apparent that the level of image charge on the parallel plates decreased as the pre-annealing temperature increased. This was unusual since the image charge usually followed the trends associated with d_{33} , see Figures 11 and 12. Since the image charge is related to the magnitude and distribution of the polarization within the sample, either the geometric distribution of the SHG was changing and/or the type of defect site generating the SHG was evolving. Upon examination of Maker-Fringe data, it is apparent that the geometric distribution was not changing as the pre-annealing temperature increased. So the most likely explanation of the data is that the microscopic source of the SHG was evolving as the pre-annealing temperature increased.

Upon examination of Figures 11 and 12, it is apparent that samples from lot 3 reacted in a similar way to both wet and dry pre-annealing. In addition, for both wet and dry pre-annealed samples, d_{33} was quenched at pre-annealing temperatures above 600°C. From Figures 11 and 12, it is apparent that the level of Ge and Si E' defect sites remained relatively constant for pre-annealing temperatures up to 700°C. d_{33} was obviously not correlated to the level of Si and Ge E' defect sites or their precursors. In addition, the relative concentration of the defect sites, within experimental error, were identical for both the wet and dry pre-annealed samples in the pre-annealing temperature range. This was unlike the behavior seen in lot 2 where

the relative concentration of E' defect sites for the dry pre-annealed material was, at a minimum, double those in the wet pre-annealed material. The relatively constant concentration of E' defect sites over the pre-annealing temperature range in addition to the lack of sensitivity of the d_{33} to water provides evidence that water did not react with the E' defect sites as in lot 2. For pre-annealing temperatures above 800°C, thermal growth of the Si and Ge E' defect sites was seen. Since d_{33} was virtually zero at these pre-annealing temperatures, the thermally generated defect sites were obviously not active in the generation of the second harmonic. Based on the fact that there was no correlation between d_{33} and the paramagnetic defect sites in addition to the fact that d_{33} was quenched at pre-annealing temperatures above 600°C, a "bond effect" is proposed to be a source of SHG in this lot of fused silica. This is further supported by the fact that permanent hydroxide is virtually nonremovable at pre-annealing temperatures less than 1000°C⁽¹²⁾, in addition, to the relatively extensive bulk contribution to the SHG compared to lot 2 material, Figures 2 and 3. It is apparent though by examining Figure 3 that when the SHG reached its maximum in the 500-600°C pre-annealing temperature range, a near-surface effect was predominant. This could be the result of water uptake to form metastable hydroxide. Based upon the literature^(17, 19-21), it is speculated that the peroxy bridge structure in the *trans* configuration, which is converted to the *cis*-like configuration lacking an inversion center⁽²²⁾ upon poling, equation 6, could be the optically active bond structure in lot 3 material.



According to Devine, et al.^(19, 20), peroxy-radical defect sites, which form from the reaction of diffusing O₂ with oxygen deficient sites within the material, pre-anneal to form peroxy bridges in the temperature range 300-600°C. This is consistent and could be another explanation for the growth of SHG in this temperature range besides metastable hydroxyl. In addition, observations by Freund, et al.⁽²¹⁾ indicate a thermal

dissociation of the peroxy bridge at pre-annealing temperatures above 500°C into two $\equiv \text{Si-O}$ groups which are suggested by Devine et al.⁽¹⁷⁾ to pre-anneal back into the lattice in the form $\equiv \text{Si-O-Si} \equiv$. This would support the sudden decline of the SHG to nearly zero between 500-600°C. Finally, Freund⁽²³⁾ also reports that the peroxy bond is expected to orientate itself when an external stress is applied. This would support speculation that the *trans* configuration is converted to its optically active form, the *cis*-like configuration, upon poling.

4. MODEL

Based on data associated with d_{33} , the image charge, EPR and FTIR, it is felt that the SHG in poled fused silica is likely coming from two sources. It is proposed that a “bond” effect in addition to a “hole-filling” effect plays a role in the generation of second harmonic. For samples of fused silica showing no correlation of d_{33} with paramagnetic defect sites, in addition to quenching at pre-annealing temperatures greater than 600°C, a 2nd order “bond” effect is thought to be generating the second harmonic. The optically active defect structure is felt to be the peroxy bridge defect in the *cis*-like configuration. It is proposed that upon poling, the *trans*-configuration having zero net dipole moment undergoes rotation about the O-O bond to form the *cis*-like configuration which has a net dipole moment, equation (6). Since the *cis*-like configuration is energetically unstable, it is felt that during the poling process the electric field aligns the dipoles which are then frozen in place when the sample is cooled. Upon depoling, the *cis*-like configuration most likely reverts back to the lower energy *trans*-configuration since no electric field is present to hold the structure in place. The net result of such a structure would be a second order SHG effect.

Finally, for lots of fused silica that maintain an appreciable d_{33} at higher pre-annealing temperatures, it is speculated that hydroxyl defect sites associated with Si and Ge are the sources of the SHG. One explanation for the behavior of d_{33} upon wet and dry pre-annealing is represented by an equilibrium between E' and metastable hydroxyl defect sites, equations (4) and (5). The SHG is then the greatest when the number of metastable hydroxyl defect sites are maximized. The trends in d_{33} can also be explained by the stabilization of permanent hydroxyl defect sites at lower pre-annealing temperatures through hydrogen bonding with molecular water and the desorption of metastable hydroxyl at higher temperature pre-anneals.

As a result, at both lower and higher pre-annealing temperatures, the number of hydroxyl defect sites available for poling is decreased. Finally, when a sample of fused silica containing $\equiv \text{Si-OH}$ and $\equiv \text{Ge-OH}$ defects is then poled, it is speculated that molecular hydrogen is released and the resultant non-bridging oxygen hole centers ($\equiv \text{Si-O} \cdot$ or $\equiv \text{Ge-O} \cdot$) are charged.

5. CONCLUSIONS

The level of SHG and concentration of defect sites in fused silica can be manipulated by wet or dry pre-annealing in nitrogen. In some lots of material, the effects of wet and dry pre-annealing do not differ significantly and the SHG goes virtually to zero when wet or dry pre-annealed above 500-600°C. In other lots of fused silica, the effects of wet and dry pre-annealing are quite distinct in that wet pre-annealing decreases the SHG significantly on either side of 600°C while dry pre-annealing has virtually no effect over the range of pre-annealing temperatures from 400-900°C.

It has also been found that the effect on the SHG of either a wet or dry pre-anneal can be, in some cases, fully reversed by the opposite pre-annealing process.

After either wet or dry pre-annealing, a weak bulk SHG effect has been found to emerge. This demonstrates that the source of the SHG is not limited to defects inherent only to the sample near-surface.

EPR analysis has shown that fused silica contains Si and Ge E' centers. d_{33} , image charge, EPR and FTIR data reveals the presence of one possible second order "bond effect" in addition to a third order "hole-filling effect". The molecular source of the "bond effect" is proposed to be the peroxy bridge structure which is converted from the *trans* configuration to the a *cis*-like configuration upon poling. The third order "hole-filling effect" is speculated to originate from the charging of the $\equiv \text{Si-O} \cdot$ and $\equiv \text{Ge-O} \cdot$ non-bridging oxygen hole centers, which are derived from metastable and permanent hydroxyl defect sites, to set up a depletion region.

Finally, there is still little known about the molecular cause of SHG in fused silica. Future work will focus on designing experiments to confirm or deny the role of hydroxide defect sites and peroxy bridge structures in the generation of second harmonic. In addition, the energetics associated potentially optically active defect sites will be studied with semi-empirical and *ab-initio* quantum chemistry calculations.

REFERENCES

1. R. A. Myers, N. Mukherjee and S. R. J. Brueck, "Large second-order nonlinearity in poled fused silica," *Opt. Lett.* **16**(1991)1732.
2. N. Mukherjee, R. A. Myers and S. R. J. Brueck, "Dynamics of second-harmonic generation in fused silica," *J. Opt. Soc. Am. B.*, **11**(4)(1994)665-669.
3. H. Nasu, H. Okamoto, M. Mito, J. Matsuoka and K. Kamiya, "Influence of the OH content on second harmonic generation from electrically polarized SiO₂ glasses," *Jpn. J. Appl. Phys.* **32**(1993)L406-L407.
4. P. G. Kazansky, A. Kamal and P. St. J. Russell, "Erasure of thermally poled second-order nonlinearity in fused silica by electron implantation," *Opt. Lett.*, **18**(14)(1993)1141-1143.
5. S. K. Lai, D. R. Young, J. A. Calise and F. J. Feigl, "Reduction of electron trapping in silicon dioxide by high-temperature nitrogen anneal," *J. Appl. Phys.*, **52**(9)(1981)5691-5695.
6. E. H. Nicollian, A. Goetzberger, and C. N. Berglund, "Avalanche injection currents and charging phenomena in thermal SiO₂," *Appl. Phys. Lett.* **15**(1969)174.
7. E. H. Nicollian, C. N. Berglund, P. F. Schmidt and J. M. Andrews, "Electrochemical charging of thermal SiO₂ films by injected electron currents," *J. of Appl. Phys.* **42**(13)(1971)5654-5664.
8. W. Olthuis and P. Bergveld, "On the charge storage and decay mechanism in silicon dioxide electret," *IEEE Trans. on Elec. Insul.* **27**(4)(1992)691-697.
9. J. Jerphagnon and S. K. Kurtz, "Maker-fringes: a detailed comparison of theory and experiment for isotropic and uniaxial crystals," *J. of Appl. Phys.*, **41**(4)(1970)1667-1681.
10. X. -C. Long, R. A. Myers and S. R. J. Brueck, "Measurement of the linear electro-optic coefficient in poled amorphous silica," *Optics Letters* **19**(22)(1994)1819-1821.
11. D. L. Griscom, "Characterization of three E'-center variants in X- and γ - irradiated high purity α -SiO₂," *Nuc. Instr. and Meth. in Phys. Rsch.* **B1**(1984)481-488.
12. R. W. Lee, "On the role of hydroxyl in the diffusion of hydrogen in fused silica", *Physics and Chemistry of Glasses* **5**(2)(1964)35-43.

13. J. E. Shelby, "Molecular diffusion and solubility of hydrogen isotopes in vitreous silica", J. of Appl. Phys. **48**(8)(1977)3387-3394.
14. G. L. Holmberg, A. B. Kuper and F. D. Miraldi, "Water contamination in thermal oxide on silicon," J. of the Electrochem. Soc., **117**(5)(1970)677-682.
15. T. E. Tsai, M. A. Saifi, E. J. Friebele, D. L. Griscom and U. Osterberg, "Correlation of defect centers with second-harmonic generation in Ge-doped and Ge-P-doped silica-core single-mode fibers", Optics Letters **14**(18)(1989)1023-1025.
16. Private communication with Dr. David L. Griscom of Naval Research Laboratory.
17. R. A. B. Devine and C. Fiori, "Thermally activated peroxy radical dissociation and annealing in vitreous SiO₂," J. Appl. Phys. **58**(9)(1985)3368-3372.
18. M. S. Aslanova, S. G. Klimanov, S. E. Rudakova and V. E. Khazanov, "ESR- and IR- spectral investigation of quartz fibers," Izvestiya Akademii Nauk SSSR, Neorganicheskie Materialy **11**(5)(1975)890-895.
19. G. Oriel, J. Phalippou and L.L. Hench, "Structural changes of silica xerogels during low temperature dehydration", J. of Non-Cryst Solids **88**(1986)114-130.
20. R.S. McDonald, "Surface functionality of amorphous silica by infrared spectroscopy", J. Phys. Chem. **62**(1958)1168.
21. R. A. B. Devine, J. J. Capponi and J. Arndt, "Oxygen-diffusion kinetics in densified, amorphous SiO₂," Phys. Rev. B **35**(2)(1987)770-773.
22. R. A. B. Devine, "The role of activation energy distributions in diffusion related annealing in SiO₂," J. Appl. Phys. **58**(2)(1985)716-719.
23. F. Freund, M. M. Masuda and M. M. Freund, "Highly mobile oxygen hole-type charge carriers in fused silica," J. Mat. Rsch. **6**(8)(1991)1619-1622.
24. P. N. Prasad and D. J. Williams, Introduction to nonlinear optical effects in molecules and polymers, John Wiley and Sons, Inc. ©1991.
25. F. Freund, "Conversion of dissolved "water" into molecular hydrogen and peroxy linkages", J. of Non-Crystalline Solids **71**(1985)195-202.

Figure Captions

Figure 1 - Experimental setup of Maker-SHG scan. Inset shows the geometrical arrangement of the p-polarized input 1.06 μm beam with respect to the poled sample.

A = RG695 filter, B = attenuation filters, C = BG18 filter, D = 530 nm band pass filter.

Figure 2 - Relative intensity of SHG [a.u.] vs rotation angle [degrees] for poled samples from lot 2 that had been wet pre-annealed at a series of temperatures: a) 400°C, b)500°C, c)600°C, d)700°C, e)800°C, f)900°C. [Note: the amplitudes of the Maker-Fringe scans are not drawn to scale. The amplitudes of (b)-(f) relative to (a) are indicated at the far right of each Maker-Fringe scan.]

Figure 3 - Relative intensity of SHG [a.u.] vs rotation angle [degrees] for poled samples from lot 3 that had been wet pre-annealed at a series of temperatures: a) 400°C, b)500°C, c)600°C, d)700°C, e)800°C, f)900°C. [Note: the amplitudes of the Maker-Fringe scans are not drawn to scale. The amplitudes of (b)-(f) relative to (a) are indicated at the far right of each Maker-Fringe scan.]

Figure 4 - Percentage change in d_{33} for a series of samples from lots 1-3 that have been wet pre-annealed over the temperature range 400°C to 900°C. [Note: samples from lot 1 have only been wet pre-annealed whereas samples from lots 2 and 3 have been both wet and dry pre-annealed, see Figure 2.]

Figure 5 - Percentage change in d_{33} for a series of samples from lots 2-4 that have been dry pre-annealed over the temperature range 400°C to 900°C. Note that samples from lot 4 have only been dry pre-annealed whereas samples from lots 2 and 3 have been both wet and dry pre-annealed, see Figure 1.

Figure 6 - Relative intensity of SHG [a.u.] vs rotation angle [degrees] for a poled *as received* sample.

Figure 7 - a. Theoretical Maker-SHG fit using an index of refraction value of 1.46071 for 532 nm radiation and an index of refraction value of 1.44963 for 1.06 μm radiation. An interaction layer thickness of 1.65 mm, which was equivalent to the sample thickness, was also used, b. Experimental maker SHG scan of a sample after dry pre-annealing

Figure 8 - High power electron paramagnetic resonance spectrum of a sample of fused silica. The peak located at a magnetic field value of 3485.23 G has been attributed to the Ge E' center and that located at 3480.96 G has been attributed to the Si E' center.

Figure 9 - Samples from lot 2 that have been wet pre-annealed over a series of temperatures from 400°C to 900°C, a. d_{33} [pm/V] vs pre-annealing temperature [°C], b. relative intensity of 3649 cm^{-1} peak [a.u.], c. Relative concentration of Si E' centers [a.u.] vs pre-annealing temperature [°C], d. Relative concentration of Ge E' centers [a.u.] vs pre-annealing temperature [°C].

Figure 10 - Samples from lot 2 that have been dry pre-annealed over a series of temperatures from 400°C to 900°C, a. d_{33} [pm/V] vs pre-annealing temperature [°C], b. Image charge $\times [105]$ [°C] vs pre-annealing temperature [°C], c. Relative concentration of Si E' centers [a.u.] vs pre-annealing temperature [°C], d. Relative concentration of Ge E' centers [a.u.] vs pre-annealing temperature [°C].

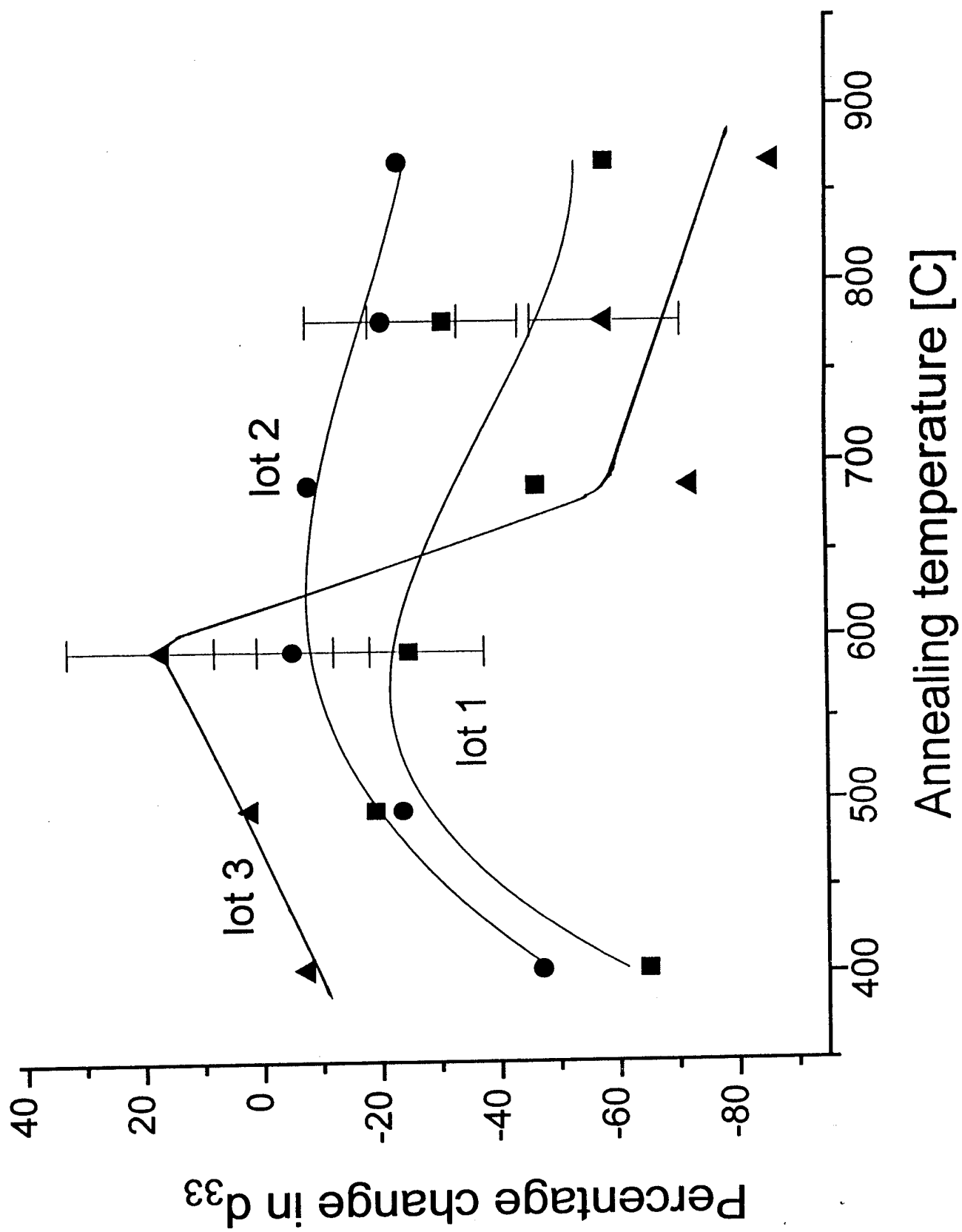
Figure 11 - Samples from lot 3 that had been wet pre-annealed over a series of temperatures from 400°C to 900°C, a. d_{33} [pm/V] vs pre-annealing temperature [°C], b. Image charge $\times 10^5$ [C] vs pre-annealing temperature [°C], c. Relative concentration of Ge E' centers [a.u.] vs pre-annealing temperature [°C], d. Relative concentration of Si E' centers [a.u.] vs pre-annealing temperature [°C].

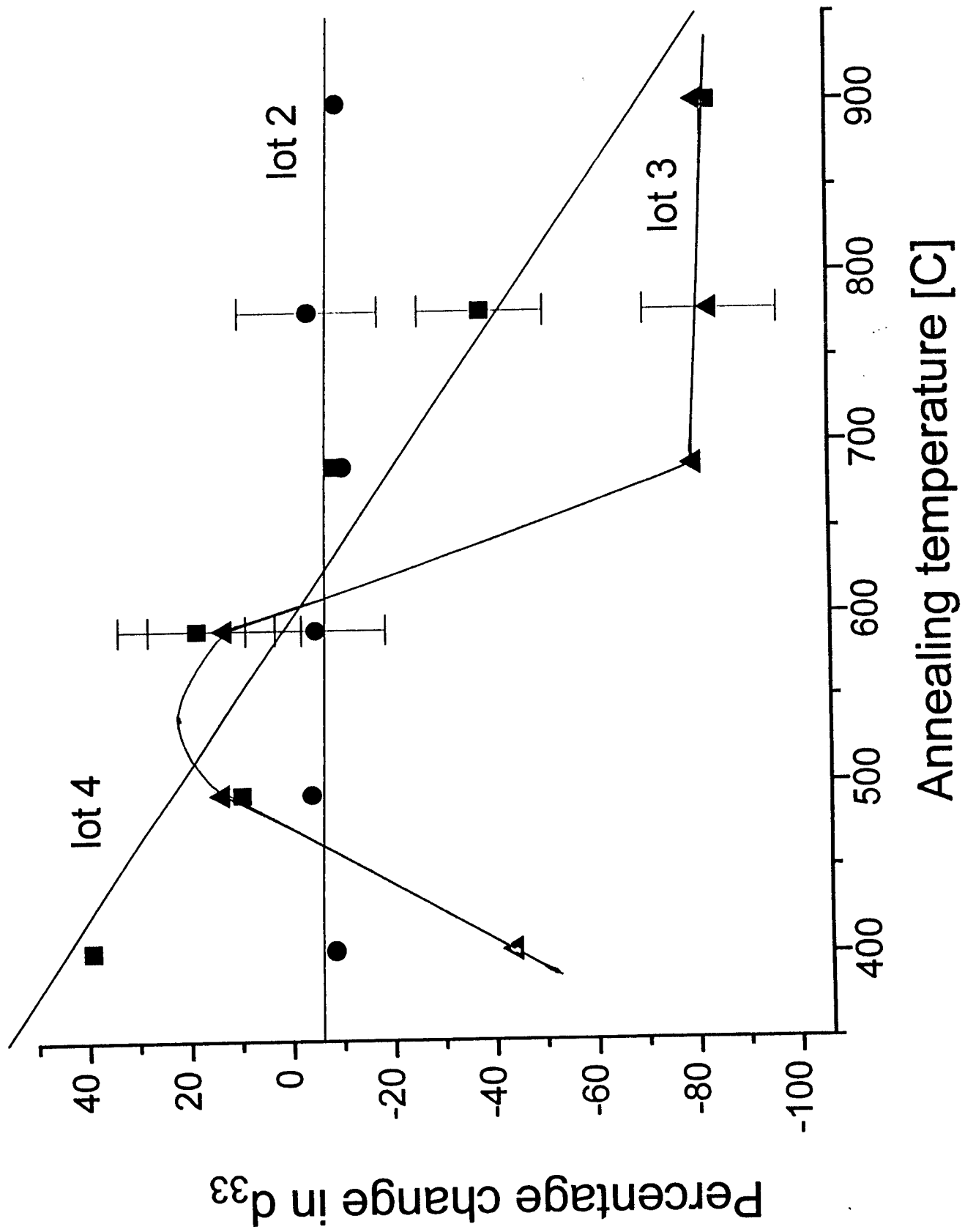
Figure 12 - Samples from lot 3 that had been dry pre-annealed over a series of temperatures from 400°C to 900°C, a. d_{33} [pm/V] vs pre-annealing temperature [°C], b. Image charge $\times 10^5$ [C] vs pre-annealing temperature [°C], c. Relative concentration of Si E' centers [a.u.] vs pre-annealing temperature [°C], d. Relative concentration of Ge E' centers [a.u.] vs pre-annealing temperature [°C].

Tables

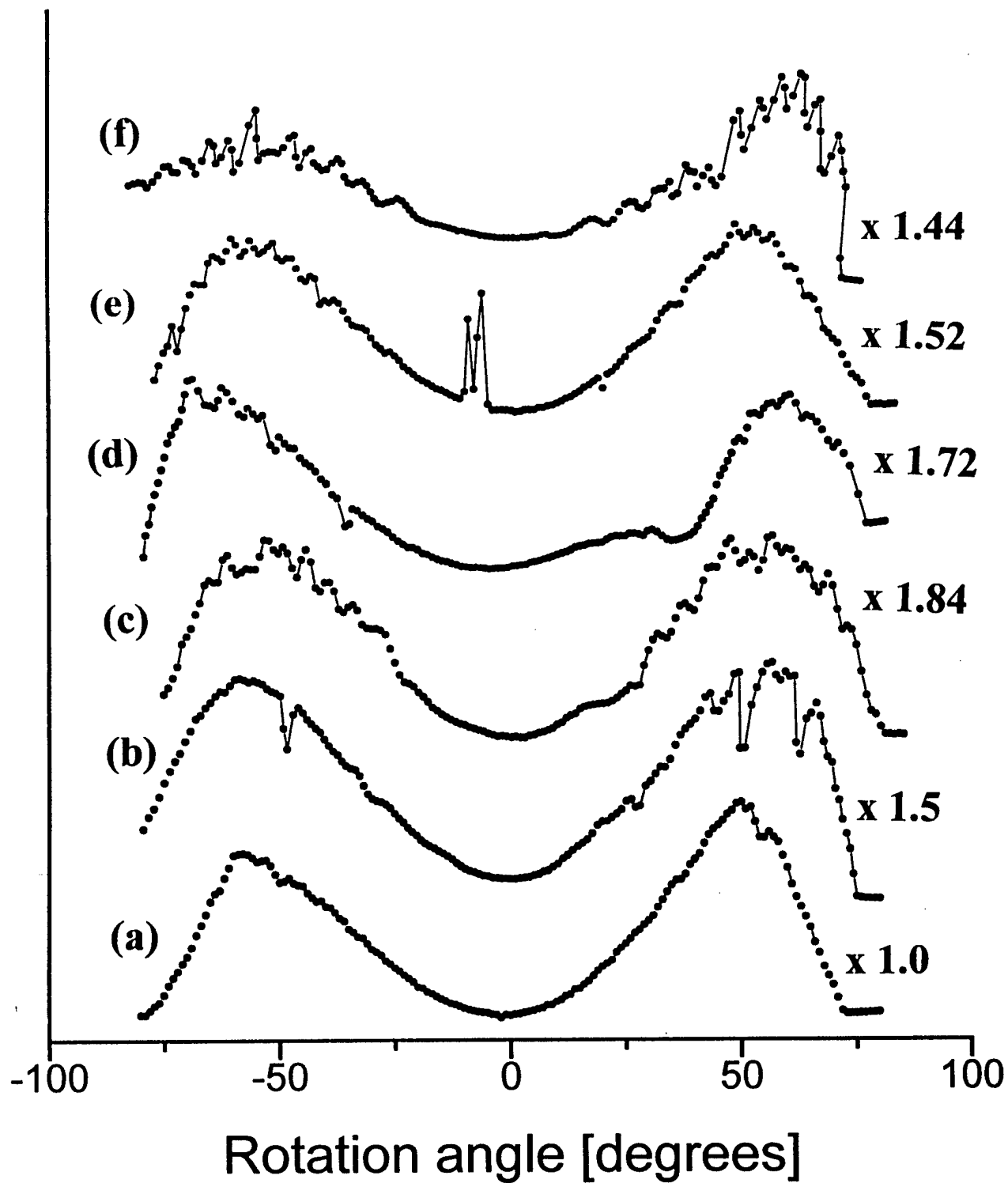
Table 1 -EPR parameters used for analysis of defect sites in fused silica by the high power second harmonic method

EPR parameter	Value
Receiver gain	1.0×10^5
Phase	229°
Harmonic	2
Modulation frequency	50 kHz
Modulation amplitude	6.232 G
Conversion	81.92 msec
Time constant	163.84 msec
Sweep time	167.772 sec
Center field	3490 G
Sweep width	300 G
Resolution	2048
Frequency	9.773 GHz
Power	20 mW

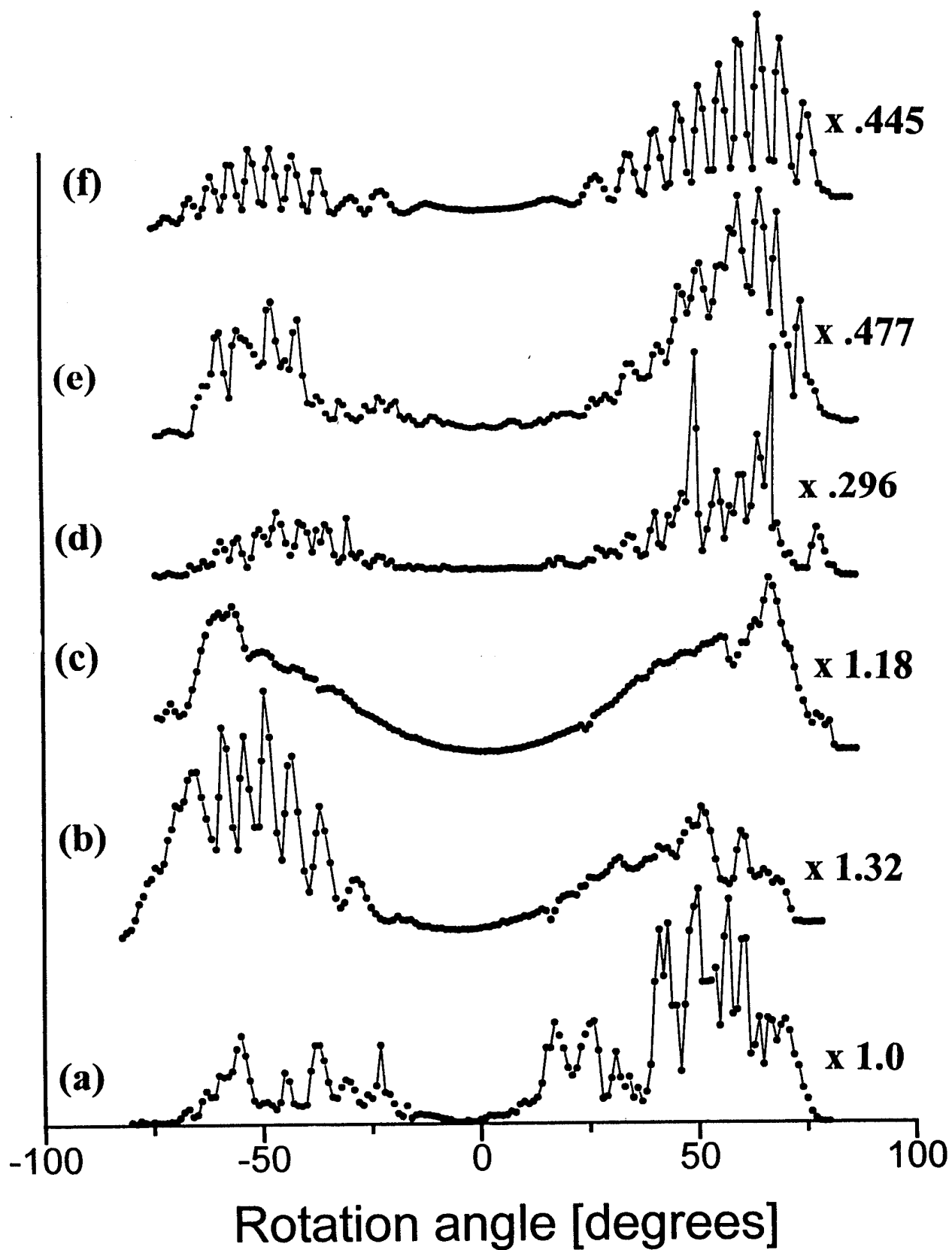


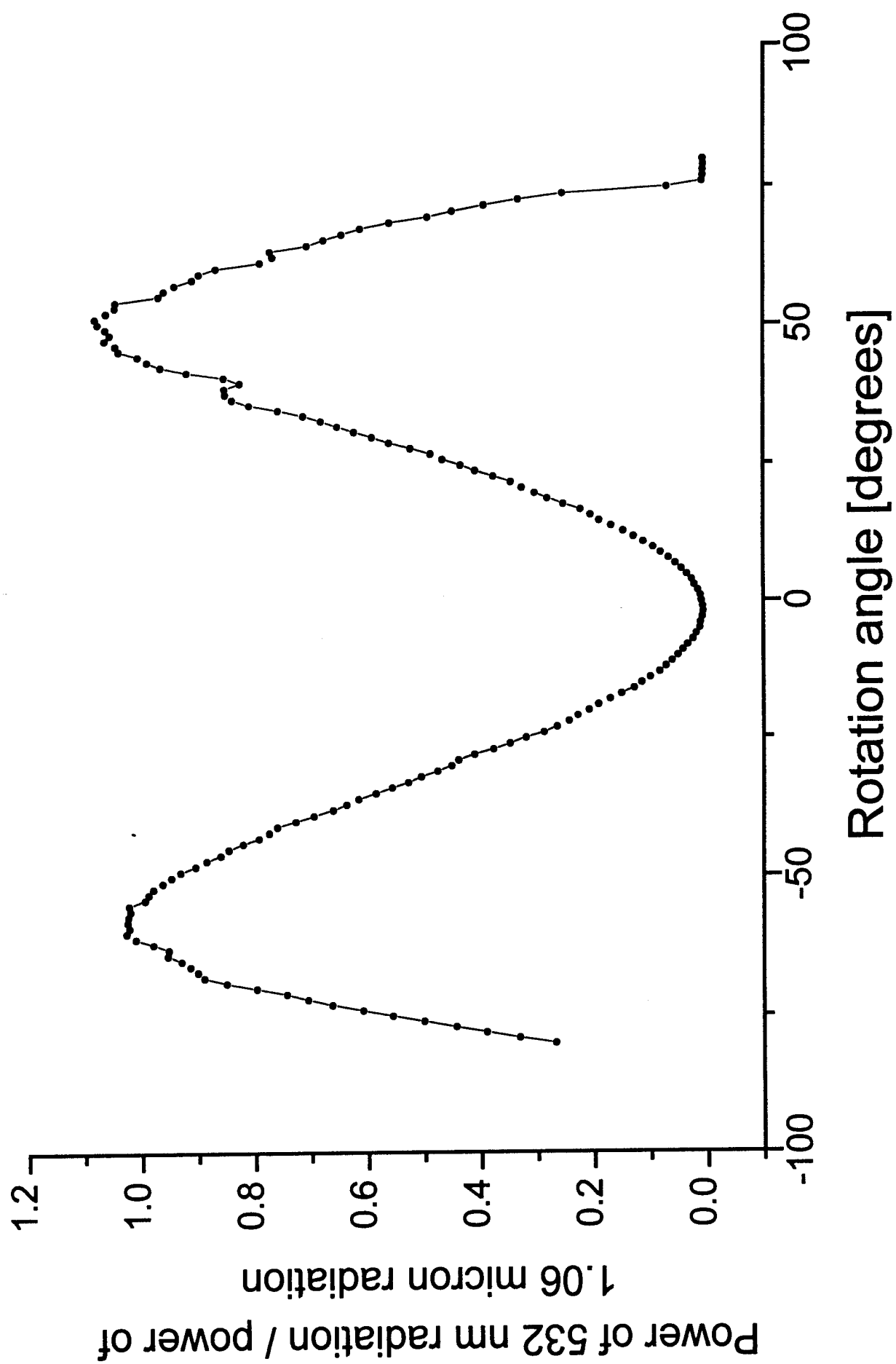


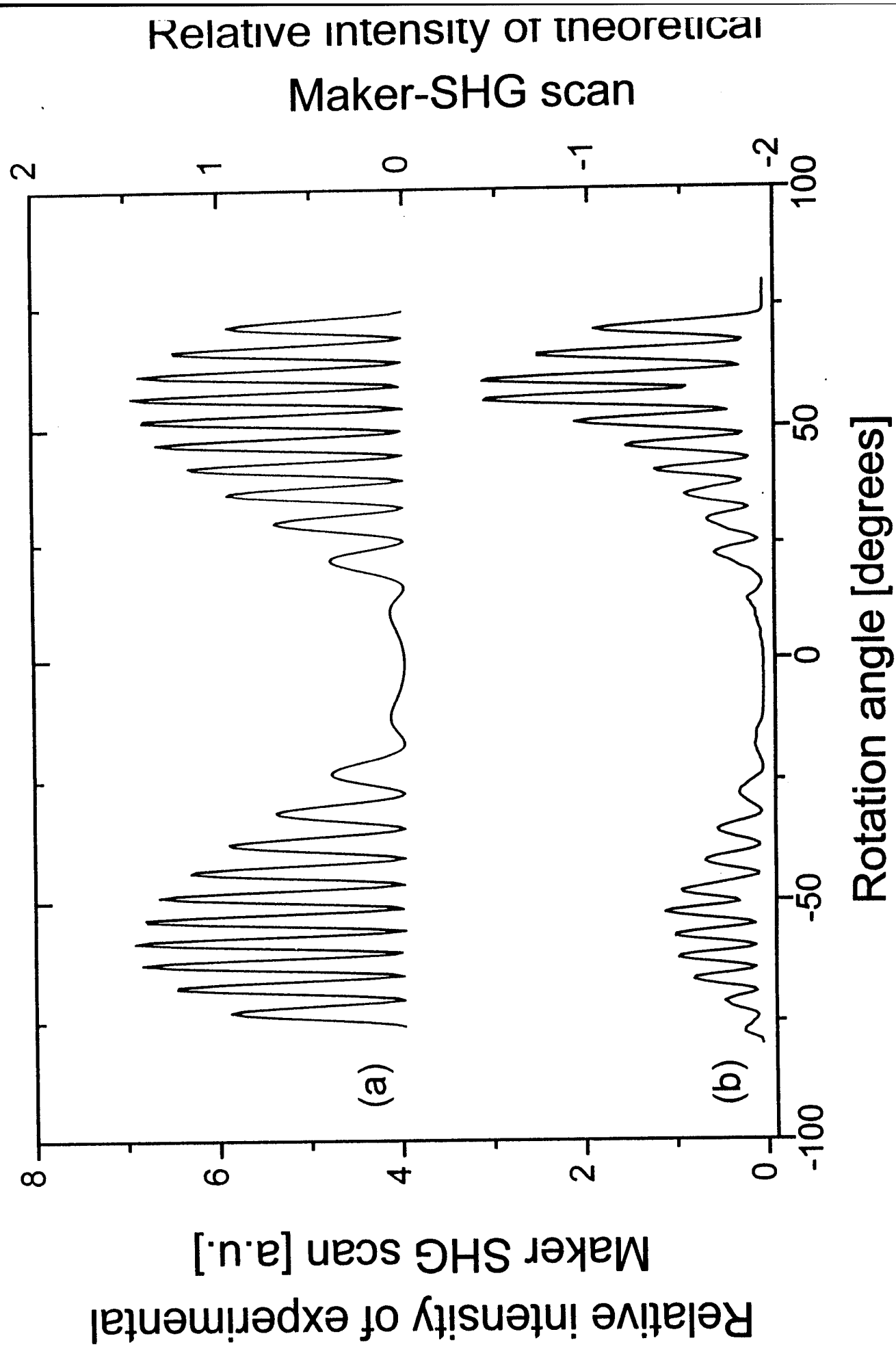
Power of 532 nm radiation / power of 1.06 micron radiation

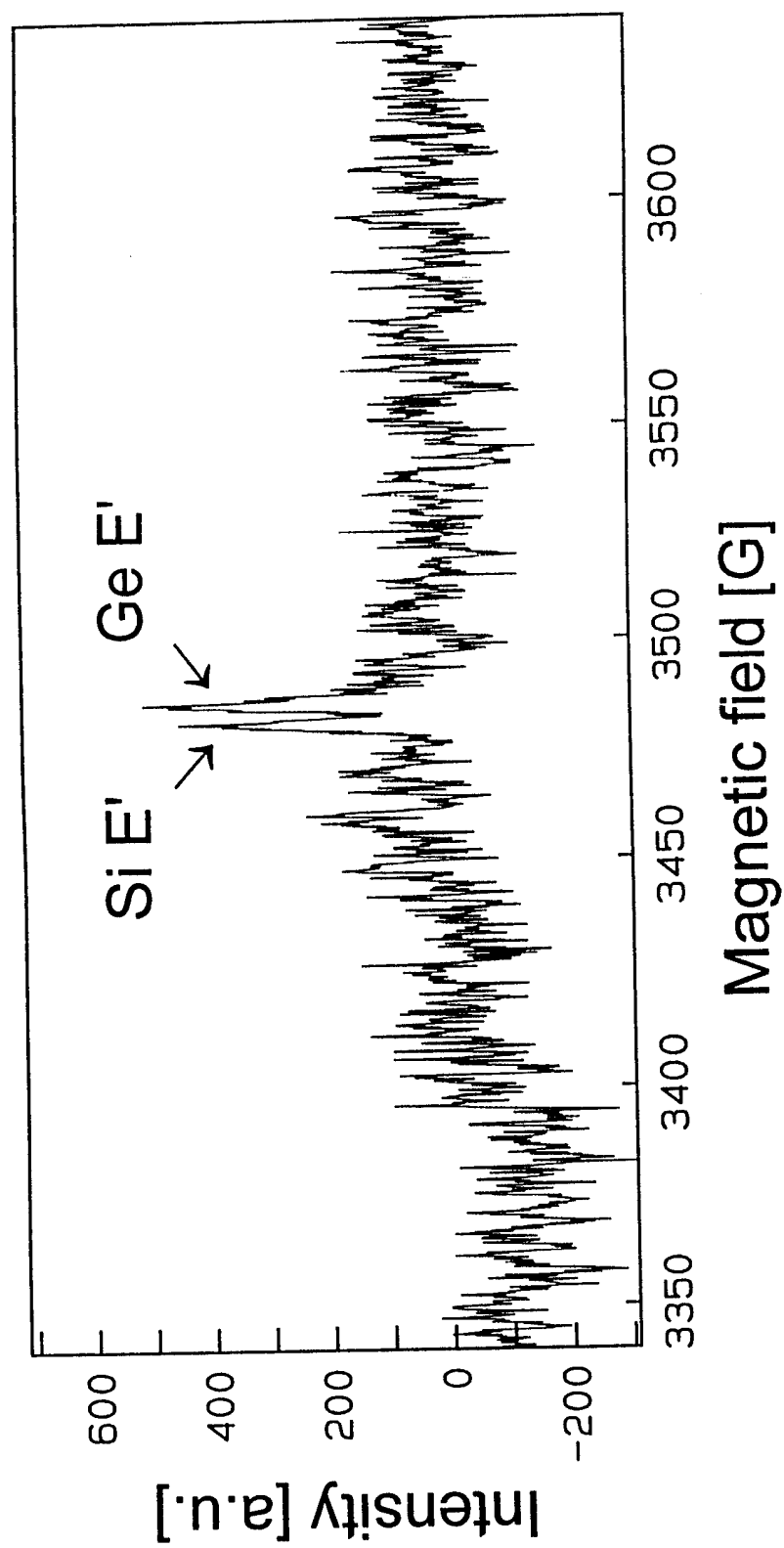


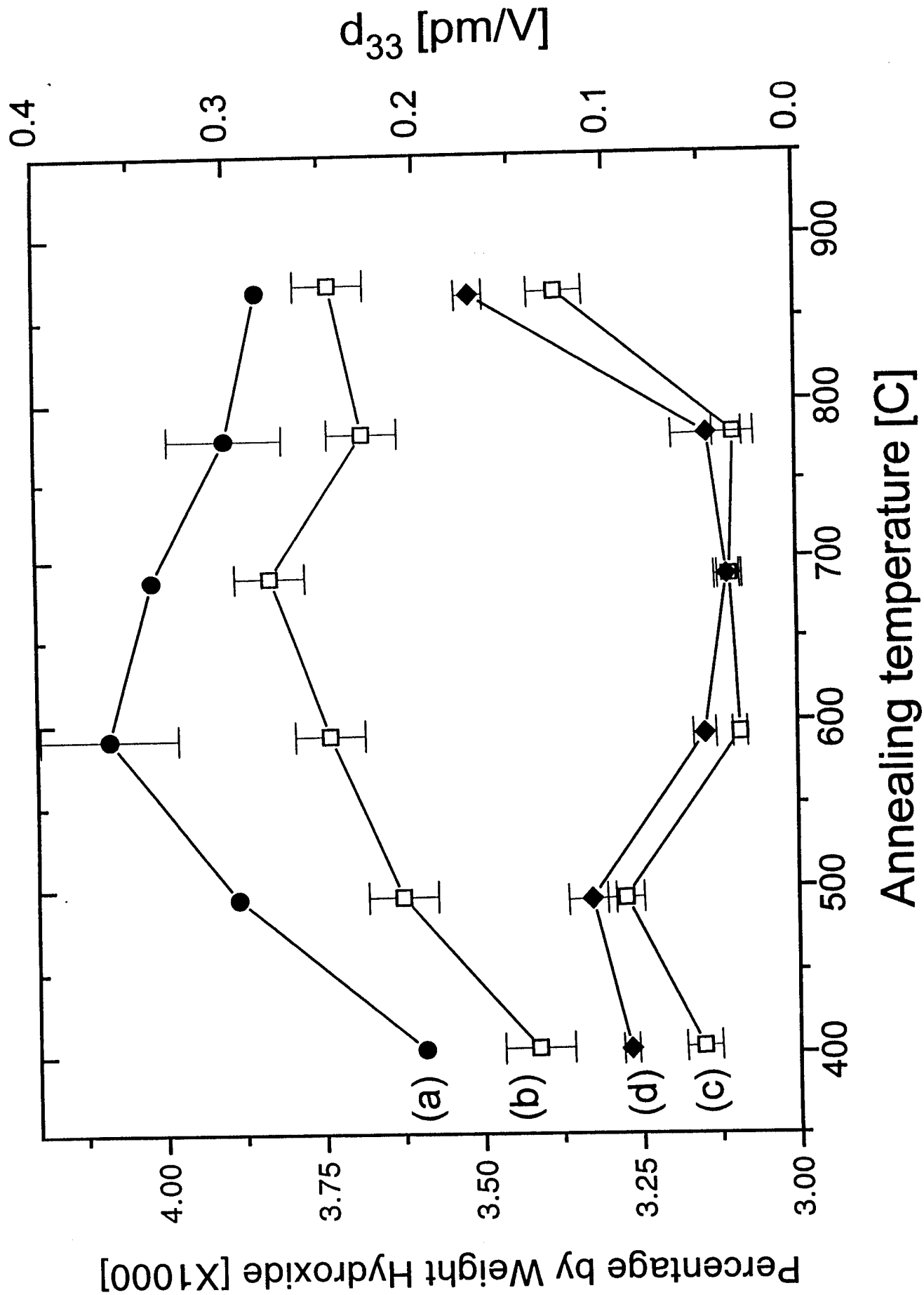
Power of 532 nm radiation / power of 1.06 micron radiation

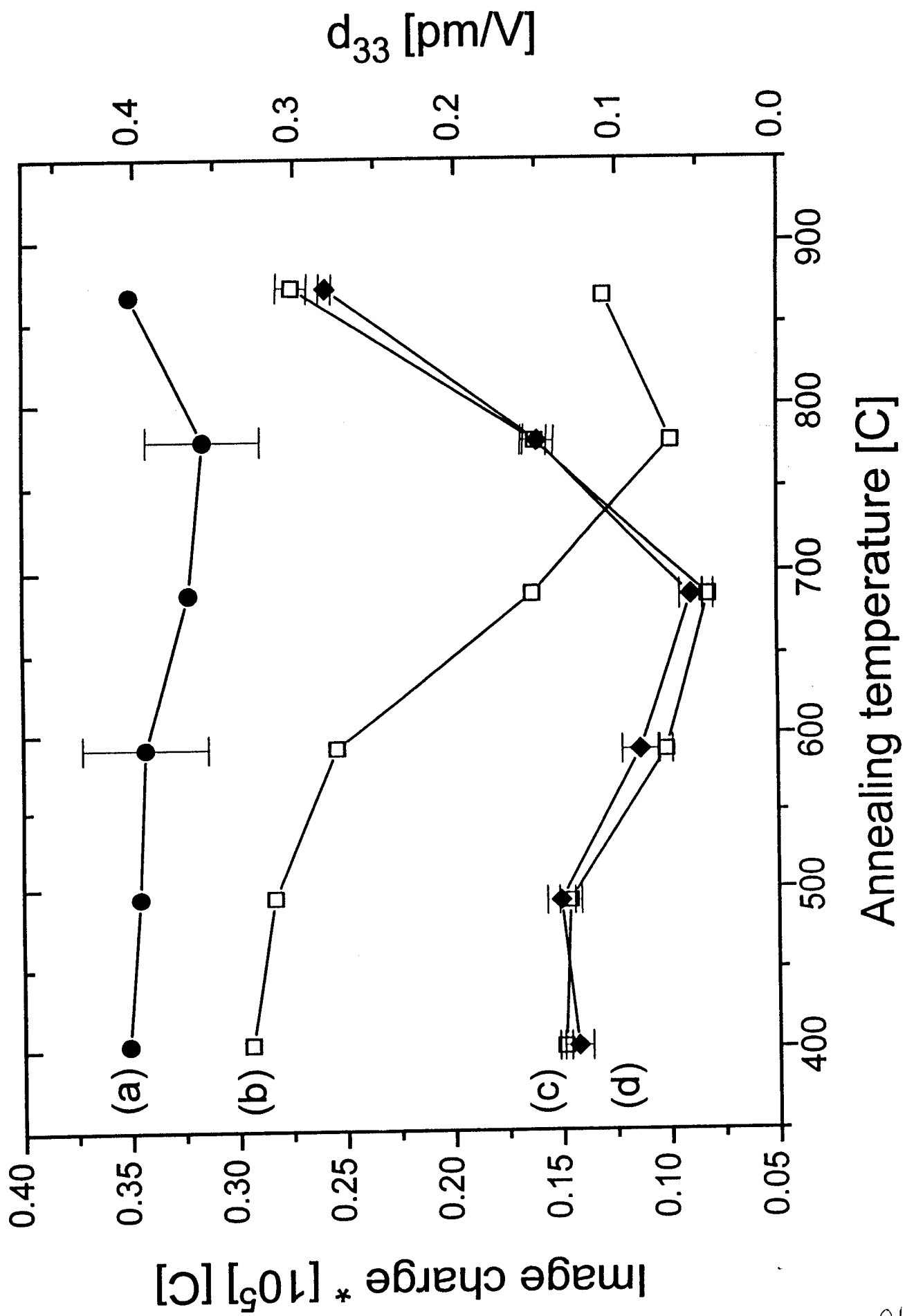


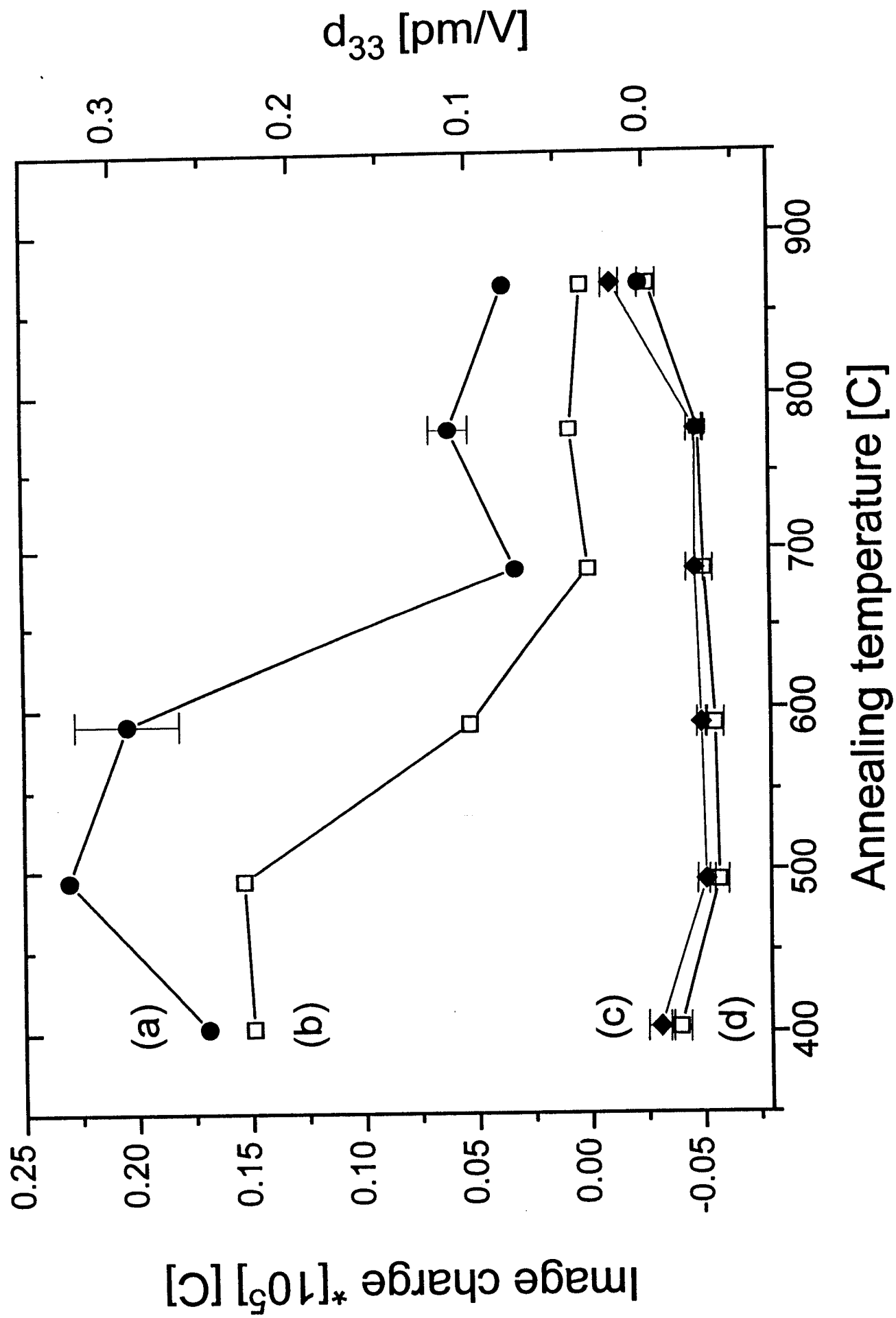


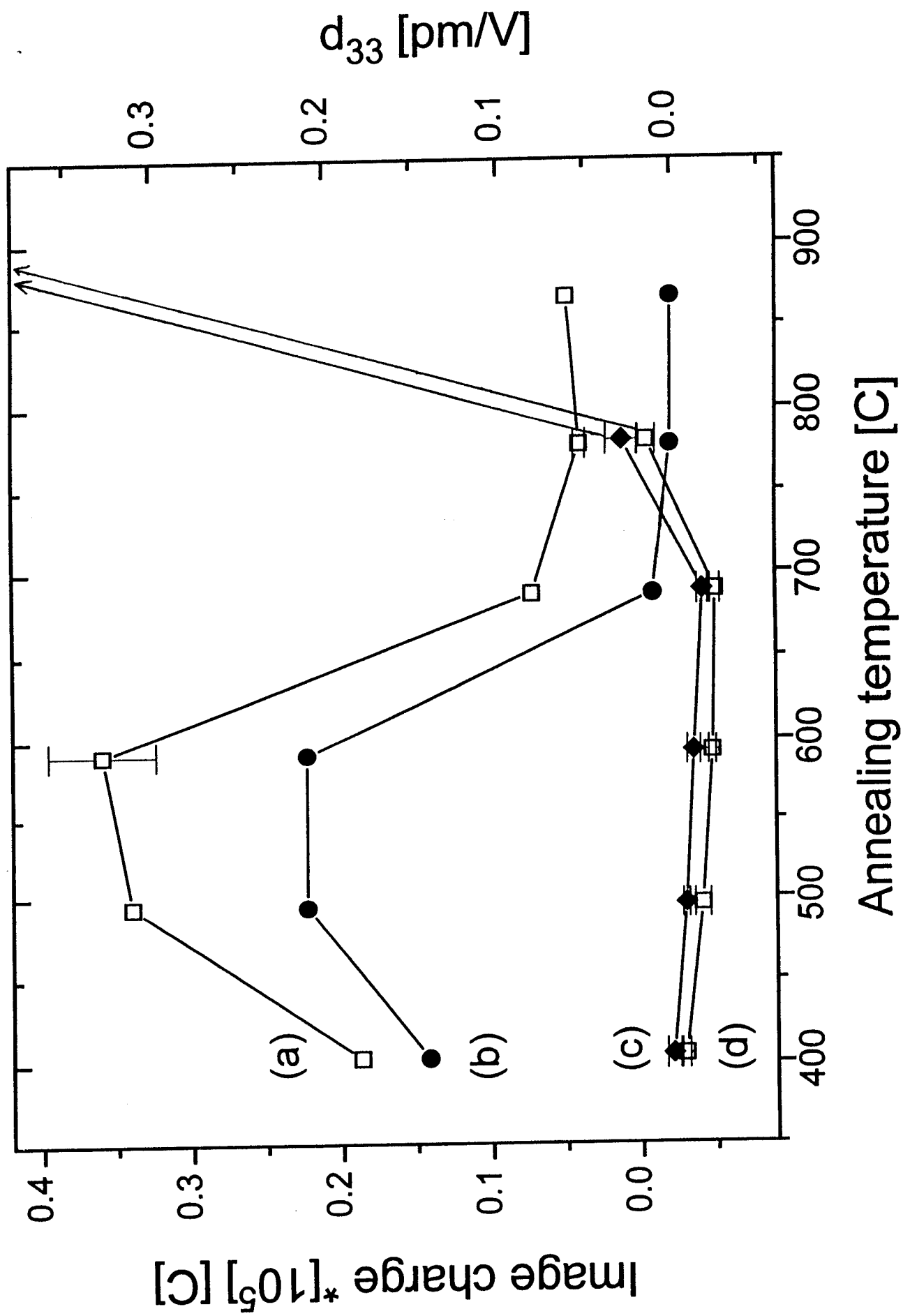












SPECTROSCOPIC INVESTIGATIONS OF LASER ABLATED GERMANIUM OXIDE

Paul J. Wolf*, Brian M. Patterson*, and Sarath Witanachchi**

*Frank J. Seiler Research Laboratory, Materials Physics Division, USAF Academy, CO 80840

**Department of Physics, University of South Florida, Tampa, FL 33620

ABSTRACT

Laser produced plumes from a GeO_2 target were investigated using both optical emission spectroscopy and laser induced fluorescence. Elemental neutral and ionic Ge and diatomic GeO were monitored as a function of O_2 pressure at 4 cm from the target surface. Data obtained from laser fluorescence experiments showed no indication of chemical production of GeO in these plumes under any conditions studied; however, the atomic emission intensities of several ionic and neutral Ge lines appeared to increase with O_2 pressure. This signified plume interactions with the background gas. The trends in the species concentrations were determined and the results are interpreted with respect to mechanisms for thin film growth.

INTRODUCTION

Our recent work in growing thin films of germanium dioxide (GeO_2) using laser ablation deposition showed that stoichiometric thin films can be fabricated under two different deposition conditions, and the results of these studies suggest the possibility of two separate kinetic mechanisms for growing these films. First, stoichiometric films could be produced by ablating a GeO_2 target in 150 mTorr of ambient O_2 [1]. At these relatively high pressures, elemental Ge in the ablation plume can react gas kinetically [2] with O_2 to form GeO, which can subsequently recombine with excess O_2 at the substrate surface in a disproportionation reaction. Generally, the oxygen content in the films increased with O_2 pressure from 10^{-5} to 0.15 Torr.

Performing depositions at 100's mTorr of an ambient gas causes the plume to become very highly forward directed [3] and leads to films of nonuniform thickness. For that reason, we explored film depositions at low pressures to produce plumes that are spatially more extended and allow a better opportunity to produce flat films for optical waveguides. Stoichiometric films were prepared at lower background pressures when the ablation plume was passed through a dc discharge in a 30 mTorr oxygen background [4]. In these studies, we found that the combination of the substrate temperature and the dc discharge enabled us to incorporate the correct oxygen content in the film. At these lower pressures, chemical reactions would appear unlikely because of the low collision rates between Ge and any ambient gas. However, the discharge could activate the material in the plume or the ambient gas providing additional energetic species to promote surface recombination reactions.

Reactions between elemental species in laser produced plumes and a reactive background gas are known to be important for producing good quality high T_c superconducting thin films [5]. An understanding of the potential chemical processes occurring between the plume material and any reactive gas in between the target and the substrate is needed to elucidate the important thin film growth mechanisms. Thus, the aim of this work is to explore the microscopic mechanisms responsible for forming high quality dielectric thin films under both growth conditions discussed above.

EXPERIMENT

Figure 1 shows a schematic diagram of the experimental apparatus. A pulsed ArF excimer laser [$\lambda = 193$ nm, pulse width of 28 ns (FWHM)] was focused onto the surface of a GeO_2 target at normal incidence with an energy density of 1 J cm^{-2} . The target was housed in a chamber that routinely achieved a base pressure of 5×10^{-6} Torr. Oxygen was metered into the chamber with a needle valve and a ring electrode biased at -1.5 kV was inserted in the plume path to determine the effect of a dc discharge on the constituents. The emission from the laser-produced plume (with and without the discharge) was imaged onto a spectrometer and the dispersed signal was detected using a linear diode array (OMA III). The time-integrated emissions were examined as a function of O_2 pressure at 4 cm from the target surface in spectral regions that covered emission features originating from electronically excited states of Ge I, Ge II, GeO, and O I.

The laser fluorescence experiments were performed using the frequency doubled output of a pulsed dye laser. The dye laser probe beam interrogated the plume perpendicular to the excimer laser beam, and the fluorescence was collected at 90° to the dye laser beam. The timing between the two pulsed lasers was varied between 1 and 50 μsec so that the plume constituents could be probed as a function of time from the ablation laser pulse. The timing of the OMA gate was maintained so that the probe beam sampled the plume material within the 500 ns gate width of the OMA. Ge atoms were probed by exciting from the ground 3P_0 state to the 3P_1 level at 265.16 nm and observing the fluorescence from this state with the gated OMA III system. GeO molecules were probed at 261.4 nm which promoted population from the $X^1\Sigma (v'' = 0)$ to the $A^1\Pi (v' = 1)$ state. The entire $v' = 1$ progression from GeO ($A \rightarrow X$) was captured with the gated OMA in a single trace.

RESULTS

Figure 2 shows a sample of a time-integrated plasma emission spectrum. The plume luminescence was caused by electronic transitions in neutral Ge (Ge I), singly ionized Ge (Ge II), and neutral O (O I) atoms. At pressures below ≈ 50 mTorr and with no discharge, the emission emanated solely from excited Ge I. The emission intensities remained constant from vacuum to about 10 mTorr of added O_2 and increased by a factor of 10 between 10 and 100 mTorr. This behavior could be attributed to species confinement at higher backing gas pressures which increases the number of emitters per volume [6]. Application of the discharge at low pressures (i.e., $P(\text{O}_2) < 50$ mTorr) enhanced both the Ge I and O I atomic emissions as shown in Fig. 2. No GeO emission was observed under any conditions in these experiments.

The various channels that are open to creating these electronically excited states in the plume material make it difficult to monitor the behavior of any one species independent of the formation mechanism. In order to circumvent this limitation, the behavior of species in the plume was monitored as a function of ambient gas pressure using laser induced fluorescence (LIF). Figure 3 shows a sample LIF spectrum of Ge I. The ground state Ge I concentration appears to decrease with increasing O_2 pressures as illustrated in Fig. 4. The decay, when converted to a rate coefficient, is consistent with the known reaction rate coefficient for $\text{Ge} + \text{O}_2 \rightarrow \text{GeO} + \text{O}$ [2]. The Ge LIF intensities were also monitored as a function of N_2 pressure to test whether or not the decay is due to this reaction scheme. Collisions between N_2 and Ge are non-reactive and should yield little or no decrease in the Ge I concentration with pressure. We found, however, that the Ge concentration decreased with increasing N_2 pressures with a rate that was only 40% slower

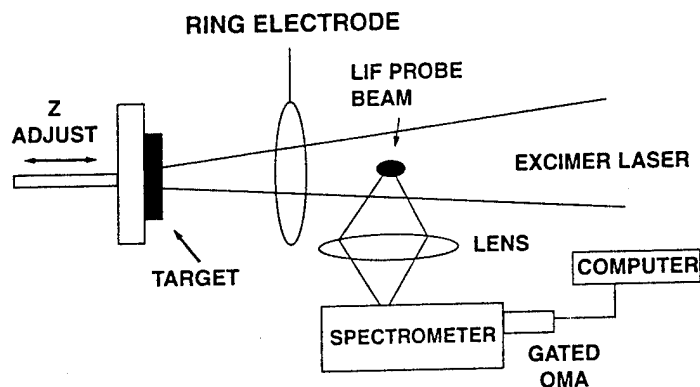


Figure 1. Diagram of the experimental system. The diagram shows the arrangement for the LIF studies. The set-up for the optical emission studies changes by removing the dye laser beam and operating the OMA in an ungated mode.

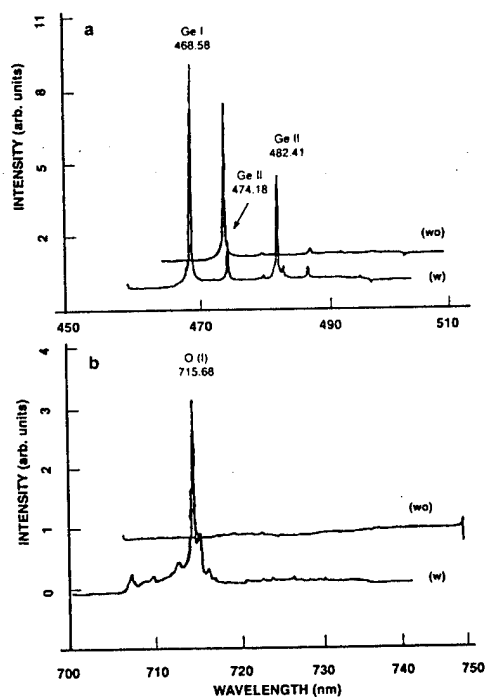


Figure 2. Time-integrated plasma emission spectrum recorded at an oxygen pressure of 30 mTorr and at 4.0 cm from the target surface. Trace (a) shows Ge emission with (w) and without (wo) the discharge while trace (b) shows the behavior of atomic oxygen.

than that for O_2 . This may indicate that the decays are not caused by a chemical depletion of ground state atoms. Electronic quenching could account for these decays, but the radiative lifetimes of the states under study (≈ 250 ns) prohibit such encounters [7]. For example, the time between collisions in an equilibrium mixture is about 12 μs so the electronic states will never see a collision. These pressure experiments were repeated with the dc discharge with no difference in the results.

Although the emission studies did not reveal the presence of GeO^* , the removal of ground state Ge I by reaction is not totally ruled out. Reactions between Ge and O_2 produce GeO in the electronic ground state with $\Delta E = +1.2$ eV [7]. The exothermicity of the reaction is sufficient to populate $GeO(X)$ up to $v'' = 5$ so no visible emission would be produced. We searched for vibrational excitation in $GeO(X)$, which would indicate chemical formation of GeO, by pumping from various X state vibrational levels ($0 \leq v'' \leq 5$) to the A state using the strongest Frank-Condon allowed transitions. We discovered strong emission lines from the molecule upon excitation from only $v'' = 0$. No LIF emission was observed after exciting from $v'' \geq 1$ even in the presence of various pressures of O_2 . In experiments similar to those performed with Ge I, the GeO LIF emission intensities decreased with increasing O_2 pressures. The $GeO(A \rightarrow X)$ LIF signals became undetectable at O_2 pressures near 40 mTorr. The radiative lifetime for $GeO(A)$ is not known, but, assuming typical values of 3-5 μs , a significant number of collisions would not occur eliminating electronic quenching as the source of the intensity decrease. Although the mechanism for these intensity decreases at various O_2 pressures is currently not understood, the results do indicate that chemical production of GeO via interactions of the plume material with the background O_2 does not occur.

Since the chemical production of GeO via plume-ambient gas interactions does not appear to be important, we traced the origin of diatomic GeO by monitoring LIF signals as a function of distance from the target surface. These LIF experiments showed that GeO molecules were present in the plume at distances as near as 2.5 mm from the target surface. Molecular LIF emission was also observed in vacuum. These results indicate that GeO is either produced as a result of recombination of material in the plume near the target surface where the ion and neutral number densities are high or the molecule dissociated directly from the target.

DISCUSSION

These experiments showed that interactions between the plume material and the ambient O_2 gas directly affected the concentrations of the excited neutral and ionic states of Ge and O atoms as well as molecular GeO. Two possible mechanisms can be postulated to explain the observed emission and LIF behavior described above. The first mechanism involves non-reactive plume-ambient gas interactions. Plume interactions with the background gas, especially at the higher gas pressures (> 50 mTorr), spatially confine the plume and should cause both the atomic emission features and the LIF intensities to increase. However, we observe increases in only the atomic emission intensities and not in the LIF signals. Therefore, this mechanism may not be plausible. The second mechanism involves reactive encounters between the plasma and the ambient gas. Scattering events between electrons and atoms or molecules and high kinetic energy collisions between atoms could produce neutral electronic excitation as well as additional ionization. Therefore, atomic emission experiments would show an increase in emission intensities as was observed here. These interactions would also result in a concurrent decrease in ground state species which is consistent with the LIF results.

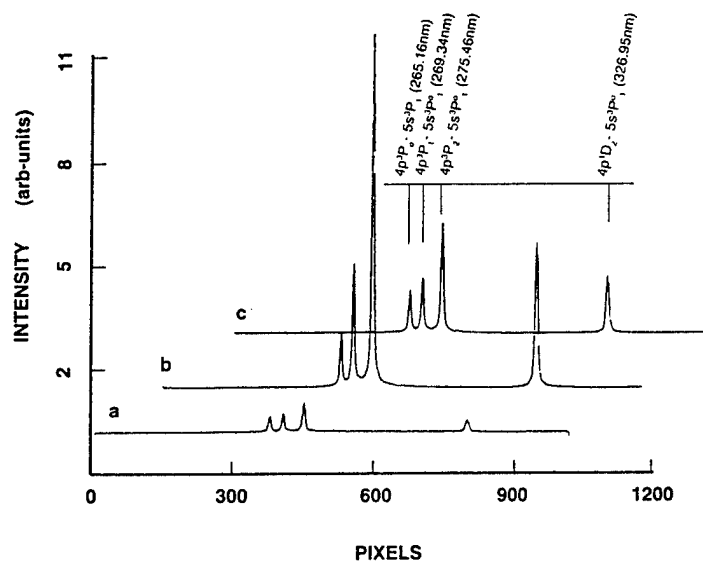


Figure 3. LIF emission spectra from Ge as a function of O_2 pressure: (a) $P(O_2) = 25$ mTorr, (b) $P(O_2) = 0$ mTorr, and (c) $P(O_2) = 10$ mTorr. These spectra were recorded 4 cm from the target surface with a $10.5 \mu s$ delay time between the excimer and the probe lasers.

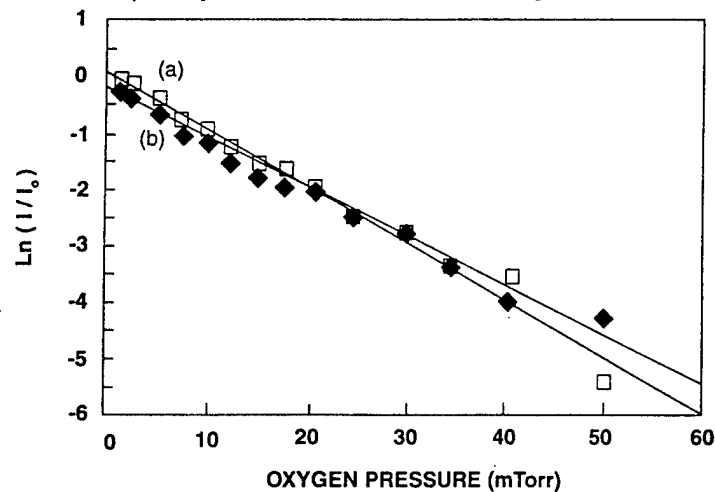


Figure 4. Plot of the natural log of the relative fluorescence intensities vs. O_2 pressure. Decays from two LIF emission lines are plotted: (a) $\lambda = 326.9$ nm and (b) $\lambda = 275.5$ nm. The cause of this decay may be due to a combination of reactive and non-reactive collisions with the ambient oxygen.

These results may have significance in determining the mechanisms for GeO_2 thin film growth. Since chemical reactions do not appear to dominate the plume-ambient gas processes, surface reactions must control the thin film growth. At high ambient gas pressures (i.e., $P(\text{O}_2) = 150$ mTorr), excess O_2 may be required to complete recombination reactions on the substrate surface, whereas at lower pressures, the discharge produces excited O atoms which can then interact more energetically with the substrate. These processes produce the same result: stoichiometric thin films. The importance of GeO in the film formation process is not completely understood. Diatomic GeO is abundant in vacuum but disappears as the O_2 pressure is increased. Since we cannot detect population in other vibrational levels of the ground state, GeO may either be scattered from the excitation region or the molecule could be dissociated as a result of plasma- O_2 interactions.

SUMMARY

Constituents of a laser-produced plume from a GeO_2 target have been spectroscopically examined. The results indicate complicated processes that occur when the plume interacts with the ambient O_2 . High kinetic energy species are produced and the behavior of individual species in the plume may be governed by several reactive and non-reactive encounters. Chemical production of diatomic species, which are critical for growing good quality high T_c thin films, does not occur for laser ablated GeO_2 plumes in O_2 , and thus does not appear to be important for growing stoichiometric GeO_2 thin films.

REFERENCES

1. P.J. Wolf, T.M. Christensen, N.A. Coit, and R.W. Swinford, *J. Vac. Sci. Technol. A*, **11**, 2725 (1993).
2. P.M. Swarengen, S.J. Davis, and T.M. Niemczyk, *Chem. Phys. Lett.*, **55**, 274 (1978).
3. D.J. Lichtenwalner, O. Auciello, R. Dat, and A.I. Kingon, *J. Appl. Phys.*, **74**, 7497 (1993).
4. S. Witanachchi and P.J. Wolf, submitted to *J. Appl. Phys.*
4. C.E. Otis and R.W. Dreyfus, *Phys. Rev. Lett.*, **67**, 2102 (1991) and references therein.
5. P.J. Wolf, in preparation.
6. M.H. Miller and R.A. Roig, *Phys. Rev. A*, **7**, 1208 (1973).
7. G.A. Capelle and J.M. Brom Jr, *J. Chem. Phys.*, **63**, 5168 (1975).

MATERIALS PHYSICS DIVISION

2300/FF/05

PUBLICATIONS

1 Oct 91 - 30 Sep 95

Examination of Schlieren Photography System, by Major Terrence F. Deaton, FJSRL-TM-91-0002, Oct 91.

Nonlinear Optical Doped Amorphous Glass and Process for Fabrication, by John J. Kester. Patent application submitted October 1991.

Photodissociation of S_4N_4 . I. 248 nm, by Dr T. Henshaw, Dr A. Ongstad and Captain R.I. Lawconnell. Poster paper presented at the Molecular Dynamics Contractors Conference, Annapolis MD, 28-30 Oct 90. Presentation at University of Denver, 10 Jan 91. Journal of Chemical Physics, Vol. 96, p. 53, 1992. FJSRL-JR-92-0003.

Photo-Electronic Nonlinear Excitations and Wave Propagation in Periodically Modulated Media, by Dr Marek Grabowski (UCCS). Submitted to Physical Review B, Feb 92.

Second Harmonic Generation in Planar Waveguides of Doped Silica, by John J. Kester, Paul J. Wolf, and W. Roc White (DFP). Optics Letters, Vol. 17, No. 24, Dec 92.

Photodissociation Dynamics of S_4N_4 at 222 and 248 nm, by Andrew P. Ongstad, Robert I. Lawconnell (DFMS), and Thomas L. Henshaw. Journal of Chemical Physics, 97(2), 15 Jul 92.

The Plasma Properties of Laser Ablated SiO_2 , by Paul J. Wolf. Journal of Applied Physics, 72(4), 15 Aug 92.

Modification of an Eulerian Hydrocode to Include Viscosity, by John P. Jackson. FJSRL-TM-92-0003, Sep 92.

Powder Second Harmonic Generation in Novel Inorganic Salts, by David P. Saunders. FJSRL-TM-92-0004, Sep 92.

Laser Ablation Deposition of Germanium Oxide Thin Films, by Paul J. Wolf, Thomas M. Christensen, Nathan G. Coit, and Richard W. Swinford (UCCS). Materials Research Society Symposium Proceedings, Vol. 285, pp 439-443, Laser Ablation in Materials Processing-Fundamentals and Applications Symposium, Boston MA, 30 Nov-4 Dec 92.

Nonlinear Polariton Excitations in Quantum Dot Arrays, by Pawel Hawrylak (NRC of Canada), Marek Grabowski, (UCCS), and Jacek A. Tuszynski (Univ of Alberta). Physics Letters A, Vol. 165, No. 2(1992), pp. 148-152.

The Thin Film Properties of Germanium Oxide Synthesized by Pulsed Laser Sputtering in Vacuum and Oxygen Environments, by Paul J. Wolf, Thomas M. Christensen, Nathan G. Coit, and Richard W. Swinford (UCCS). Journal of Vacuum Science and Technology A, 11(5) pp 2725-2732, Sep/Oct 93.

Use of the Asymmetric Photoionization Model to Explain the Length and Time Dependence of Second Harmonic Generation in Fibers, by Peter S. Weitzman (GSRP), Ulf Osterberg (SFRP)(Dartmouth College), and John J. Kester. Presented at the SPIE Meeting, Quebec Canada, 17-18 Aug 93. SPIE Proceedings of Photosensitivity and Self Organization in Optical Fibers and Waveguides, Vol. 2044, pp 146-157, 1993.

Electric Field Induced Second Harmonic Generation in Germanium Doped Silica Planar Waveguides, by Ulf L. Osterberg and Peter S. Weitzman (Dartmouth College). Final SFRP/GSRP report submitted to RDL 27 Aug 93.

Three Dimensional Characterization of Nonlinear Optical Thin Films, by Thomas M. Christensen (UCCS), final report for AFOSR Summer Research Extension Program, Dec 93.

Electric Field Induced Second Harmonic Generation in Germanium Doped Silica Planar Waveguides, by Peter Weitzman (GSRP), John J. Kester, and Ulf Osterberg (SFRP). Electronics Letters, Vol 30, No. 9, pp 697-698, 28 Apr 94.

Induced Second Harmonic Generation in Planar Waveguides by an Externally Applied Periodic DC Electric Field: Efficiency as a Function of Field Structures, by Mavis L. Brauer, Iyad Dajani, and John J. Kester. Electronics Letters, Vol. 30, No. 4, 17 Feb 94.

Activated Reactive Laser Deposition of GeO_2 Films, by Sarath Witanachchi (Univ of South Florida) and Paul J. Wolf. Journal of Applied Optics, Vol 76(4), pp 2185-2190, 15 Aug 94.

Time-Integrated Optical Emission Studies of Plumes Generated from Laser Ablated Germania Glass, by Paul J. Wolf. Journal of Applied Optics, Vol. 76(3), p. 1480-1486, Aug 94.

Analysis of National Institute of Standards and Technology Ore and United States Geological Survey Samples by Inductively Coupled Plasma Spectroscopy/Laser-Induced Breakdown Spectroscopy, by Terry L. Thiem (DFC) and Paul J. Wolf. Microchemical Journal, 50, 244-252, 1994.

Charge Transport and Second Harmonic Generation in Glass Waveguides, by David Statman. Final SFRP report, Sep 94.

The Temporal Behavior of Ge Atoms in Laser Generated Plumes by Optical Time-of-Flight Spectroscopy, by Paul J. Wolf. Submitted to the Journal of Applied Physics, September 1994.

Effect of Annealing on the Level of Second Harmonic Generation and Defect Sites in Poled Fused Silica, by Leanne J. Henry, Alan D. DeVilbiss, and Tsung E. Tsai. Invited talk. The

Symposium on Photorefractive Gratings and Quadratic Nonlinearities in Glass Waveguides: Fundamentals and Applications, Grasmere, Cumbria UK, 6-9 Mar 95. Submitted to the Journal of Optical Society of America B, 11 Oct 94.

Nonlinear Optical Switch in Amorphous Waveguides, by John J. Kester, Iyad A. Dajani, and Peter M. Ranon. Patent Application submitted 3 Nov 94.

Polarization Dependence of Second Harmonic Generation in Thin-Film Planar Waveguides, by Mavis L. Brauer, I. Dajani, and J.J. Kester. Physical Review Letters, Submitted 1 Dec 94.

Correlation of Ge E' Defect Sites with Second Harmonic Generation in High-Water Poled Fused Silica, by Leanne J. Henry. Submitted to Optics Letters, Jan 95. Accepted.

Static Electric Field Due to Seeding Inside and Outside of a Planar Waveguide, by Mavis L. Brauer and Iyad A. Dajani. Journal of Applied Physics, Vol. 77(3), pp 970-975, Feb 95.

Mycoplasma Characterization Using Protein Profiling in Human Cell Co-Culture, by John Leavitt, Elaine Goodman, Henry Tillinghast. Submitted to the Journal of Clinical Microbiology, Mar 95.

Spin-Unrestricted Time-Dependent Hartree-Fock Theory of Frequency-Dependent Linear and Nonlinear Optical Properties, by Shashi Karna. Submitted to the Journal of Chemical Physics, Apr 95.

Second-Harmonic Generation Efficiencies in Germanium-Doped Planar Waveguides: A Normal-Mode Analysis, by Iyad Dajani. Submitted to Journal of Modern Optics, 31 Aug 94. Accepted 20 Oct 94. Projected publication - summer 1995.

Effect of Annealing on the Level of Second Harmonic Generation and Defect Sites in Poled Fused Silica, by Leanne J. Henry, Alan D. DeVilbiss (UCCS), and Tsung E. Tsai (Virginia Polytechnic Institute). Submitted to Journal of Optical Society of America B, 11 Oct 94. Projected publication - summer 1995.

Polarization Dependence of Second Harmonic Generation in Thin-Film Planar Waveguides, by Mavis L. Brauer, I. Dajani, and J.J. Kester. Submitted to Physical Review Letters 1 Dec 94. Projected publication - summer 1995.

Isomerization Energies and Nonlinear Optical Properties of *cis* and *trans* $\text{Si}_2\text{H}_6\text{O}_2$, $\text{Si}_2\text{H}_6\text{O}_8$, and $\text{Si}_8\text{H}_{18}\text{O}_8$ Clusters, by Leanne J. Henry and Walter J. Lauderdale. Submitted to the Journal of Physical Chemistry, 31 May 95.